2021년 2월
석사학위논문

Evaluation and Analysis of 1g Shaking Table Test Modeling by Simulation Programs

조 선 대 학 교 대 학 원

토 목 공 학 과

JIN YONG

Evaluation and Analysis of 1g Shaking Table Test Modeling by Simulation Programs

시뮬레이션 프로그램에 의한 1g 진동대 시험 모델링 평가 및 분석

2020년 2월 25일

조 선 대 학 교 대 학 원

토 목 공 학 과

JIN YONG

Evaluation and Analysis of 1g Shaking Table Test Modeling by Simulation Programs

지도교수 김 대 현

이 논문을 공학 석사학위 논문으로 제출함.

2020년 10월

조 선 대 학 교 대 학 원

토 목 공 학 과

JIN YONG

JIN YONG의 석사학위논문을 인준함.

위원장 조선대학교 교수 박 상 준 (인)

위 원 조선대학교 교수 김 대 현 (인)

위 원 조선대학교 교수 이 희 영 (인)

2020년 11월

조 선 대 학 교 대 학 원

TABLE OF CONTENT

LIST OF TABLES

LISTS OF FIGURES

초 록

시뮬레이션 프로그램에 의한 1g 진동대 시험 모델링 평가 및 분석

김 용
지도교수 : 김 대 현
조선대학교 일반대학원 토목공학과

지진피해 분석은 내진설계의 안전성 향상을 위하여 지진응답해석을 실시할 필요가 있다. 진동대 실험은 지반 및 지진공학 연구에서 중요한 실험 중 하나이다. 각종 지반 및 건축 모델의 방진시험과 중요시설의 내진성능 평가에서는 연구자의 필요에 따라 진동대 시험을 수행하거나 특정 지진파를 재현하거나 특정 주파수의 진동을 반복 가진할 수 있다. 진동대 시험에서 얻은 지반의 응답은 실 지진파가 원형지반에 미치는 영향을 예측할 수 있으며 지진 대책이나 지반의 댐핑을 연구하기에 용이하다.

본 연구에서는 유한요소 프로그램 ABAQUS와 1차원 지반해석 프로그램 DEEPSOIL을 사용하여 수치해석 후 1g 진동대 시험 결과와 상호비교하였다. 가속도-시간 이력, 최대지반가속도, 가속도 스펙트럼을 활용하여 1g 진동대 실험에 대해 DEEPSOIL 및 ABAQUS의 신뢰성과 지반의 지진응답해석을 검증하고 의미있는 결론을 도출하였다.

Chapter 1. Introduction

1.1 Background

In recent years, the probability of global earthquakes has continued to increase, and high-intensity earthquake disasters have occurred frequently, such as the magnitude 7.9 earthquake that occurred in central Nepal in April 2015, the magnitude 7.3 earthquake that occurred in Kyushu, Japan in April 2016, and the magnitude 5.4 earthquake that occurred in Pohang, South Korea on November 15, 2017, and the magnitude 6.4 earthquake occurred near Hualien County, Taiwan in February 2018. The earthquake caused the collapse of buildings and casualties, and brought endless pain and disaster to human society.

In the event of an earthquake, the seismic wave propagated from the bedrock reaches upper soil particles through the soil layer, as shown in Figure 1.1 (Kwon and Yoo, 2020). The dynamic stress of the soil unit is mainly caused by shear waves propagating upward from the bedrock, and the unit will be subjected to repeated action of shear stresses whose magnitude and direction are constantly changing.

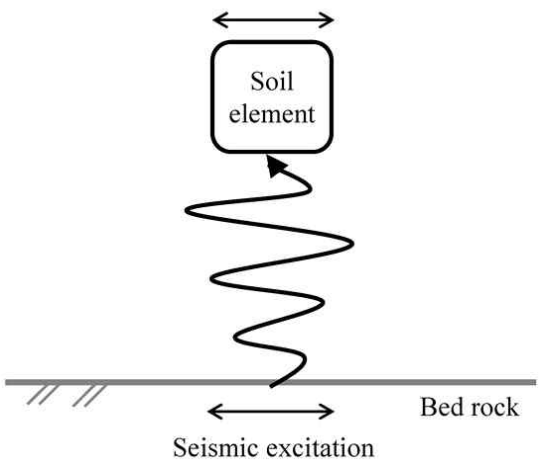

Figure 1.1 Earthquake wave transmission (Kwon and Yoo, 2020).

From point of failure of soils, there are two types of stresses which acts on a soil mass, as shown in Figure 1.2. Normal stress which acts normal to the plane and is of compressive nature as soil does not experience any tensile forces. Shear stress which acts parallel to the surface of the soil mass and tends to slide or slip that soil mass from rest of the soil mass. When this shear stress exceeds the shear strength of a soil then it is called the shear failure for that soil element.

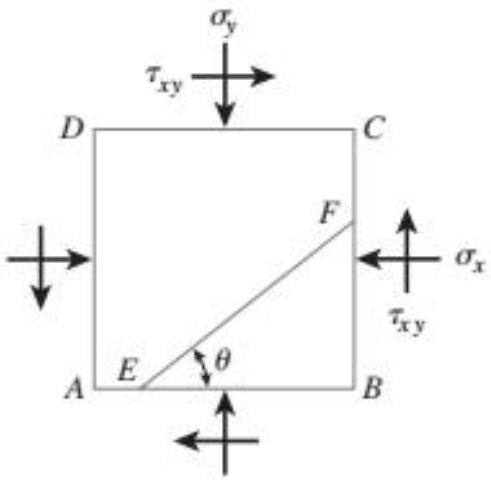

Figure 1.2 A soil element with normal and shear stresses acting on it.

1.2 Research methods

1.2.1 Laboratory simulation experiment

Due to the randomness and uncertainty of earthquakes, it is necessary to conduct simulated earthquake experiments to obtain soil experimental data under artificial control. Therefore, the earthquake simulation shaking table came into being in the 1960s. In order to obtain ideal test results, researchers have carried out a lot of research work in the design and production of soil tanks. After continuous improvement, earthquake simulation shakers have now been developed worldwide and have a certain scale. Shaking table model test is an important method to study the mechanism and failure mode of ground earthquake failure, evaluate the overall seismic capacity of the ground, and measure the effects of seismic reduction and isolation.

Shaking table test is divided into centrifuge shaking table test and 1g shaking table test. The boundary conditions for one-dimensional vibration are shown in figure 1.3. The most popular is the 1g shaking table model. The 1g shaking table test assumes that the model foundation and the prototype foundation have similar vibration processes. It is hoped that the soil box can restrain the soil while controlling the impact of soil vibration within the allowable range. The reflection and scattering of the waves in the experiment will cause the result to be distorted. How to restore the earthquake as much as possible under artificial design has become one of the problems that researchers have thought. Therefore, the design of the model box is very important. At present, the models commonly used by researchers include rigid boxes, flexible boxes and laminar shear boxes.

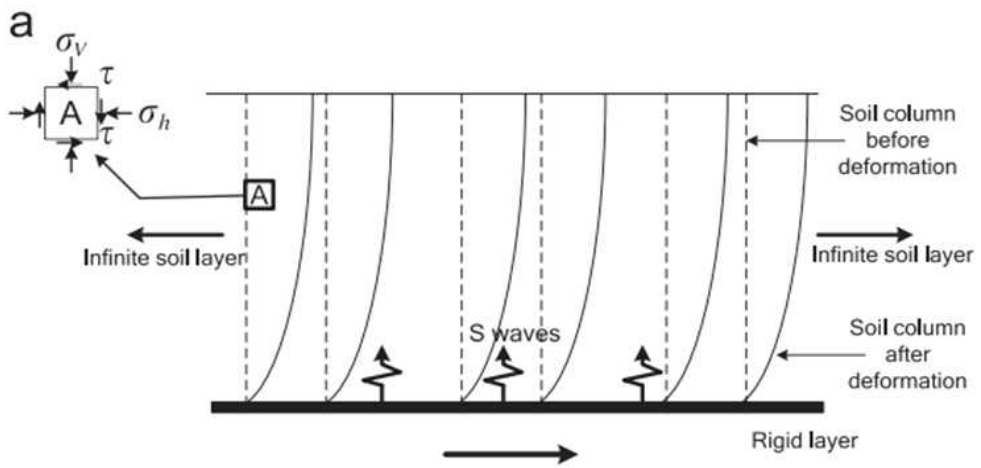

(a) in a semi-infinite half space

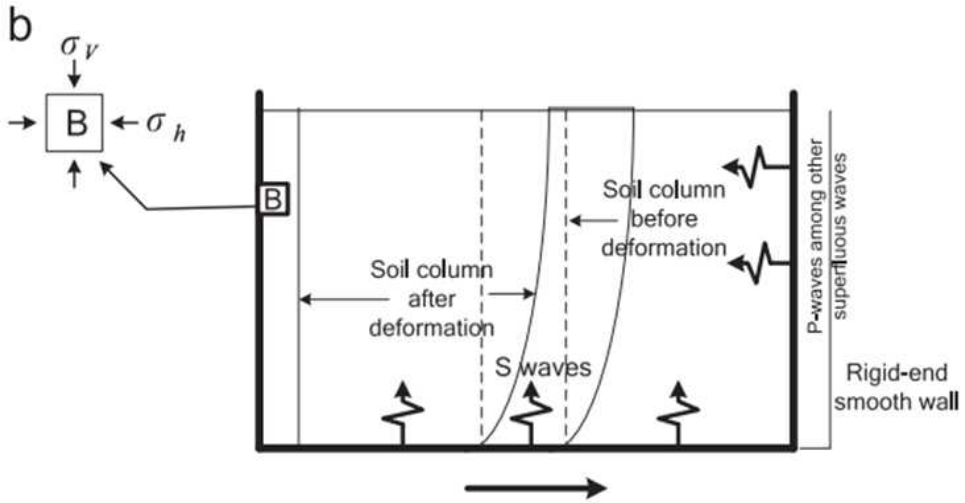

(b) in a centrifuge model within a rigid smooth wall container

Figure 1.3 Boundary conditions during 1D shaking(Lee et al, 2012).

In addition, incompatible displacements (strain dissimilarity) between the zigzagged wall face and the soil bed might cause P-waves among other superfluous wave reflections on both sides of container no matter which direction the soil bed moves to as shown in Figure 1.4. Kim and Ryu (2008) modeled and compared the ground responses in the free field, rigid box, and laminar shear box by using a 3-D FEM program. It is found from the numerical simulations that the

laminar shear box can simulate the free field ground movement more precisely than the rigid box. Turan et al (2009) studied the boundary effects of a laminar container on a synthetic clay in a 1g shaking table test. Only a small amplitude (0.1g) excitation was applied to the shaking table and assessed the boundary effects in terms of the peak amplitude of acceleration measured at various distances from the end wall. Individuality of boundary effects occurs in each laminar container; therefore, evaluation of boundary effects on a new container tested in the in-situ stress level is essential (Lee et al, 2012).

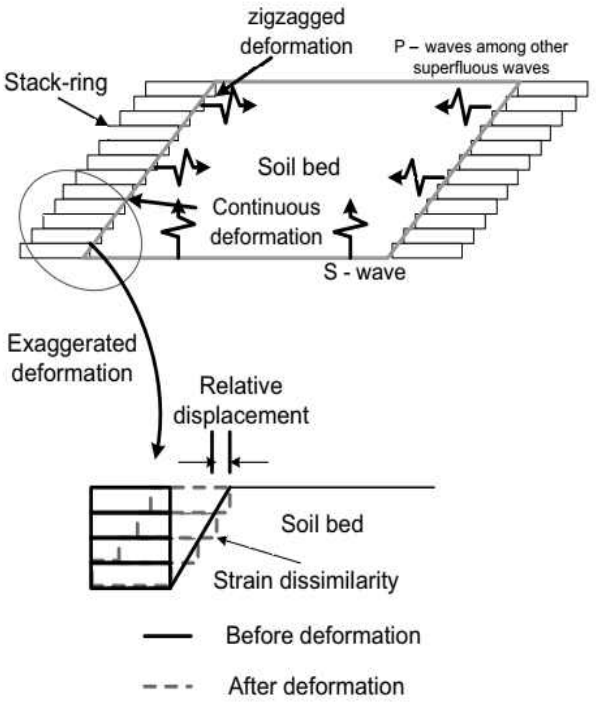

Figure 1.4 Incompatible displacement(strain dissimilarity) between the end wall of laminar container and the bed during shearing (Lee et al, 2012).

1.2.2 Numerical analysis simulation method

Since the 1980s, the rapid development of computer technology has greatly promoted the development of numerical solutions for ground seismic response analysis. The whole ground system can be calculated dynamically by finite element method. Many scholars begin to use large commercial finite element program to analyze the seismic response of slope and flat.

Andersen (2010) presented a numerical model for studying the dynamic evolution of landslides and analyzed a simplified slope with houses placed on the top. Faris and Wang (2014) performed finite element calculation of seismic acceleration in shear zone of landslide using ABAQUS 2D model.

The finite element method can calculate the dynamic response of the whole flat ground system. It can simulate the contact surface between soil and ground in complex terrain flexibly, especially for geometric non-linearity, material non-linearity and contact solving non-linearity, which can not be achieved by simplified algorithm. When the finite element method is used to deal with the dynamic problem, how to transform the infinite boundary dynamic problem into the finite boundary dynamic problem becomes the difficulty in the application of this method. The selection and simulation of artificial boundary will directly affect the accuracy of the calculation results.

1.3 Research objectives

Firstly, the dynamic characteristics of the soil are experimentally studied. Based on the ABAQUS finite element program, the nonlinear dynamic constitutive model of the soil is established. At the same time, the time-domain nonlinear one-dimensional seismic response analysis program DEEPSOIL is used to integrate and compare the data. The main research objectives of this thesis are as follows:

1. This thesis introduces the calculation method of site seismic response, summarizes the determination of bedrock ground motion and soil dynamic constitutive model, and summarizes the setting of artificial boundary conditions.

2. In the seismic problem of slope and flat ground, the 1g shaking table test in the model experiment is introduced in detail, including experimental equipment, experimental settings, experimental methods, operating platforms, etc. Comparing the advantages and disadvantages of several current model box boundary effect evaluation methods, and choosing an evaluation method that best reflects the boundary error are discussed to study the boundary effect of the model box.

3. Based on the soil nonlinear dynamic constitutive model established in the ABAQUS program, the nonlinear seismic response of the site when horizontal ground motion is input to the bedrock surface is analyzed, and the feasibility of the established Mohr-Coulomb model is verified. The modeling process and detailed problems are introduced. Also, the time-domain nonlinear one-dimensional seismic response analysis program DEEPSOIL is verified.

Chapter 2. Literature review on nonlinear dynamic constitutive models of soil

Several different constitutive relations accounting for the non-linear stress - strain relations, accumulation of irreversible deformation and hysteresis under cyclic loading have been suggested for soil (Shalev et al, 2014).

In the process of studying the mechanical behavior of soil under cyclic loading, the most difficult thing is to determine the relevant parameters describing the properties of the soil. Therefore, when conducting seismic design related to geotechnical engineering, the dynamic shear modulus is used. Shear strain amplitude, damping ratio, maximum shear modulus and other parameters to accurately describe the dynamic characteristics of the soil are key issues that need to be resolved. Small-strain shear-wave velocity(V_s) is directly related to small-strain shear modulus($G_{\max}$) by

$$G_{\max} = \rho V_s^{\,2} \tag{2.1}$$

where, ρ = mass density of soil
(total unit weight of the soil divided by the acceleration of gravity).

2.1 Basic theory of models

Experimental research shows that the relationship between dynamic shear modulus G and dynamic shear strain of saturated soft soil basically conforms to the hyperbolic relationship. Hardin et al. (1972) proposed the empirical relationship between predicting G and the Hardin-Drnevich model, and then Martin and Seed et al. (1982) believed that the Davidenkov model can better describe the dynamic deformation characteristics of soft soils. After that, many researchers have

improved and promoted the previous theories.

2.1.1 Hardin-Drnevich Model

The Hardin-Drnevich model is a hyperbolic relationship model proposed by Hardin et al. (1972). The basic idea is to use a certain hyperbolic function to simulate the soil stress-strain skeleton curve (Figure 2.1).

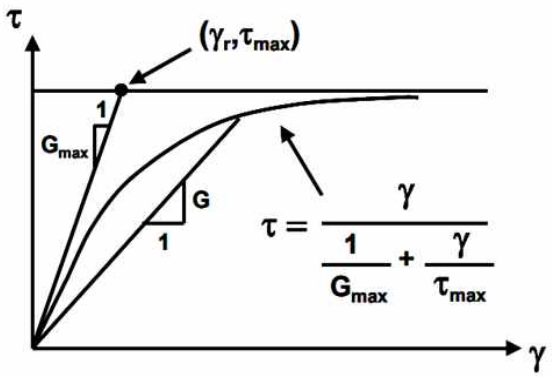

Figure 2.1 Hyperbolic stress-strain relationship (Hardin et al, 1972).

The usual form of the hyperbolic stress-strain relation is :

$$\tau = \frac{\gamma}{\frac{1}{G_{\max}} + \frac{\gamma}{\tau_{\max}}} \tag{2.2}$$

Where, τ = shear stress

γ = shearing strain

$G_{\max}$ = small-strain shear modulus

$\tau_{\max}$ = shear strength of the soil.

The reference shear strain value is introduced:

$$\gamma_t = \frac{\tau_{\max}}{G_{\max}} \tag{2.3}$$

Dividing the resulting equation by $G_{\max}$ and subsitituting equation(2.3):

$$\frac{G}{G_{\max}} = \frac{1}{1+\frac{\gamma}{\gamma_t}} \tag{2.4}$$

Equation 2.4 is also the standard form of the relationship between the shear modulus ratio and the amplitude of the shear strain used in the analysis of seismic response of soil layers in the current seismic safety assessment.

$G_{\max}$ should be determined according to the resonance column test, but in the absence of test, it can also be determined by Hardin's empirical formula (2.5) applicable to undisturbed cohesive soil and sand:

$$G_{\max} = 1230\frac{(2.973-e)}{(1+e)}(OCR)^k\sigma_0^{-1/2} \tag{2.5}$$

Where, e = Void Ratio

OCR = Over Consolidation Ratio

σ_0 = Mean Effective Stress

k is depending on plastic index of soil, it can be obtained by interpolation in Table 2.1.

Table 2.1 K value table

Π	0	20	40	60	80	100
K	0	0.18	0.3	0.41	0.48	0.5

The simple relationship between modulus and damping is:

$$D = D_{\max}(1 - \frac{G}{G_{\max}}) \tag{2.6}$$

Substituting equation 2.3 and equation 2.6 and dividing by $D_{\max}$:

$$\frac{D}{D_{\max}} = \frac{\frac{\gamma}{\gamma_r}}{1 + \frac{\gamma}{\gamma_r}} \tag{2.7}$$

2.1.2 Davidenkov Model

Martin and Seed (1982) modified the Hardin hyperbolic model. At this time, the Hardin-type skeleton curve equation can be expressed as follows:

$$\tau = G\gamma = G_{\max}\gamma[1 - H(\gamma)] \tag{2.8}$$

$$\gamma = \frac{\tau}{G_{\max}}[1 + F(\tau)] \tag{2.9}$$

For the convenience of presentation, let:

$$\frac{G}{G_{\max}} 1 - H(\gamma) \tag{2.10}$$

$$H(\gamma) = \frac{\frac{\gamma}{\gamma_r}}{\frac{\gamma}{\gamma_r}} \tag{2.11}$$

Davidenkov skeleton curve was used to describe the above stress-strain

relationship:

$$\frac{G}{G_{\max}} = 1 - [\frac{(\frac{\gamma}{\gamma_0})^{2B}}{1+(\frac{\gamma}{\gamma_0})^{2B}}]^{A} \tag{2.12}$$

Rewrite $H(\gamma)$ into the following form:

$$H(\gamma) = [\frac{(\frac{\gamma}{\gamma_0})^{2B}}{1+(\frac{\gamma}{\gamma_0})^{2B}}]^{A} \tag{2.13}$$

Where, A and B are fitting parameters related to soil properties.

It should be pointed out that 0 here is no longer a reference shear strain amplitude with a clear physical meaning, but just a fitting parameter.
And the analog equation of damping ratio in power form is put forward as follows:

$$\lambda = \lambda_{\max}[[\frac{(\frac{\gamma}{\gamma_0})^{2B}}{1+(\frac{\gamma}{\gamma_0})^{2B}}]^{A}]^{n} \tag{2.14}$$

Where, γ = shearing strain

$G_{\max}$ = small-strain shear modulus

A, B, $\lambda_{\max}$, n, γ_0 are the fitting parameters.

Substituting into equation 2.5 and equation 2.6, the skeleton curve expression of

Davidenkov model can be obtained:

$$\tau = G \cdot \gamma = G_{\max}\gamma 1 - [\frac{(\frac{\gamma}{\gamma_0})^{2B}}{1+(\frac{\gamma}{\gamma_0})^{2B}}]^{A} \tag{2.15}$$

In addition, when A=1.0, B=0.5, $\gamma = \gamma_0$, the stress-strain relationship curve described by the Davidenkov model degenerates to the Masing hyperbolic model.

Since, τ is function of γ_0, the incremental expression of G in the skeleton curve can be obtained by deriving equation 2.11 with respect to :

$$G = G_{\max}[1 - [\frac{(\frac{\gamma}{\gamma_0})^{2B}}{1+(\frac{\gamma}{\gamma_0})^{2B}}] - A\frac{\gamma}{\gamma_0}[\frac{(\frac{\gamma}{\gamma_0})^{2B}}{1+(\frac{\gamma}{\gamma_0})^{2B}}]^{A-1}\frac{2B(\frac{\gamma}{\gamma_0})^{2B-1}}{[1+(\frac{\gamma}{\gamma_0})^{2B}]^2}]] \tag{2.16}$$

When the skeleton curve of stress-strain relationship is Davidenkov model, Masing's rule can be used to construct the corresponding hysteretic curve. According to Masing's rule, the calculation formula of hysteretic curve is :

$$\frac{\tau - \tau_r}{2} = f(\frac{\gamma - \gamma_r}{2}) \tag{2.17}$$

Where, τ is the stress at the inversion point
γ is the strain of inversion point.

Hysteretic loop is defined as follows. Due to the nature of materials, when the load is greater than a certain degree, residual deformation occurs during unloading,

that is, the load is zero but the deformation does not return to zero, which is called hysteresis phenomenon. In this way, after a load cycle, the load displacement curve forms a loop, which is called hysteretic loop, as shown in figure 2.2.

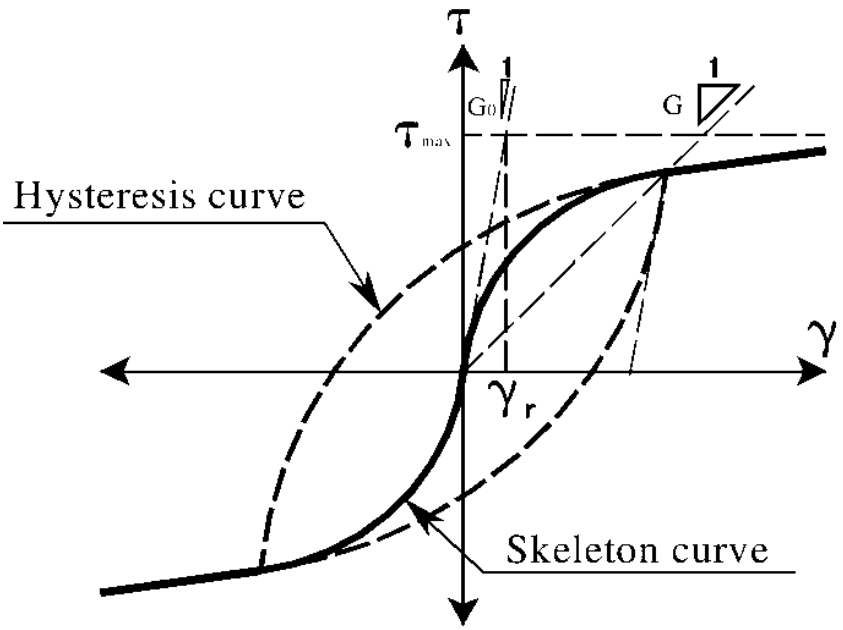

Figure 2.2 Masing rule hysteresis loop (Hardin et al, 1972).

Combining equation 2.15 and equation 2.17 to obtain the calculation expression of hysteresis curve is:

$$\tau = 2G_{\max}R1 - [\frac{(R)^{2B}}{1+(R)^{2B}}]^{A} + \tau_r \qquad (2.18)$$

Where, $R = \frac{\gamma - \gamma_r}{2\gamma_0}$.

Equation 2.18 is derived from γ to obtain the incremental expression of G in the hysteresis curve:

$$G = G_{\max}[1-[\frac{(\frac{\gamma}{\gamma_0})^{2B}}{1+(\frac{\gamma}{\gamma_0})^{2B}}]-A\frac{\gamma}{\gamma_0}[\frac{(\frac{\gamma}{\gamma_0})^{2B}}{1+(\frac{\gamma}{\gamma_0})^{2B}}]^{A-1}\frac{2B(\frac{\gamma}{\gamma_0})^{2B-1}}{[1+(\frac{\gamma}{\gamma_0})^{2B}]^2}]] \quad (2.19)$$

Thus, the complete Davidenkov skeleton curve and the hysteresis curve of unloading and reloading are obtained.

2.1.3 Darendeli Model

In order to consider the influence of confining pressure, Darendeli (2001) further improved the widely used Hardin hyperbolic model as:

$$\frac{G}{G_{\max}} = \frac{1}{1+(\frac{\gamma}{\gamma_0})^a} \quad (2.20)$$

Where, γ_r is γ at $G/G_{\max}$ equal to 0.5, and "a" is curvature coefficient.

With the added curvature coefficient, the modified hyperbolic model fits the measured normalized shear modulus reduction curve slightly better than the original hyperbolic model.

The physical of hysteresis loop is as follows.: During the earthquake, the field ground in the earthquake, the earthquake energy input ground, the ground is a continuous process of energy absorption and dissipation when ground into the elastic-plastic state, its seismic performance mainly depends on the ability of energy dissipation components add lotus phase hysteresis curve under load - displacement curve surrounded area can reflect the size of the ground to absorb energy; And unloading curve and load curve as the area surrounded by the energy dissipation of the energy is through the material of inner friction or local damage, such as crack and plastic hinge rotation, etc. The energy is converted into heat energy is lost to space, therefore, hysteretic curve in the area of hysteresis loop back is used to assess an important indicator of energy dissipation ground.

Figure 2.3 shows calculation of damping ratio utilizing a hysteresis loop. Damping ratio D is a parameter to estimate the proportional relationship between dissipated energy and maximum stored energy in each dynamic period at a given strain level. In figure 2.3, the area is enclosed by the hysteresis loop is represented the energy dissipated in a dynamic cycle, while the triangular area enclosed by the peak shear stress and peak shear strain (the diagonally filled part in the figure) are represented the maximum stored energy. Damping ratio is the result of friction between soil particles, strain rate effect and stress-strain nonlinear relation of soil. Because the damping ratio is almost frequency independent in the frequency range of engineering concern, it is usually refered to as hysteresis damping. The nonlinear relation of stress and strain will lead to the increase of dissipated energy, so the damping ratio of soil material will increase with the increase of strain level. In the elastic stage (small strain stage), the damping ratio of soil is called D_{min}.

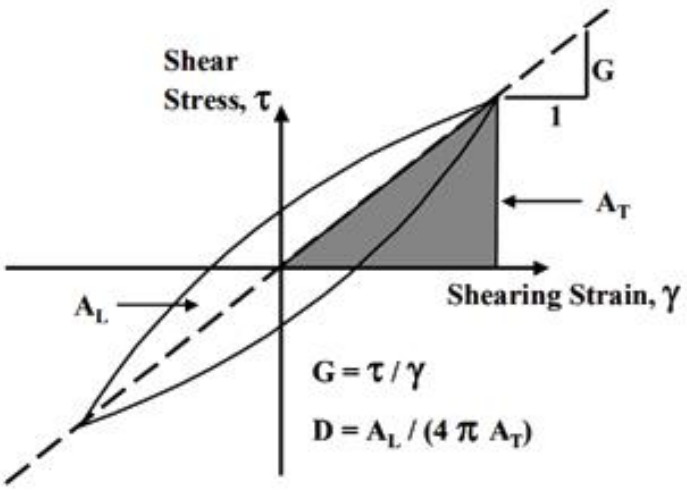

Figure 2.3 Calculation of damping ratio utilizing a hysteresis loop (Darendeli, 2001).

Darendeli (2001) adjusted the material damping ratio determined form the

"Massing behavior" with a scaling function, $b\times(\frac{G}{G_{\max}})$, so that estimated material damping ratio was closer to those measured in the laboratory at low G/G_{max} range. The defined the adjusted material damping ratio, $D_{Adjusted}$, as:

$$D = b\times(\frac{G}{G_{\max}})\times Dmasing + D_{\min} \tag{2.21}$$

where, $D_{\min}$ is the material damping ratio at small-strain range, and b is a scaling coefficient.

Hence, a four-parameter model (γ_r, a, b and $D_{\min}$) is used to characterize the normalized modulus reduction and material damping curves. A parametric study is also presented to assist the reader in becoming familiar with the modified hyperbolic model and the impact of each of the parameters.

2.1.4 Menq Model

Menq (2003) used the modified hyperbolic model proposed by Darendeli (2001) to model the relationship between normalized shear modulus and shear strain as:

$$\frac{G}{G_{\max}} = \frac{1}{1+(\frac{\gamma}{\gamma_r})^a} \tag{2.22}$$

Where : γ = shearing strain

$G_{\max}$ = small-strain shear modulus

γ_r is the reference shearing strain (with respect to shear modulus), and a is the curvature coefficient.

The small-strain material damping ratio can be expressed as:

$$D_{s,\min} = 0.55 \times C_u^{\,0.1} \times D_{50}^{\,-0.3} \times (\sigma_0^{'}/P_a)^{-0.08} \quad (2.23)$$

Where : D_{50} = median grain size,

C_u = uniformity coefficient, and

$\sigma_0{}'$ = effective confining pressure.

2.1.5 Roblee and Chiou Model

Roblee and Chiou (2004) compiled the results of 154 laboratory tests into a database, Each test result consists of laboratory-measured values of modulus, normalized modulus, and damping ratio as a function of strain. Curves fits have been established for each set of normalized modulus and damping ratio curves using equations outlined by Darendeli and Stokoe (2001). Each normalized modulus (G/G_m) versus shear strain (γ) curve has been fit with a 2-parameter model as follows:

$$\frac{G(\gamma)}{G_m} = \frac{1}{1+(\frac{\gamma}{\gamma_{ref}})^a} \quad (2.24)$$

The two normalized-modulus curve-fit parameters are:

γ_{ref} = reference strain that defines the location of the hyperbolic curve on the strain axis.

α = shape parameter that modifies the curvature of the hyperbolic curve.

Each damping ratio (D) versus shear strain (γ) curve is also fit with a 2-parameter model as follows:

$$D(\gamma) = D_{min} + \beta \times D_{masing}(\gamma) \times (\frac{G(\gamma)}{G_m})^{0.1} \quad (2.25)$$

Where, D_{masing} = damping ratio calculated using Masing assumptions.

The two damping ratio curve-fit parameters are:

D_{masing} = minimum damping ratio at low strain

β = adjustment constant to scale Masing damping (D_{masing}) to experimental data.

2.1.6 Zhang and Andrus Model

Zhang and Andrus (2005) conducted resonance column and torsion shear tests on 122 soil samples collected, and used the modified hyperbolic model to verify the test data.

$$\frac{G}{G_{\max}} = \frac{1}{1+(\frac{\gamma}{\gamma_r})^{\alpha}} \tag{2.26}$$

Equation 2.26 is adopted to model the variation of $G/G_{\max}$ with γ.

Where γ_r=reference strain and a=second curve-fitting variable called the curvature parameter.

The best fit curve between TS test values of $G/G_{\max}$ and D minus $D_{\min}$ is expressed as:

$$D - D_{\min} = f(G/G_{\max}) = 10.6(G/G_{\max})^2 - 31.6(G/G_{\max}) + 21.0 \tag{2.27}$$

2.2 Summary

Table 2.2 lists the research results of some existing dynamic characteristic models. These models are based on the results of the torsional shear experiment of the resonant column and are proposed according to the above formula. As shown in the table, the model proposed by Darendeli (2001) is suitable for general soil models (sand, silt and clay), but for coarse-grained soils with coarser particles, it is more reasonable to replace the model proposed by Menq (2003).

Table 2.2 Existing soil dynamic characteristics model

References	Type of soil used	Applicable strain range
Darendeli, 2001	General (20 sites, 110 samples)	0.0001-0.5%
Menq, 2003	D50>0.3mm Coarse grained soil(59 samples)	0.0001-0.6%
Roblee and Chiou, 2004	Clay, sand, silty soil(28 sites, 154samples)	0.0001-4.0%
Zhang et al, 2005	Mineral soils of Southern California(38 samples)	0.0001-0.3%

After a long time of development with the efforts of many researchers, the research on this aspect has great progress. After the comparison of soil physical properties, Darendeli model is the most suitable for this study.

Chapter 3. Experimental program

3.1 Soil properties

The soil sample of the scaled-down model test in this study was collected from a construction site in Korea and the cut slope in the construction site, located at Ulju-gun, Ulsan Metropolitan City.

Table 3.1 shows the geotechnical index properties of the specimen used in this experimental study. Through specific gravity test, grain size test, standard proctor test and relative density test, the physical properties of the soil were analyzed. The specific gravity of the soil was 2.69, the maximum dry unit weight was 18.27 kN/m^3, and the minimum dry weight was 12.43 kN/m^3. The optimum moisture content was 12.5% and the Atterberg limit test showed Non Plastic (NP) for Plastic Index (PI).

Table 3.1 Geotechnical index properties of the specimen used in this study.

Parameter	Value	Parameter	Value
No.200 Passing(%	10.8	e_{max}	1.123
G_s	2.69	e_{min}	0.443
OMC%)	12.5	γ_{dmax}	18.27
PI%)	N.P	γ_{dmin}	12.43
USCS	SW-SM	Elastic modulus(Pa	2x10^8
Internal friction angle(ϕ)	27.7°	Dilatancy angle(ϕ)	24.4°

The maximum and minimum void ratios were 1.123 and 0.443. The fines content of the soil was 10.8% and the soil was classified as SW-SM according to the Unified Soil Classification System. For the dynamic model test, the specimen was selected for the sample passing through the No. 4 sieve after the physical property tests, and the sample remaining in the No. 4 sieve was about 1%, not much. The elastic modulus is $2x10^8$Pa. This value is obtained indirectly using experimental data. The calculation of the modulus of elasticity is explained in the chapter 4. According to the existing experimental data, the friction angle of 27.7°, the dilatancy angle of 24.4° were used in the study(Angle of friction, USCS).

3.2 1g shaking table test equipment

3.2.1 Introduction to 1g shaking table test equipment

The system is mainly composed of a hydraulic source system, a vibration exciter, a servo analog controller, a table top, and a computer control system. The servo analog controller is an analog controller with an electro-hydraulic servo valve as the core, and its performance affects the entire system. It plays a decisive role and is the core part of the entire control system. The hydraulic source system mainly provides power, including hydraulic pump stations, accumulator groups, cooling systems, etc. The flow rate of the hydraulic pump is designed according to the maximum speed value of the seismic wave. To save energy, large-capacity accumulator groups are currently installed to provide the actuators with huge instantaneous energy, as shown in Figure 3.1.

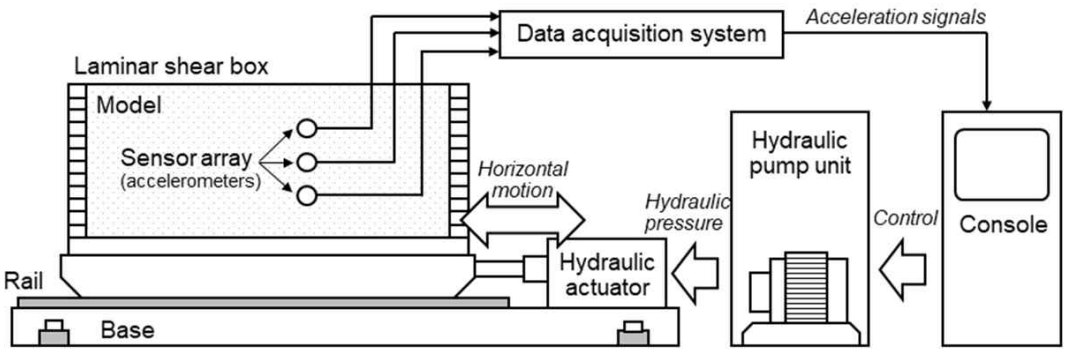

Figure 3.1 The 1g shaking table test equipment in this study (Kim et al, 2020).

3.2.2 Laminar shear box

In this study, a soft soil structure composed of most horizontally activated frames is used. The horizontal shear motion of soft soil foundation can simulate infinitely extending foundation boundary conditions. The specification of this soft soil tank is 200cm (horizontal) × 60cm (vertical) × 60cm (height), with a total of 12 layers of aluminum frame structure. The thickness of each frame is 4.5 cm, and the spacing between frames is about 0.5 cm. Each frame can move independently in a horizontal direction through a rolling bearing. The wall is made of aluminum. The natural period of the empty box is 0.04-0.05s. Figure 4.4 is the conceptual diagram of the soft soil structure and shaking table test equipment used in this test.

Fig 3.2 Laminar shear box used in this study.

In order to have consistent unit weight of the soil in each layer, careful compaction was done.

3.2.3 Shear wave velocity measurement

As shown in Figure 4.5, a typical bending element includes two piezoelectric sensors, one as the excitation source and the other as the receiver, which is mounted on the sample cap or other boundary in a cantilever manner, inserts the soil medium, and ensures that the sensor is connected to the soil. The shear wave velocity test measures the first wave arrival time to find the speed with the knowledge of the distance between the Piezoelectric stack and the accelerometer (Kim et al, 2020).

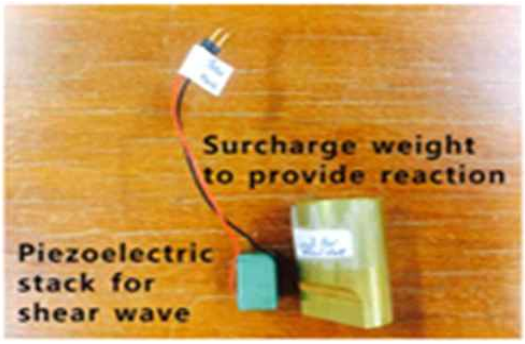

(a) Piezoelectric stack for shear wave and weight

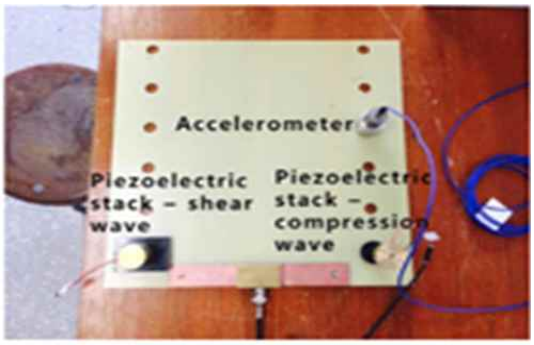

(b) Accelerometer to pick up vibration

(c) Combined component

(d) The whole view of the TDR system

Figure 3.3 Shear wave velocity measurement(Song et al, 2016).

The excitation source emits a shear wave to obtain the shear wave velocity by measuring the time difference of the shear wave reaching the receiver, as shown in the formula. The calculation equation of shear wave velocity is:

$$V_s = \frac{L}{\Delta t} \tag{3.1}$$

Where, V_s = shear wave velocity

L = distance between bending elements

Δt = propagation time of shear wave.

The calculation principle is shown in Figure 3.4.

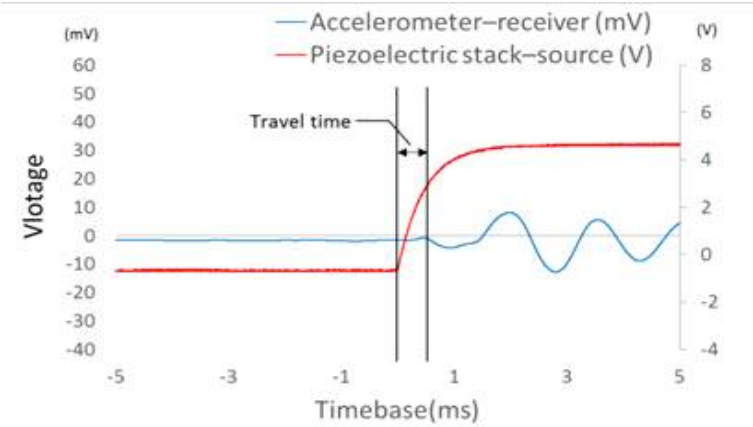

Figure 3.4 Travel time of elastic wave obtained by using the Piezoelectric stack (Kim et al, 2020).

3.2.4 Accelerometer

The response acceleration measured in this test was expected not to be faster than 20m/s^2 in terms of range, and the assumption was based on the frequency component of response data not being greater than 40Hz, and the room temperature. Therefore, the selected accelerometer was ARF-20A, which can measure up to 20m/s2. The data logger had 12 channels and was compatible with ARF-20A as a 4 Gage Sensor, and the data collection interval was maximum 0.001. Figure 3.5 shows the location of the accelerometers set in the flat center in 1g shaking table test.

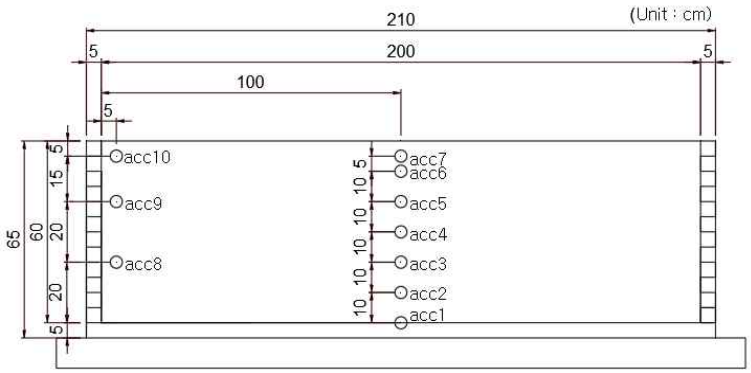

(a) Accelerometers setting in flat model

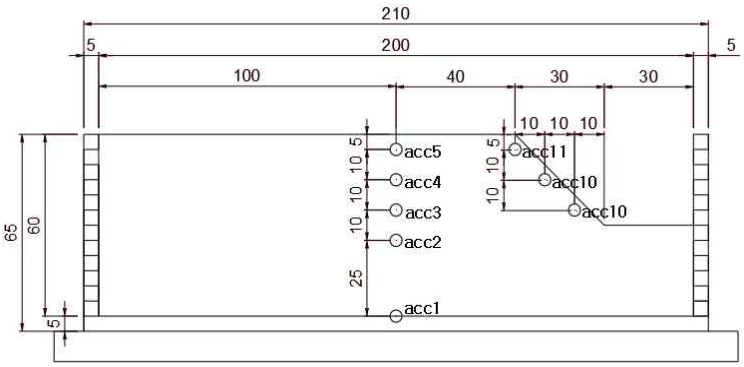

(b) Accelerometers setting in flat model

Figure 3.5 Accelerometers setting in the ground.

3.3 Seismic wave

The sine waves that are selected are 10HZ with Peak Ground Acceleration(PGA) is equai to 0.07 g and 8HZ with PGA is equal to 0.05g. The artificial seismic wave is the synthetic seismic wave combining the Gyeongju - Pohang earthquakes, using the empirical Green's function on the basis of the raw data measured in the Kori Nuclear Power Plant. Because of the rarity of earthquakes, modified ground motions are often required as inputs. The input of bedrock ground motion for soil layer seismic response analysis generally adopts two forms at present. One is to directly use the actual strong earthquake record, but also can be adjusted and modified appropriately. Second, the use of synthetic ground motion as we called artificial wave. As the artificial seismic wave has different periodic components, high amplification occurs. This is why the artificial seismic wave was selected to evaluate the effects of boundary conditions in the case of high amplification.

Chapter 4. Introduction to numerical analysis

4.1 Seismic response analysis

For site seismic resistance, the characteristics of ground motion can be represented by the amplitude and frequency spectrum of the ground motion. Amplitude usually refers to the maximum acceleration, velocity or displacement of a ground motion. Spectrum is usually referred to as response spectrum. For different characteristics of ground motion input, the site will produce different response results. In the site seismic response analysis, the surface acceleration displacement and response spectrum are important parameters that characterize the ground motion characteristics, and they are necessary in the seismic safety evaluation. The parameters are the necessary basis for engineering seismic design.

Peak ground acceleration (PGA) and response spectrum acceleration (SA) are important parameters to characterize ground motion in site seismic response analysis. They are necessary parameters in seismic safety evaluation and necessary basis for engineering seismic design. Peak ground acceleration is equal to the maximum ground acceleration that occurred during earthquake shaking at a location. PGA is equal to the amplitude of the largest absolute acceleration recorded on an accelerogram at a site during a particular earthquake (Douglas, 2003). Spectral acceleration is a unit measured in g (the acceleration due to Earth's gravity, equivalent to g-force) that describes the maximum acceleration in an earthquake on an object - specifically a damped, harmonic oscillator moving in one physical dimension. This can be measured at (or specified for) different oscillation frequencies and with different degrees of damping, although 5% damping is commonly applied.

This chapter uses DEEPSOIL program and ABAQUS program to analyze and compare different types of seismic input motion.

4.2 DEEPSOIL program

In order to perform nonlinear analysis in the time domain, many scholars have researched and developed a series of time-domain nonlinear method calculation programs. In this thesis, the DEEPSOIL program is used as the time-domain nonlinear method calculation program. DEEPSOIL is a unified one-dimensional equivalent linear and nonlinear site response analysis program. 1-D nonlinear and equivalent linear analysis can be performed. It adopts the modified hyperbolic constitutive model mentioned above (Darendeli, 2001). Nonlinear site analysis is rarely applied in engineering practice, because it is difficult to determine parameters for nonlinear programs, which often vary from person to person, and the influence of parameter changes on analysis results has not been thoroughly understood and studied. The DEEPSOIL program fits the data well and produces good results.

4.2.1 Modeling in DEEPSOIL

Creating a 1-D field is shown in Figure 4.1 in DEEPSOIL. The first and second layers are five centimeters, and the third to seventh layers are ten centimeters. There is exactly one accelerometer between each two layers, and the designed 1-D site model is shown in Figure 4.1.

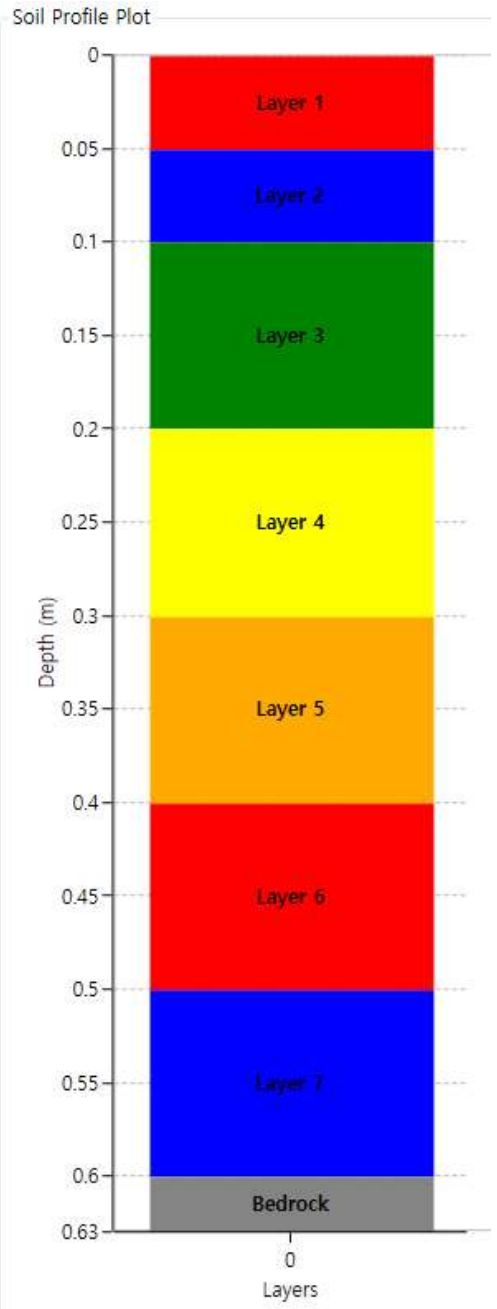

Figure 4.1 1-D site model in DEEPSOIL.

4.2.2 Darendeli model in DEEPSOIL

Darendeli model is a nonlinear model. Darendeli model uses shear strain to calculate the normalized shear modulus. The shear modulus G decreases with the increase of strain amplitude. Small strain shear modulus, usually expressed as G_{max} or G_0..The relationship between shear modulus and shear strain amplitude is typical, and its normalized modulus reduction curve is shown in Figure. 4.2a.

The nonlinear stress-strain relationship leads to an increase in energy dissipation, so the material damping ratio D increases with the increase in strain amplitude. The damping ratio of a material under small strain is called D_{min}. The typical feature of the relation between material damping ratio and strain amplitude is material damping curve, as shown in Figure 4.2b.

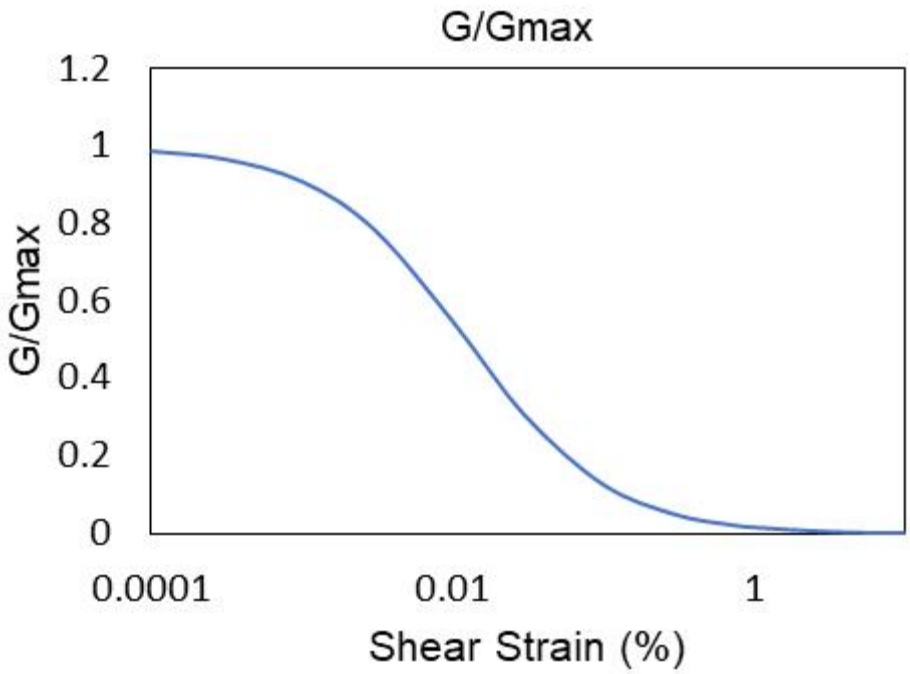

(a) Normalized modulus reduction

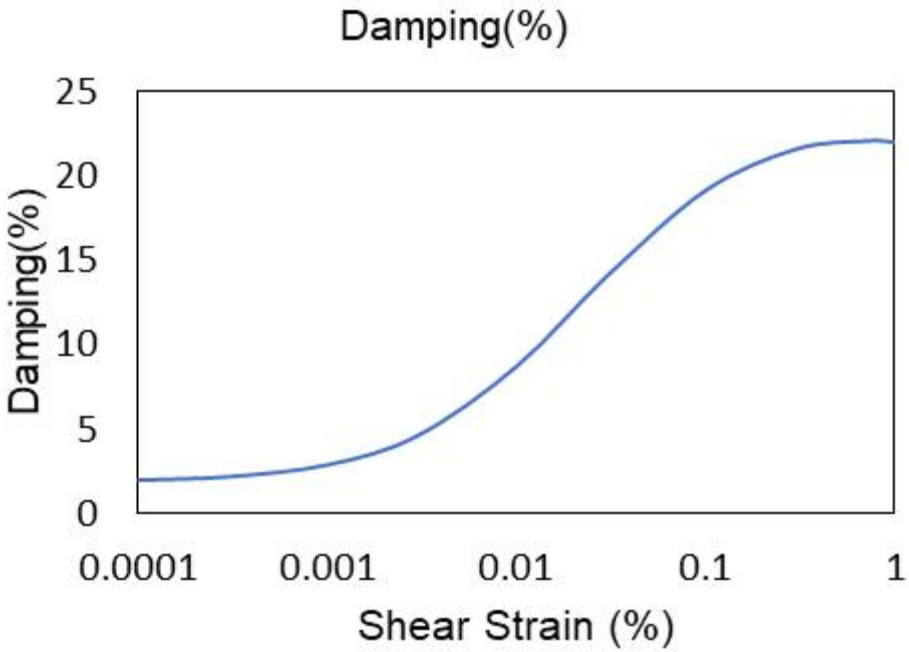

(b) Material damping curves

Figure 4.2 Linear elastic, nonlinear elastic and plastic strain ranges on (a) normalized modulus reduction and (b) material damping curves.

4.3 Modeling in ABAQUS

4.3.1 Main modeling steps

ABAQUS is a powerful finite element program for engineering simulation, which can solve problems ranging from relatively simple linear analysis to many complex nonlinear problems. ABAQUS has a constitutive model that can truly reflect the properties of the soil, and can accurately establish the initial stress state, which has strong applicability to geotechnical engineering. The modules and functions of ABAQUS are shown in Table 4.1.

Table 4.1 The modules and functions of ABAQUS

MODULUS	FUNCTION
Part	Draw geometric shapes, and generate frame parts
Property	Define the material parameters and the cross-sectional properties of the frame
Assembly	Assemble the model and generate assembly parts
Step	Arrange the analysis sequence and put forward output requirements
Interaction	Add constraints
Load	Apply load and boundary conditions
Mesh	Finite element meshing of the frame
Optimization	Post-processing module
Job	Generate a job and submits it for analysis
Visualization	Observe and analyze the results
Sketch	Generate parts

4.3.2 Geostatic stress balance

Firstly, the geostatic stress analysis was carried out, and the vertical settlement reached 10^{-7}m after balancing the geostatic stress, as shown in Figure 4.3. This result indicated that the modeling could ignore the influence of the gravity of the sand on the test.

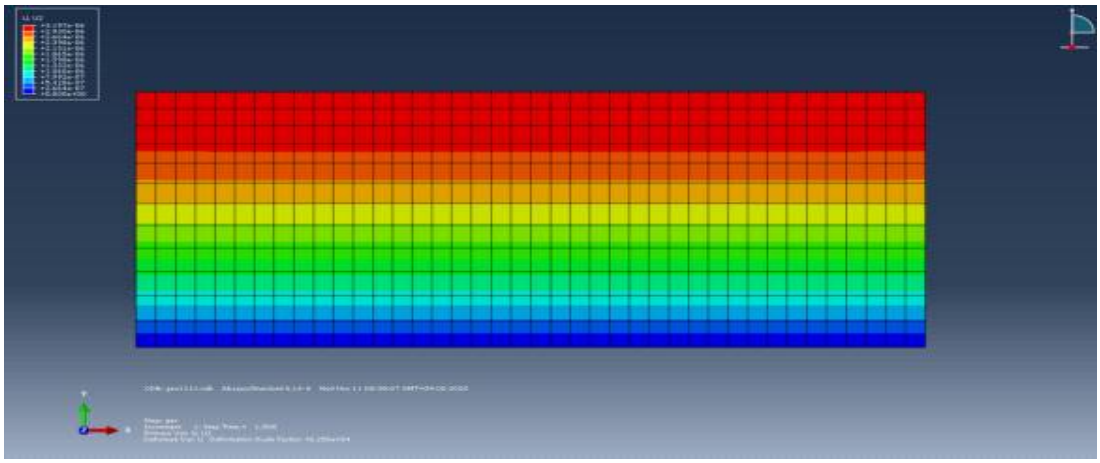

(a) Normalized modulus reduction

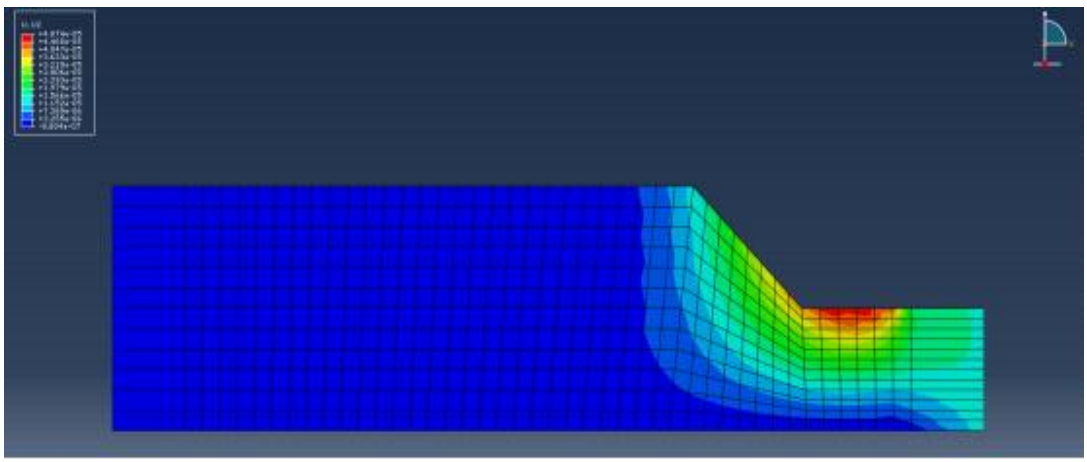

(b) Material damping curves

Figure 4.3 Geostatic stress balance in ABAQUS.

4.3.3 Mohr-Coulomb model in ABAQUS

The soil constitutive model used in this study is the Mohr-Coulomb model, which can be expressed as follows:

$$\tau = c + \sigma \tan\phi \tag{4.1}$$

Where, τ = shear strength

c = cohesion

ϕ = internal friction angle

σ = normal stress.

Using Mohr's law, equation 4.1 can be extended to the plane stress state to become Mohr-Coulomb Conditions Figure 4.4.

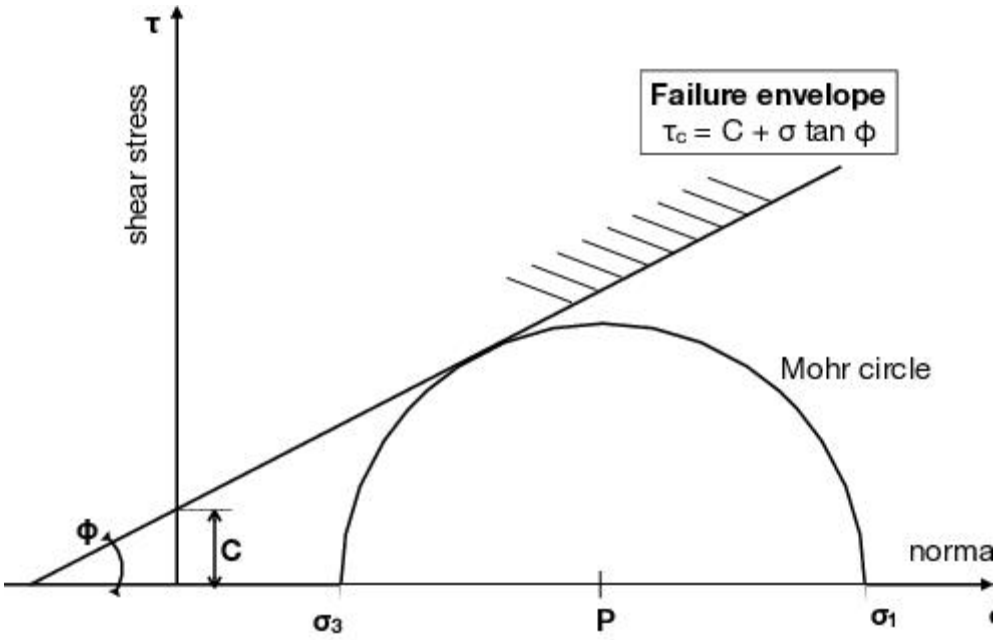

Figure 4.4 The Mohr-Coulomb failure criteria and Mohr's circle.

When the Mohr-Coulomb yield criterion is expressed by the principal stress in the plane, the equation can be written as:

$$\frac{1}{2}(\sigma_1-\sigma_3)+\frac{1}{2}(\sigma_1+\sigma_3)\sin\phi-c\cos\phi=0 \qquad (4.2)$$

In the π plane, the Mohr-Coulomb yield criterion is a hexagon with unequal angles, as shown in Figure 4.5. In the principal stress space, the yield surface of the Mohr-Coulomb yield criterion is a pyramid surface, and the central axis

coincides with the isoclinic line.

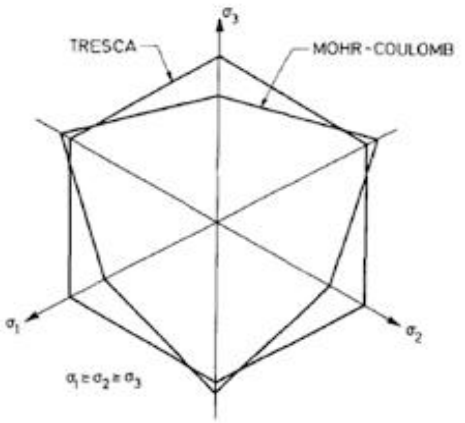

Figure 4.5 Mohr-Coulomb yield surface.

The model ground was configured with a total cross-sectional depth of 60cm according to the actual size of the model experiment. Two layers of 5cm thick were defined from the surface to the depth of 10cm, and the other layers were divided into 5 layers of 10cm thick from 10cm to the depth of 60cm. The unit weight of each layer was applied at 14.72 kN/m^3 in the same manner as in the shaking table test. Shear strength was calculated by depth according to the Mohr-Coulomb failure envelope and applied to each layer. The shear wave velocity was calculated for each layer according to the equation proposed by Kaklamanos et al (2018).

$$V_s(z) = \overline{V_s}\left[\frac{\sigma'_\nu(z)}{\overline{\sigma'_\nu}}\right]^n \tag{4.3}$$

Where: $V_s(z)$ = shear wave velocity at depth z

$\overline{V_s}$ = average shear wave velocity

σ'_{ν} = effective vertical stress at depth z

$\overline{\sigma'_{\nu}}$ = effective vertical stress calculated in the middle of the floor

n = stress index.

For the stress index, 1/4 is used for clay, silt and sandy soil, and 1/3 is used for gravel and rock. Since this sample is of sand, 1/4 was applied to the stress index. The average shear wave velocity was determined to be 66.87m/s by combining the hammer test and the calculation formula of Hardin and Richart (1963). The dynamic characteristic curve was applied by fitting the Darendeli (2001) curve with the MRDF (modulus reduction and damping curve fitting procedure using the reduction factor) method. The lower boundary of the model was applied as a rigid half-space in consideration of the stiffness of the bottom surface of the soil.

In a homogeneous and isotropic soil, the speed of the shear wave is controlled by the elastic modulus, as shown in equation 4.4.

$$G = \rho V_s^{\,2} \tag{4.4}$$

Where, G=shear modulus

ρ=the unit weight of soil

V_s =shear wave velocity.

The relationship between elastic modulus and shear modulus is:

$$G = \frac{E}{2(1+\nu)} \tag{4.5}$$

Where, G=shear modulus

E=elastic modulus

ν=Poisson's ratio.

According to equation(4.4) and equation (4.5), knowing the unit weight of soil, ρ=1.47x10^{5}N/m^3 and shear wave velocity, V_s =72m/s. The shear modulus can be

obtained as $7.6x10^7$Pa. Then knowing the shear modulus, G=$7.6x10^7$Pa, and the poisson's ratio,ν=0.3, the elastic modulus can be obtained as $2x10^8$Pa. This modulus was used in the study.

The Mohr-Coulomb model includes five parameters, elasticity modulus E and Poisson's ratio ν, internal friction angle, cohesion, and dilatancy angle. The Mohr-coulomb model is a first-order approximation result to describe the behavior of rock and soil. It is often used in the preliminary analysis or simplified analysis of the problem. The average stiffness calculated by the Mohr-Coulomb model is constant, and the estimated value of the complex deformation problem can be obtained finally. Because the Mohr-Coulomb yield surface has singular points such as spires and corners, the numerical calculation becomes complicated and the convergence is slow in ABAQUS.

4.3.4 The boundary conditions

Artificial boundary conditions have a direct impact on the accuracy of numerical simulation of near-field fluctuations, so the study of artificial boundary conditions is of great significance. In this study, three models are established in the process of time-domain acceleration response analysis of seismic waves. They are finite boundary model, viscoelastic boundary model and infinite boundary model.

Liu et al(2006) proposed the calculation results obtained from inside vibration source and the fixed boundary, the distortion and disturbances appear; the results calculated by the method mentioned above are compared with the results of viscoelastic boundary, which make it certain that the filter function of outgoing scattered wave with the method mentioned above is better than viscoelastic boundary. Modeling is shown in Figure(4.7). Therefore, the improved ABAQUS dynamic infinite element boundary method is effective and has certain stability.

Because it is a 2D model, there are only horizontal and vertical boundaries. The boundary is the bottom only has the horizontal direction acceleration and can not carry on the vertical direction motion. In order to eliminate the impact of boundary

on model analysis results, the two sides of boundary are redesigned infinite boundaries, as shown in Figure 4.6.

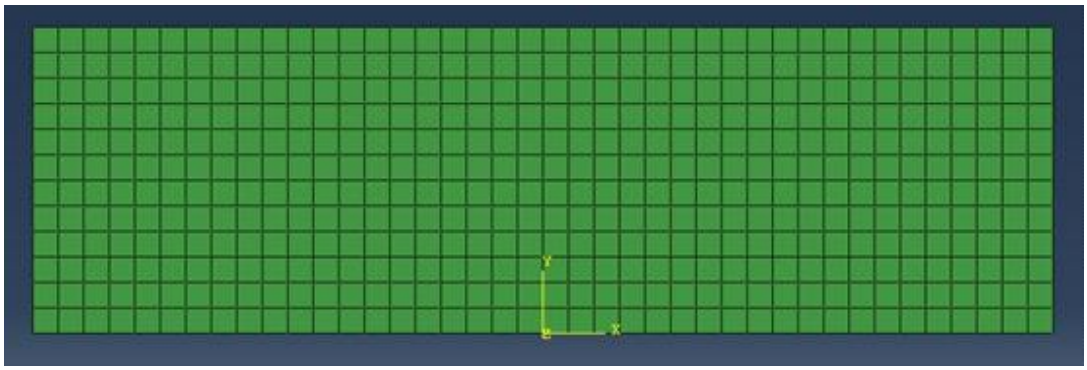

(a) Finite boundary model(flat)

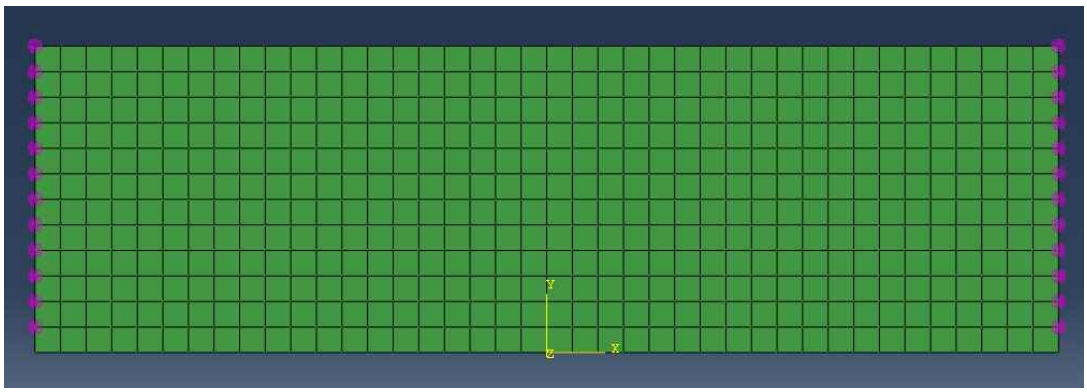

(b) Viscoelastic boundary model(flat)

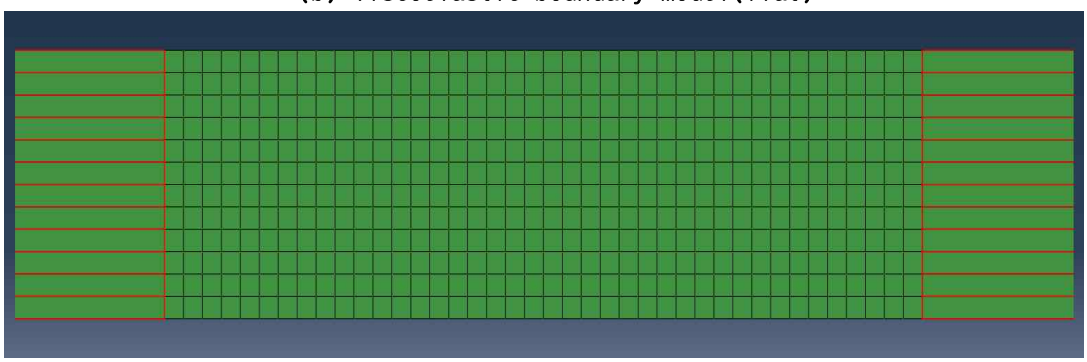

(c) Infinite boundary model(flat)

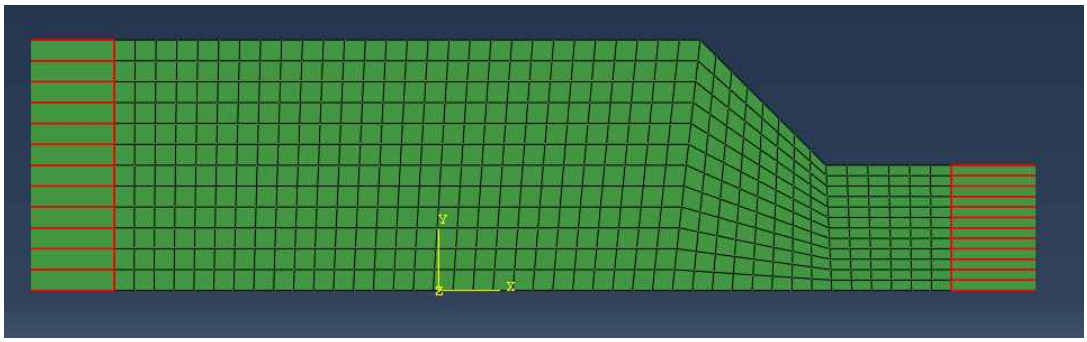

(d) Infinite boundary model(slope)

Figure 4.6 Boundary settings and comparisons in ABAQUS.

4.4 Comparison of DEEPSOIL and ABAQUS programs

As mentioned above, DEEPSOIL is a 1-D infinite half-space program. ABAQUS is a multi-dimensional modeling program. In this study, the main difference between the two programs is the constitutive model. Figure 4.7 (a) and (b) show the shear stress-shear strain curves of Darendeli model and Mohr-Coulomb model. DEEOSOIL uses the Darendeli nonlinear model, while ABAQUS uses the Mohr-Coulomb linear model. Figure 4.7 (c) and (d) are the Darendeli model and Mohr-Coulomb model $G/G_{\max}$-shear strain curve. The Darendeli model is that $G/G_{\max}$ decreases with the increase of shear strain, and the transition from linear elasticity to non-linear elasticity to unlimited plasticity. The $G/G_{\max}$- shear strain of the Mohr Coulomb model does not change with the increase of strain. Figure 4.7 (e) and (f) show the Darendeli model and Mohr-Coulomb models using hysteresis curves to calculate the damping ratio. In the Darendeli model, the nonlinearity of shear stress and shear strain will increase energy consumption. Therefore, the damping ratio will increase as shear strain increase. The Mohr-Coulomb model stress-strain curve is linear, so the damping ratio is basically unchanged.

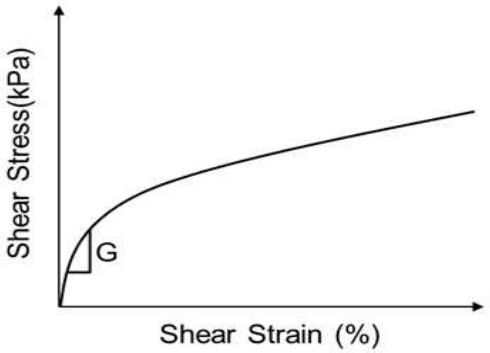

(a) Shear modulus in Darendeli model

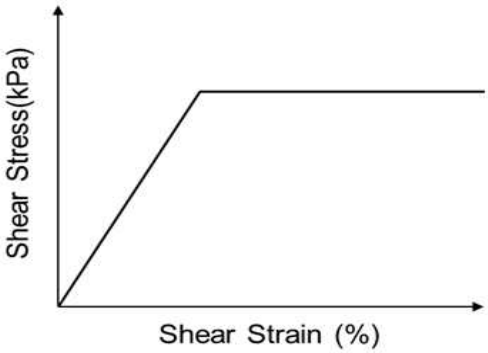

(b) Shear modulus in Mohr-Coulomb model

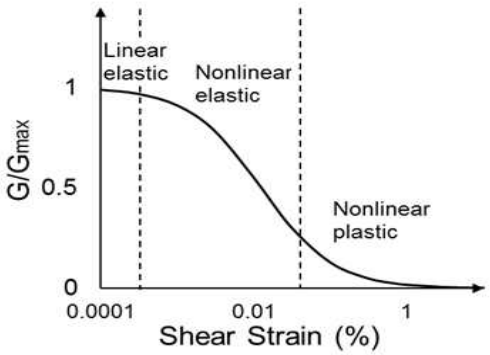

(c) Normalized shear modulus in Darendeli model

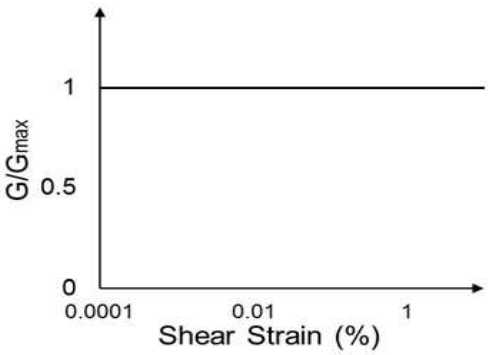

(d) Normalized shear modulus in Mohr-Coulomb model

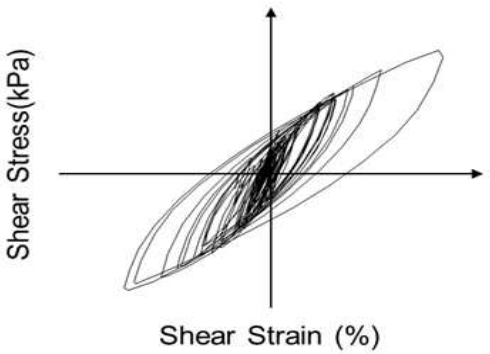

(d) Material damping ratio with shearing strain in Darendeli model

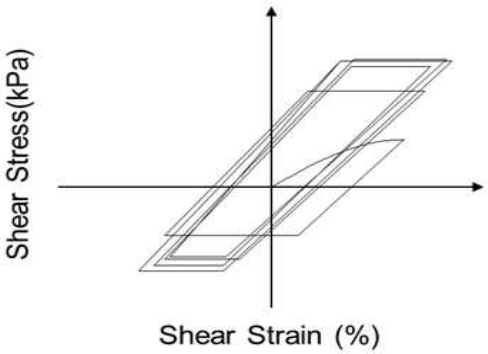

(e) Material damping ratio with shearing strain in Mohr-Coulomb model

Figure 4.7 Comparison of (a) Shear modulus, (b) Normalized shear modulus, (c) Material damping ratio with shear strain under different models.

Chapter 5. Comparison and evaluation of shaking table test with numerical analysis

The behavior characteristics of laminar shear box in the 1g shaking table test were compared with the numerical analysis results using DEEPSOIL and ABAQUS. Experiments and analysis values were compared and evaluated using Acceleration-time history, Peak Ground Acceleration (PGA) and Spectral Acceleration (SA). The experimental values were obtained from accelerometers installed by depth in the center(or slope) of the laminar shear box of the 1g shaking table test. The analysis value of DEEPSOIL was obtained at the same depth as the accelerometer buried in the 1g shaking table test after modelling the semi-infinite ground having the property values of the experiment and performing 1D analysis. In ABAQUS, the ground model used in the shaking table test was modeled In the actual size and the boundary condition was set as the Infinite boundary. Then, the analysis value in ABAQUS was obtained at the same location as the location where the accelerometer was buried in the 1g shaking table test.

The Peak Ground Acceleration means the maximum acceleration recorded while the ground has moved by dynamic load. The input motion of the shaking table test is applied to the numerical analysis model, the Peak ground acceleration at each depth of the experimental and numerical model was compared.

The response of the ground to the dynamic load depends on the natural frequency of the ground and the frequency of the earthquake motion. The response spectrum plots the maximum response to seismic motions with different frequency components, and when the response variable is acceleration, it is called an acceleration response spectrum or Spectral acceleration. Spectral acceleration is represented the maximum response acceleration that a dynamic load gives to the vibration system of various periods. Using this characteristic, it is possible to confirm the amplification occurring in a frequency period other than the dynamic load used in the experiment. Therefore, using the response spectral acceleration, it

is possible to confirm amplification characteristics that are not visible with the 8, 10Hz sine wave used in this experiment.

5.1 Comparison of flat ground with normal elastic modulus

5.1.1 Acceleration-time history

Figure 5.1 shows the Acceleration-time history graph of the experiment and analysis by the same input motion.

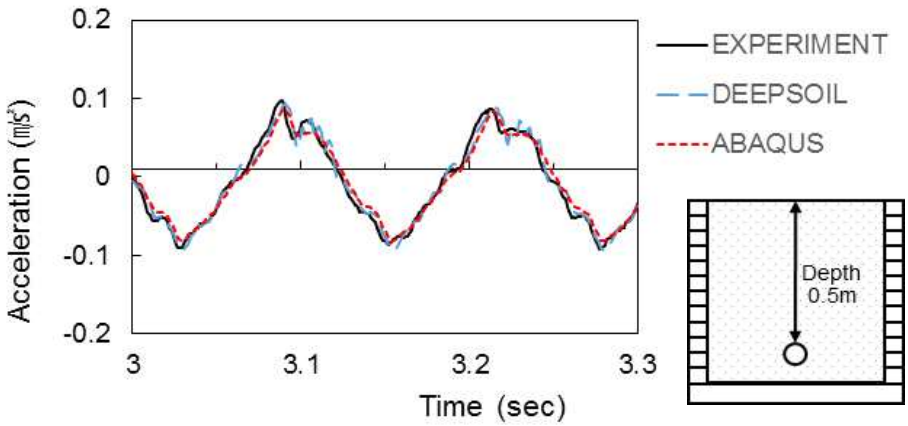

(a) Part of acceleration-time history graph of Sine 8Hz at depth 0.5m

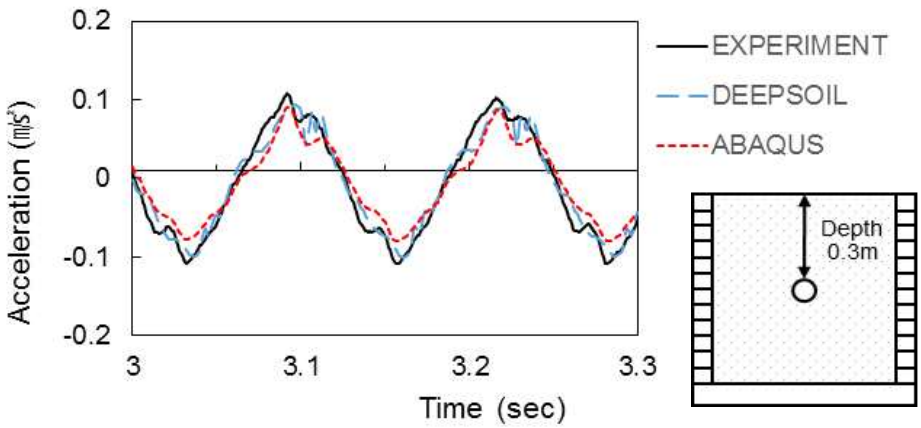

(b) Part of acceleration-time history graph of Sine 8Hz at depth 0.3m

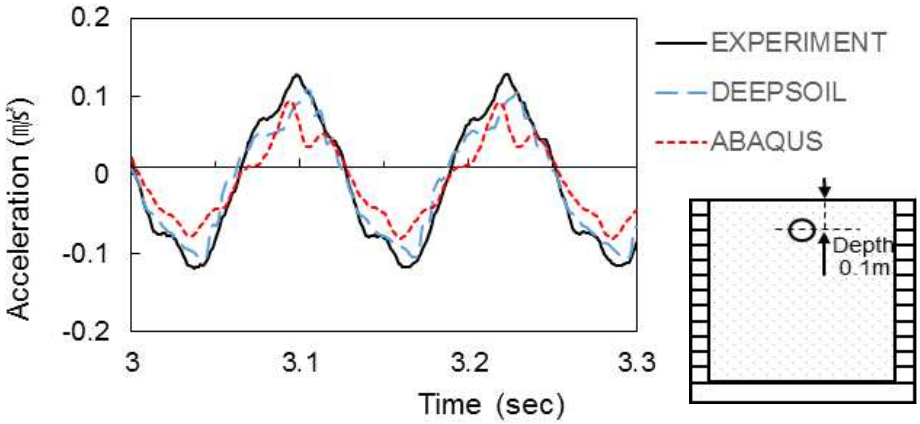

(c) Part of acceleration-time history graph of Sine 8Hz at depth 0.1m

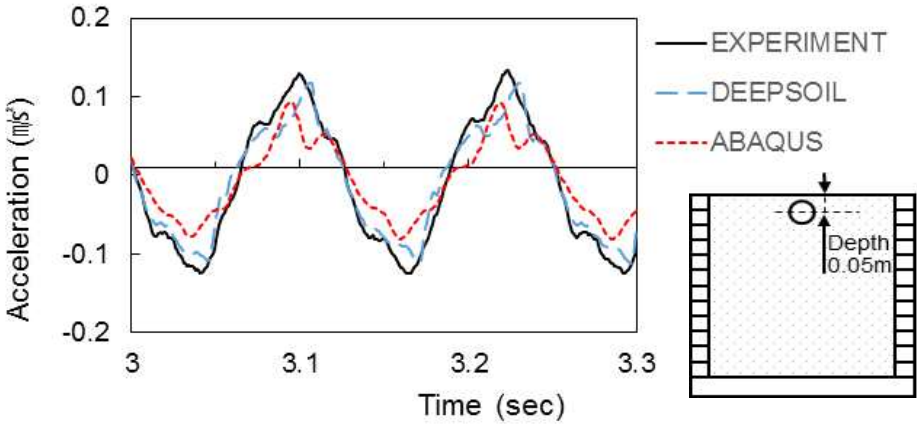

(d) Part of acceleration-time history graph of Sine 8Hz at depth 0.05m

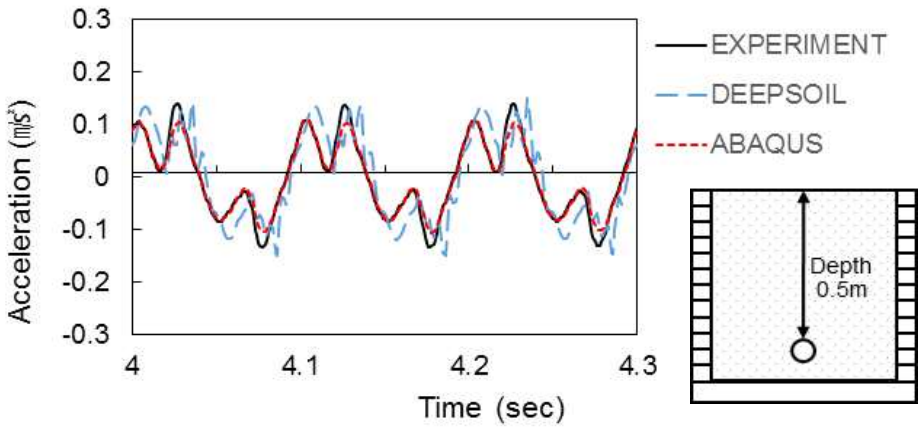

(e) Part of acceleration-time history graph of Sine 10Hz at depth 0.5m

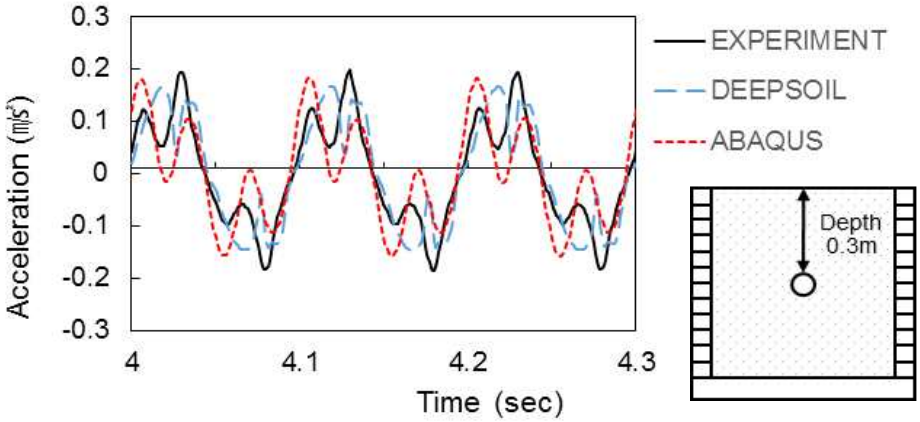

(f) Part of acceleration-time history graph of Sine 10Hz at depth 0.3m

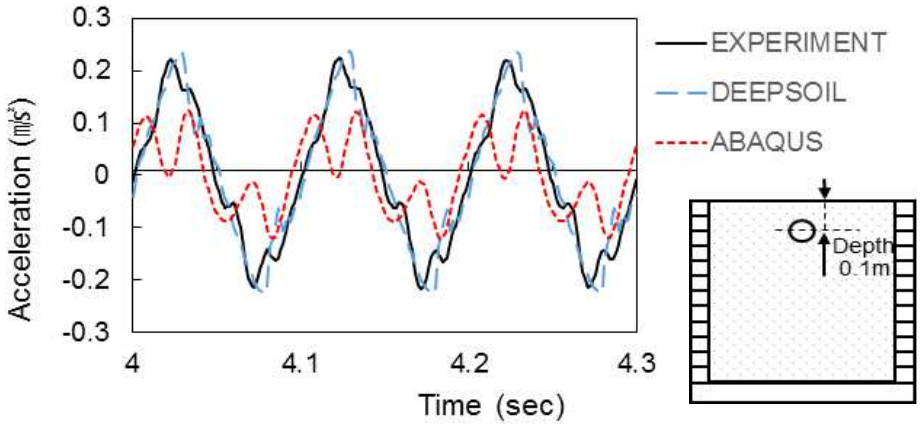

(g) Part of acceleration-time history graph of Sine 10Hz at depth 0.1m

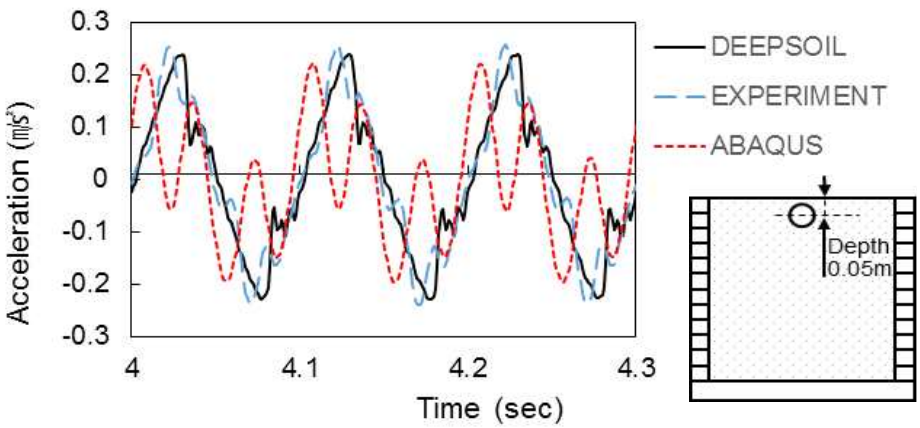

(h) Part of acceleration-time history graph of Sine 10Hz at depth 0.05m

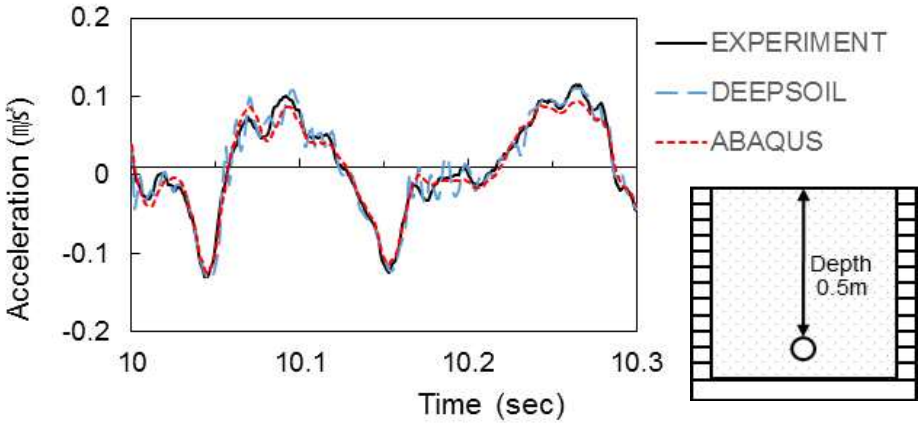

(i) Part of acceleration-time history graph of Artificial wave at depth 0.5m

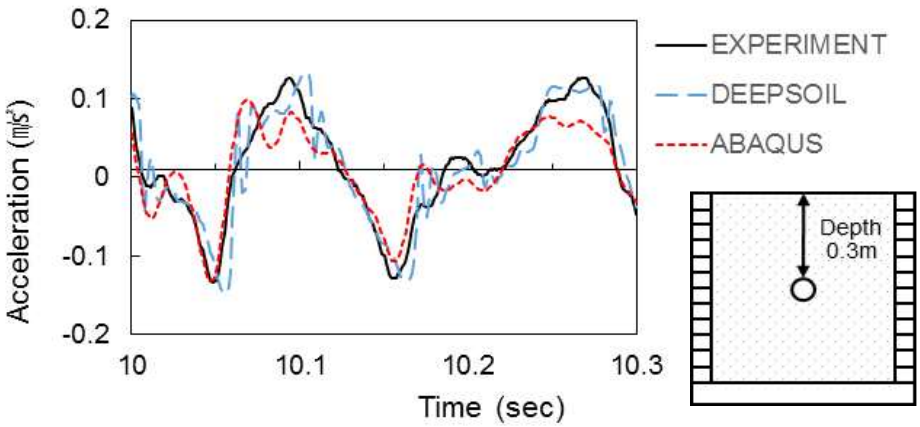

(j) Part of acceleration-time history graph of Artificial wave at depth 0.3m

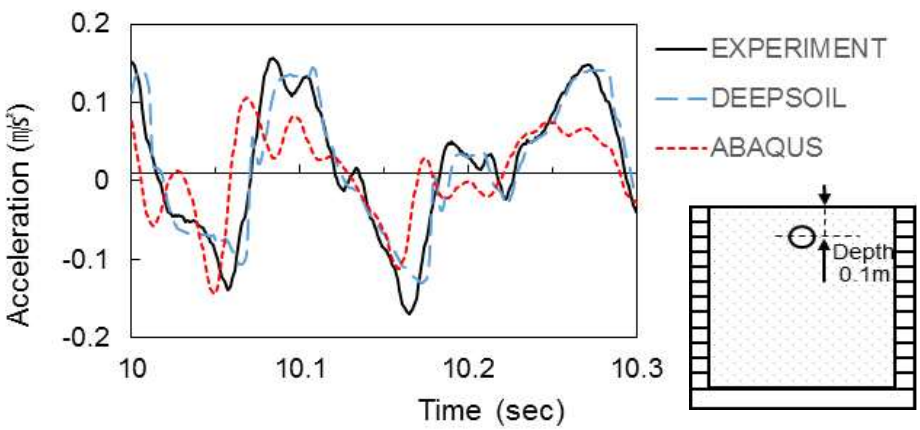

(k) Part of acceleration-time history graph of Artificial wave at depth 0.1m

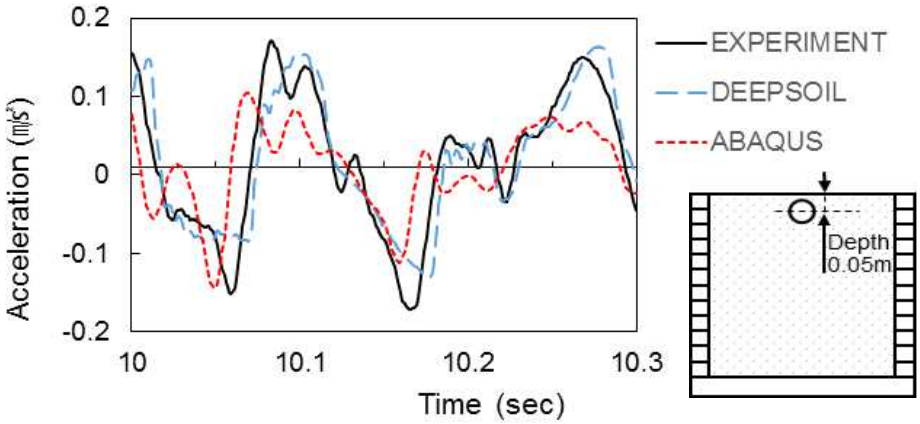

(l) Part of acceleration-time history graph of Artificial wave at depth 0.05m

Figure 5.1 Part of acceleration-time history graph for experiment and analysis.

Overall, near the bottom, both experimental and analyzed values show similar time history. However, as it goes to the top of the model, it was confirmed that the time history of the experiment and analysis were slightly different as shown in Fig. 5.1(a) to Fig. 5.1(d). This is expected because the small noises are closer to the top, the more short-period frequency components are added to the overall curve and the amplification difference increases. The short-period frequency components included in the input motion had a minimal effect on the lower part, but the effect on the amplification accumulated toward the upper part of the model is judged to affect the time history graph curve. However, since these short-period frequency components do not coincide with the main amplification period of the model, this effect is unlikely to have a significant effect on Peak ground acceleration and spectral acceleration analysis.

5.1.2 Peak ground acceleration profile

Figure 5.2 is the ground acceleration profile by each input motion and depth.

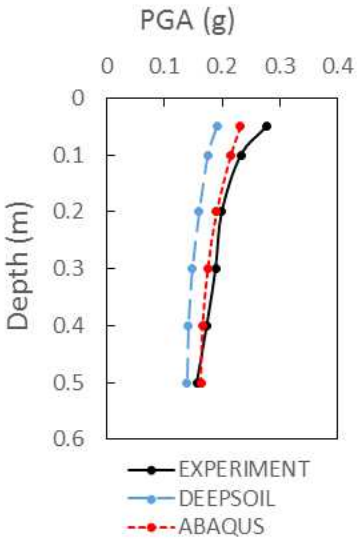

(a) Peak ground acceleration profile by Sine 8Hz

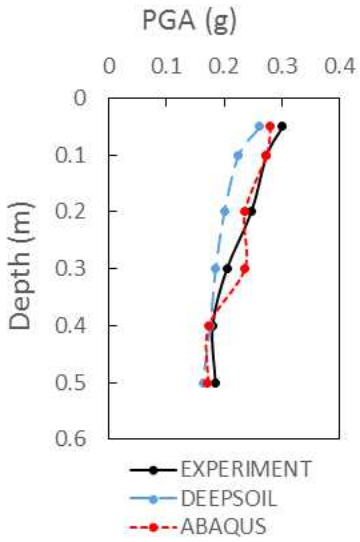

(b) Peak ground acceleration profile by Sine 10Hz

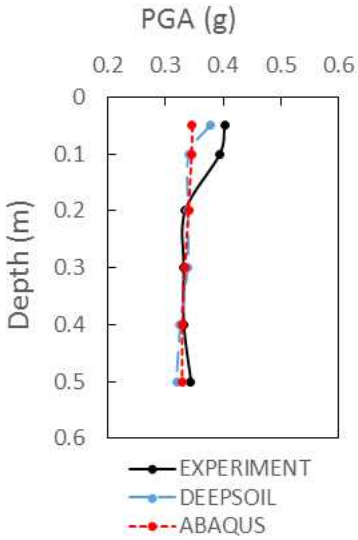

(c) Peak ground acceleration profile by Artificial wave

Figure 5.2 Peak ground acceleration profile for experiment and analysis.

In the ground acceleration profile in Figure 5.2, experiment and analyze results showed a consistently tendency to increase as the depth became shallower. In this case, ABAQUS nearly coincided with the ground acceleration of experiment and

predicted the ground acceleration better than DEEPSOIL.

5.1.3 Spectral acceleration

Figure 5.3 shows the Spectral acceleration measured by depth in the 1g shaking table test and the Spectral acceleration obtained from DEEPSOIL and ABAQUS.

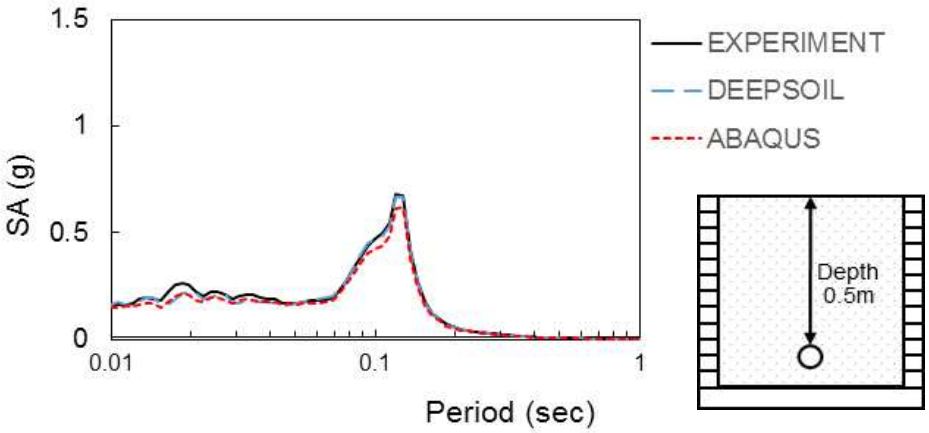

(a) Spectral acceleration by Sine 8Hz at depth 0.5m

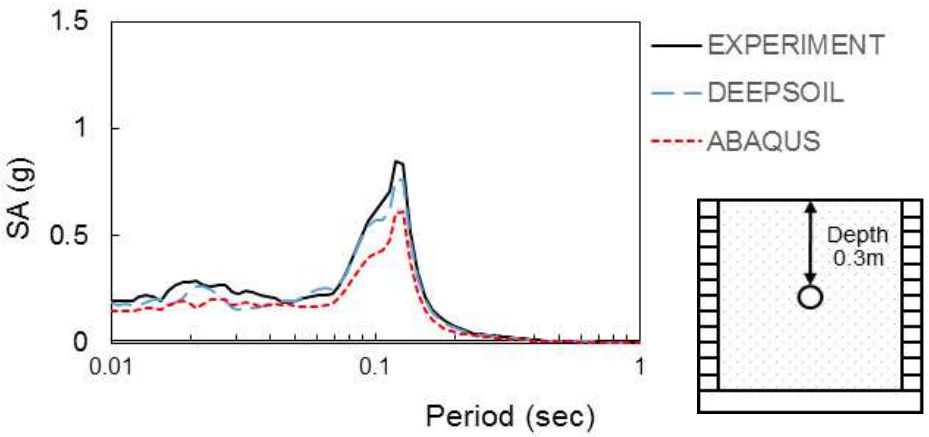

(b) Spectral acceleration by Sine 8Hz at depth 0.3m

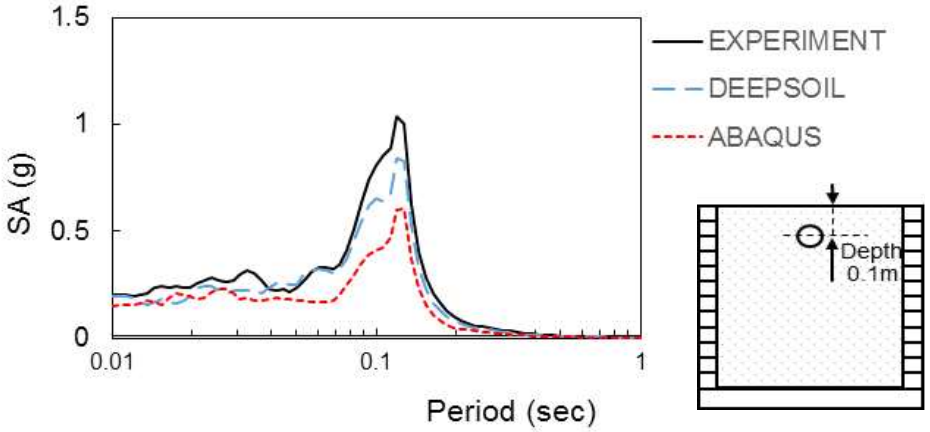

(c) Spectral acceleration by Sine 8Hz at depth 0.1m

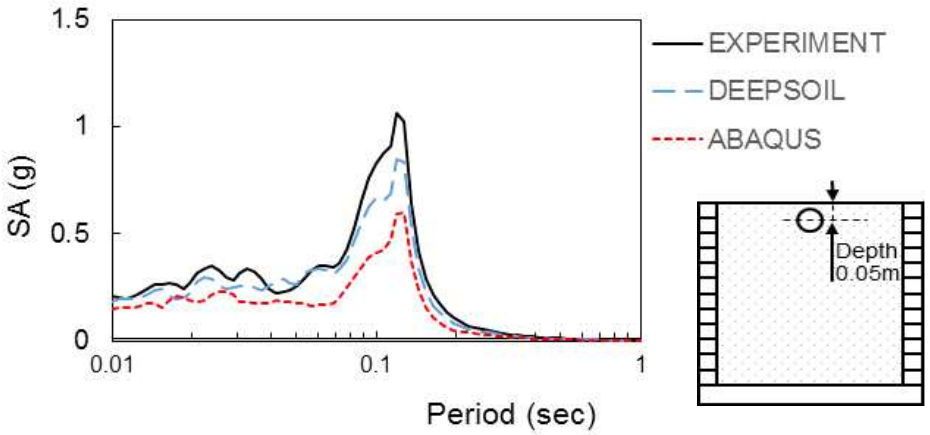

(d) Spectral acceleration of Sine 8Hz at depth 0.05m

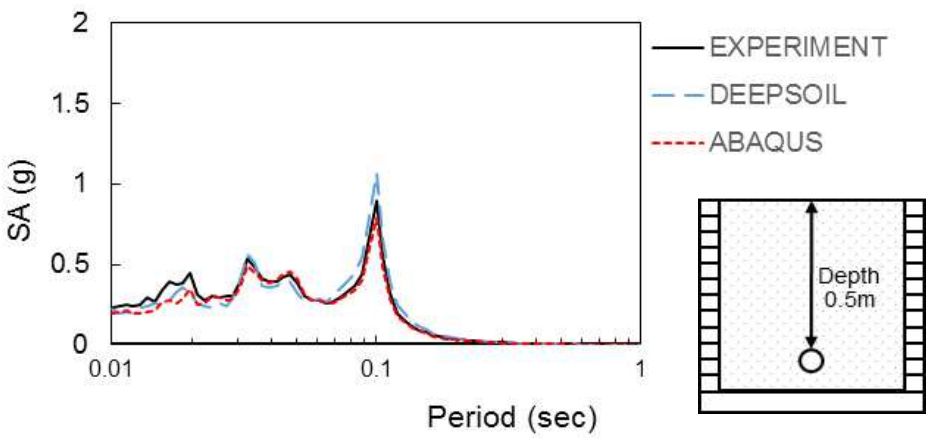

(e) Spectral acceleration by Sine 10Hz at depth 0.5m

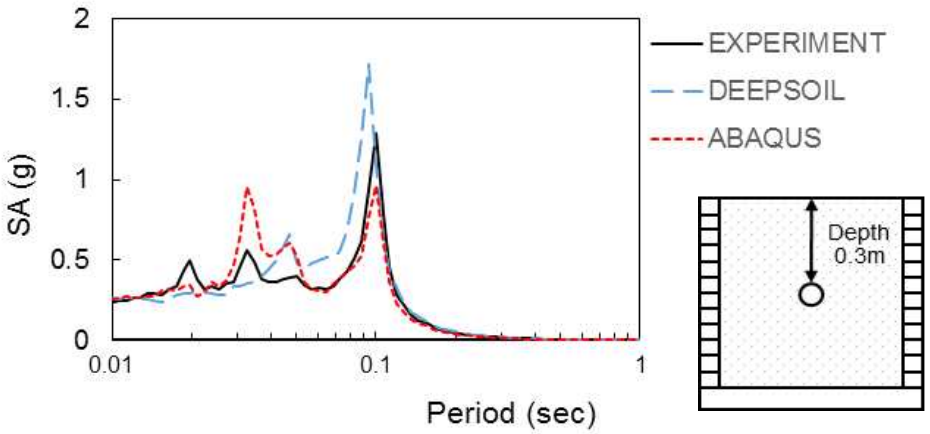

(f) Spectral acceleration by Sine 10Hz at depth 0.3m

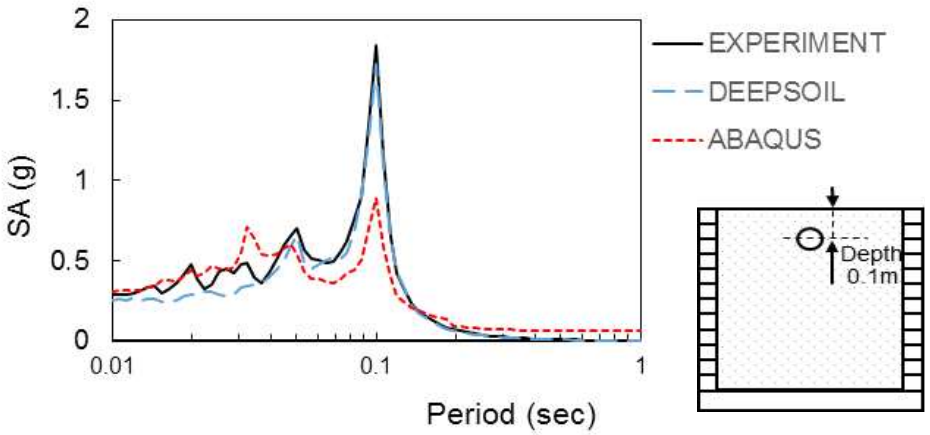

(g) Spectral acceleration by Sine 10Hz at depth 0.1m

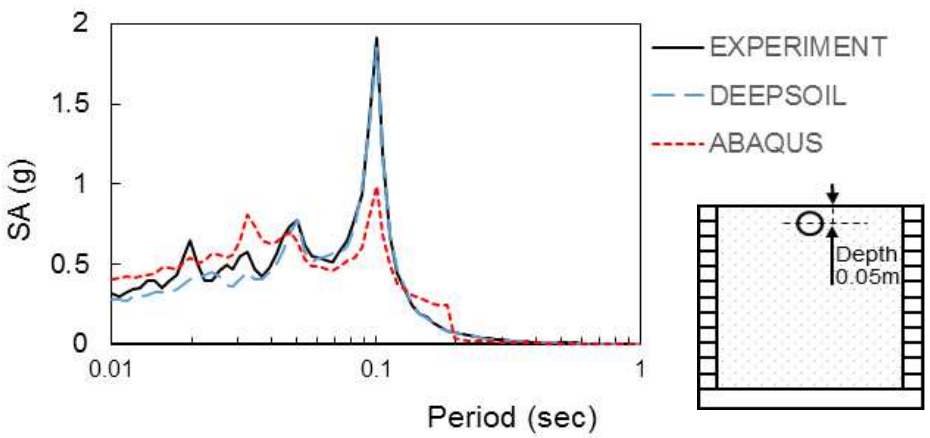

(h) Spectral acceleration by Sine 10Hz at depth 0.05m

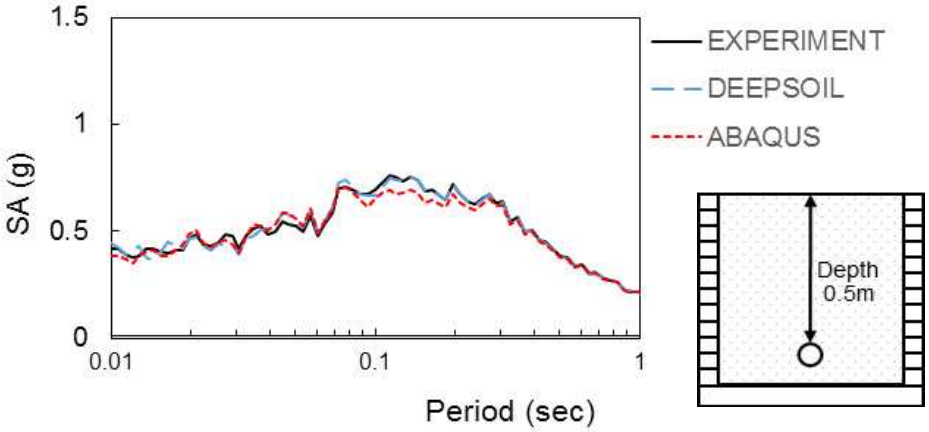

(i) Spectral acceleration by Artificial wave at depth 0.5m

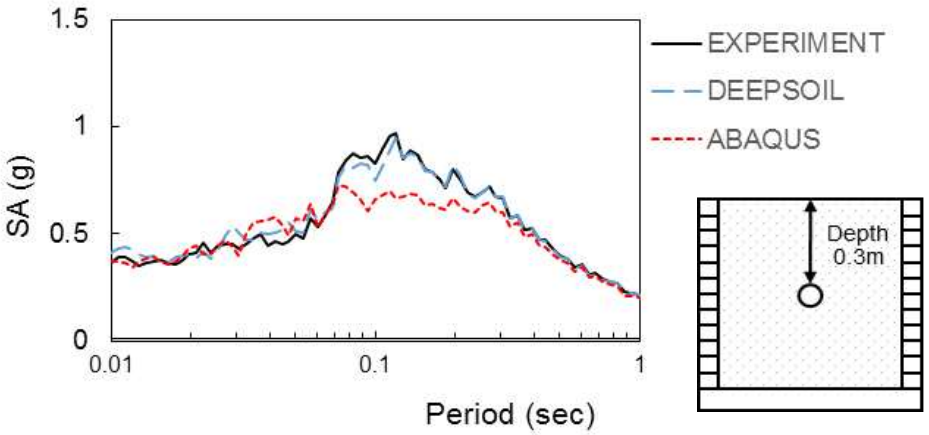

(j) Spectral acceleration by Artificial wave at depth 0.3m

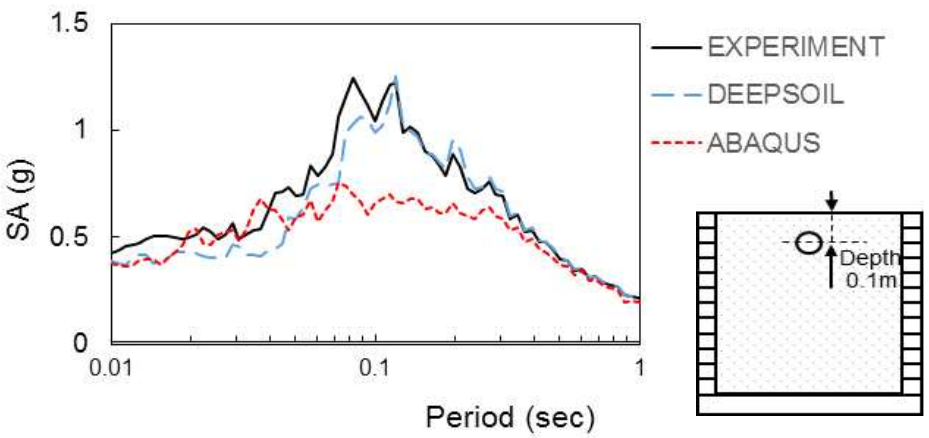

(k) Spectral acceleration by Artificial wave at depth 0.1m

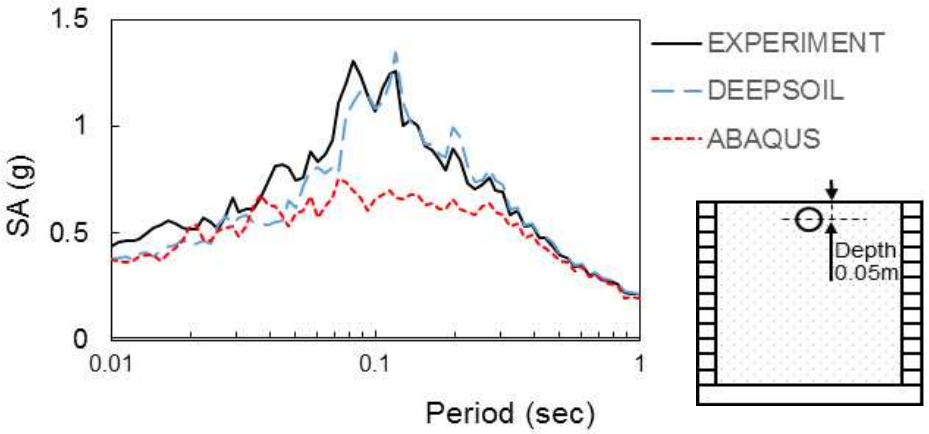

(l) Spectral acceleration by Artificial wave at depth 0.05m

Figure 5.3 Spectral acceleration for experiment and analysis.

Figure 5.3(a) to Figure 5.3(d) are the Spectral acceleration graphs of the experiment and analysis for sine 8Hz. As the depth became shallower from 0.5m to 0.05m, the greater the difference occur between the experiment and analysis. As the depth became shallower, the Spectral acceleration of analysis was amplified to be lower than the Spectral acceleration of experiment. Figure 5.3(e) to Figure 5.3(h) are the Spectral acceleration graphs of the experiment and analysis for sine 10Hz. Near the bottom of the model, DEEPSOIL amplifies slightly higher than the 1g shaking table test, and ABQUS amplifies low. In Spectral acceleration at a depth of 0.2m to the surface, DEEPSOIL predicted the very similar the 1g shaking table test and ABAQUS amplified somewhat lower. Figure 5.3(i) to Figure 5.3(l) are the Spectral acceleration graphs of the experiment and analysis for artificial wave. Overall, ABAQUS was amplified low, so the gap of Spectral acceleration between the shaking table test and analysis increased from bottom to surface. The analysis of DEEPSOIL was very similar with the Spectral acceleration graph of the shaking table test at all depth.

In the above Spectral acceleration figures, the main amplification period of the ground is 0.08sec-0.12sec, so the main amplification period is determined to be 10Hz.

In Figure 5.3(e) to Figure 5.3(h) using sine 10Hz input motion coinciding with the natural frequency of the ground and Figure 5.3(i) to Figure 5.3(l) using artificial wave input motion containing various frequency components, the spectral curves of the experiment and analysis of DEEPSOIL were almost identical and the maximum amplification was also the same. In the behavior characteristics of the ground, acceleration and Spectral acceleration are used as important parameters for dynamic ground analysis, so it is important to predict the value meaningfully. In the above, ground acceleration predicted very similar analysis of ABAQUS, but the Spectral acceleration curve predicted similarly by analysis of DEEPSOIL.

Therefore, in order to verify the behavior characteristic of ground and dynamic experiment like shaking table test, it would be reasonable to use both analysis programs and to compare comprehensively.

5.2 Comparison of flat ground with adjusted elastic modulus

The effect of using elastic modulus in Chapter 5.1 is not very ideal on the Spectrum acceleration reflection. An adjusted modulus of elasticity is introduced. The actual elasticity modulus is reduced by ten times and getting the following curves of Acceleration-time history and Spectrum acceleration. Because of the uncertainty and instability of the peak ground acceleration, it is not useful to use the peak ground acceleration in this case.

In general, the soil stiffness and elastic modulus depends on the consistency and packing (density) of the soil. Typical values of soil elastic modulus are given below as guideline. Elastic modulus for sandy soils changes with depth, because this is affected significantly by overburden pressure. This data has been recognized by many researchers, so the adjusted shear modulus is $2x10^7$Pa.

Table 5.1 Typical values of elastic modulus for granular material (MPa) (Based on Obrzud and Truty, 2012. Complied from Kezdi, 1974 and Prat et al. 1995)

USCS	Description	Loose	Medium	Dense
GW .SW	Gravels/Sand well-graded	30-80	80-160	160-320
SP	Sand, uniform	10-30	30-50	50-80
GM ,SM	Sand/Gravel silly	7-12	12-20	20-30

5.2.1 Acceleration-time history

Figure 5.4 shows the Acceleration-time history graph of the experiment and analysis by the same input motion.

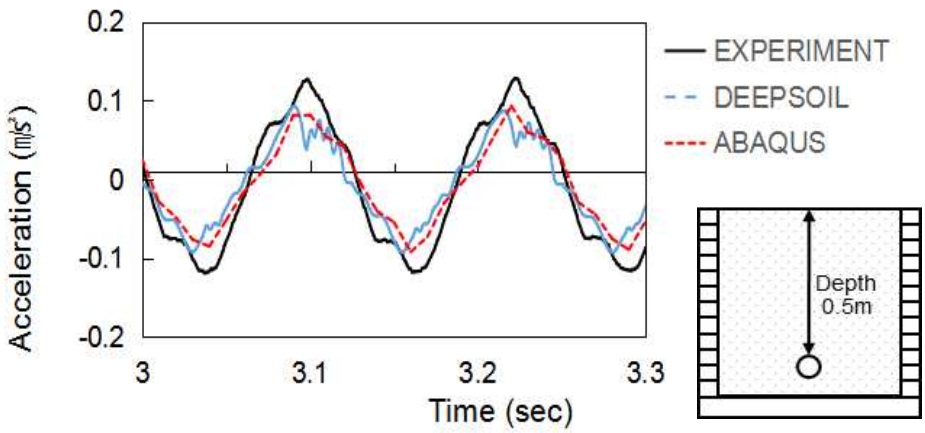

(a) Part of acceleration-time history graph of Sine 8Hz at depth 0.5m

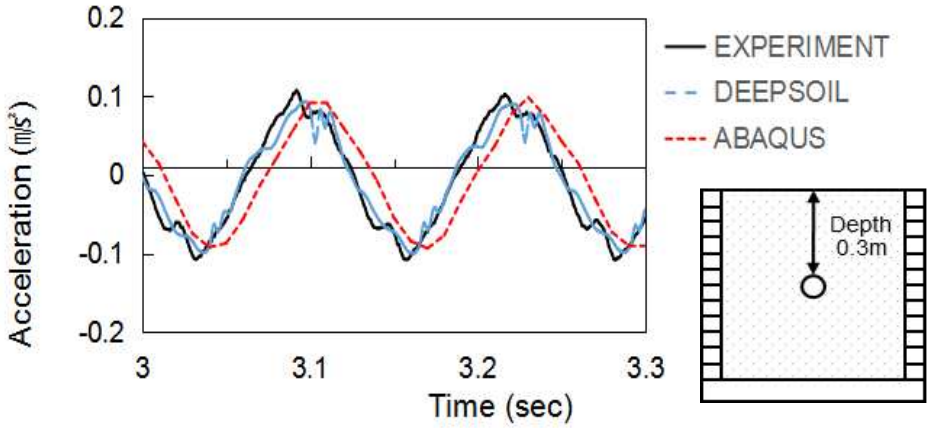

(b) Part of acceleration-time history graph of Sine 8Hz at depth 0.3m

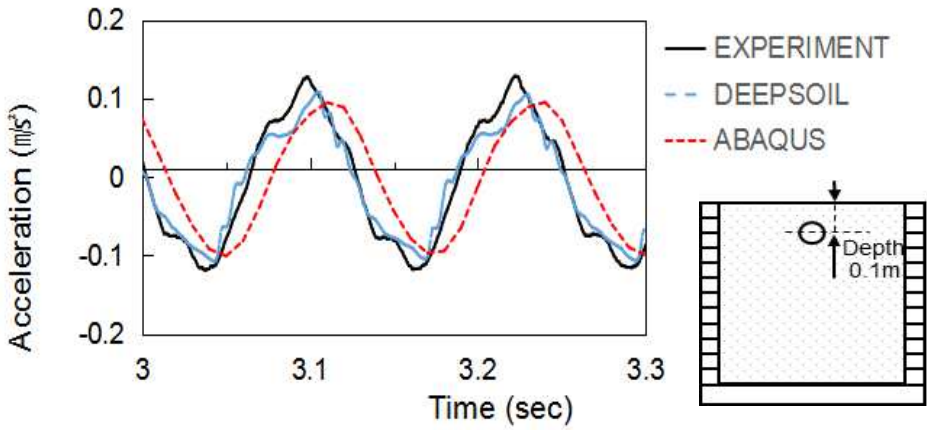

(c) Part of acceleration-time history graph of Sine 8Hz at depth 0.1m

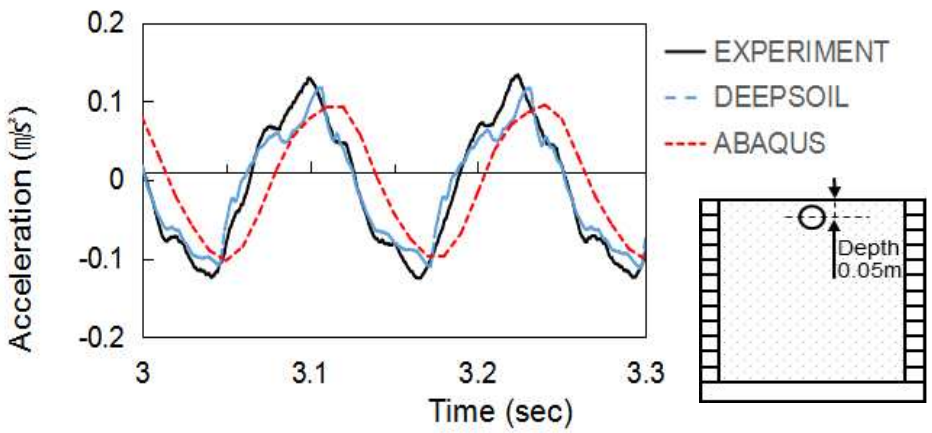

(d) Part of acceleration-time history graph of Sine 8Hz at depth 0.05m

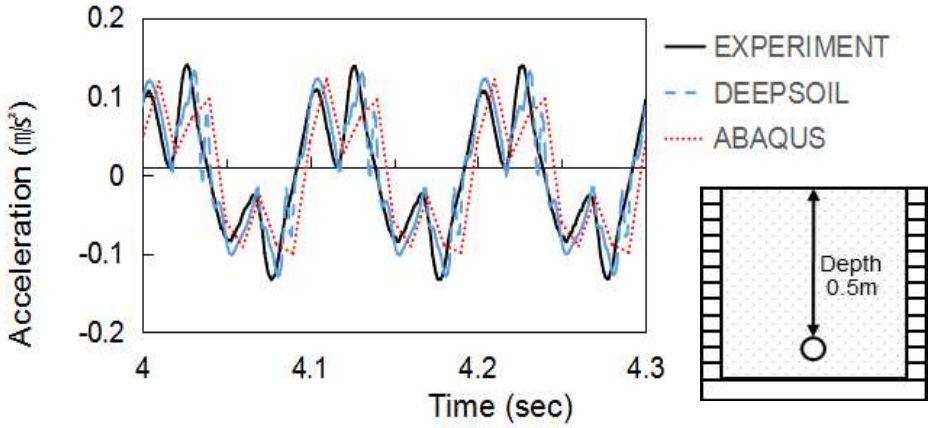

(e) Part of acceleration-time history graph of Sine 10Hz at depth 0.5m

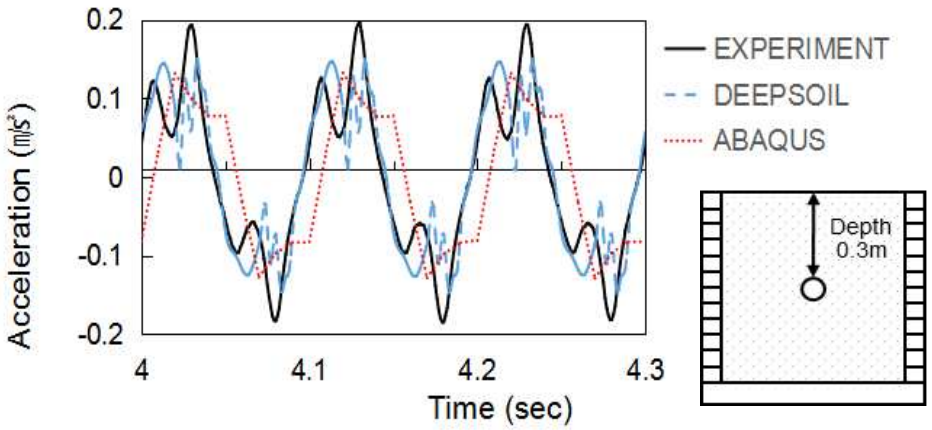

(f) Part of acceleration-time history graph of Sine 10Hz at depth 0.3m

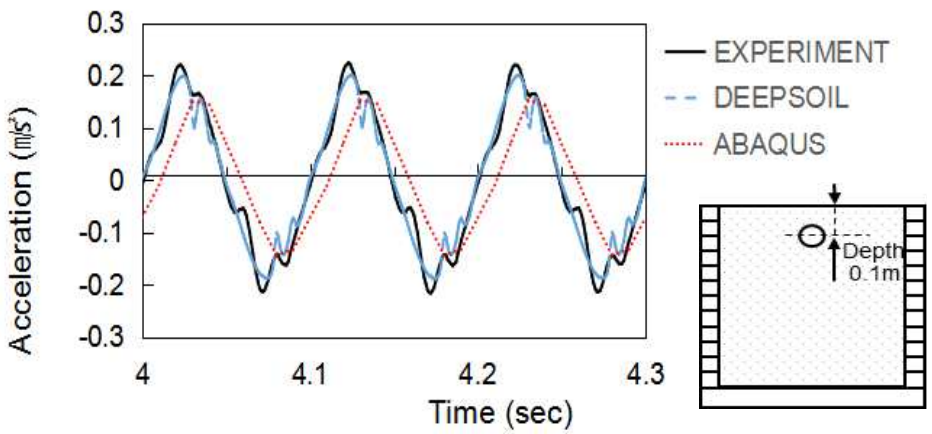

(g) Part of acceleration-time history graph of Sine 10Hz at depth 0.1m

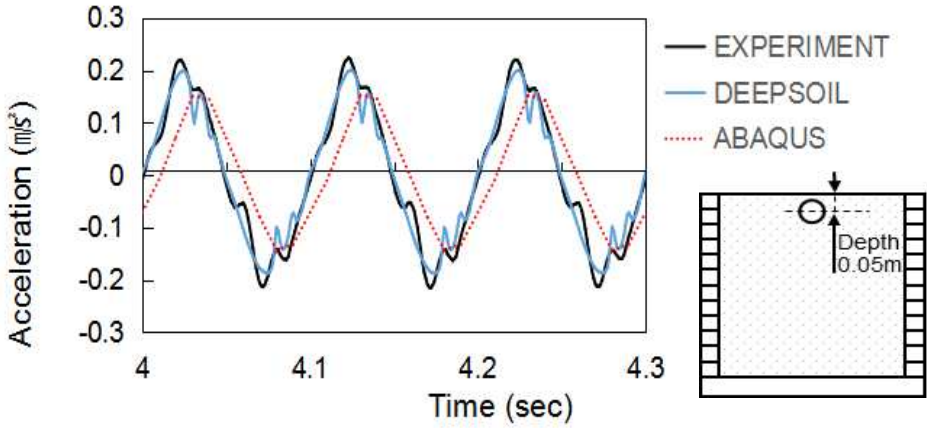

(h) Part of acceleration-time history graph of Sine 10Hz at depth 0.05m

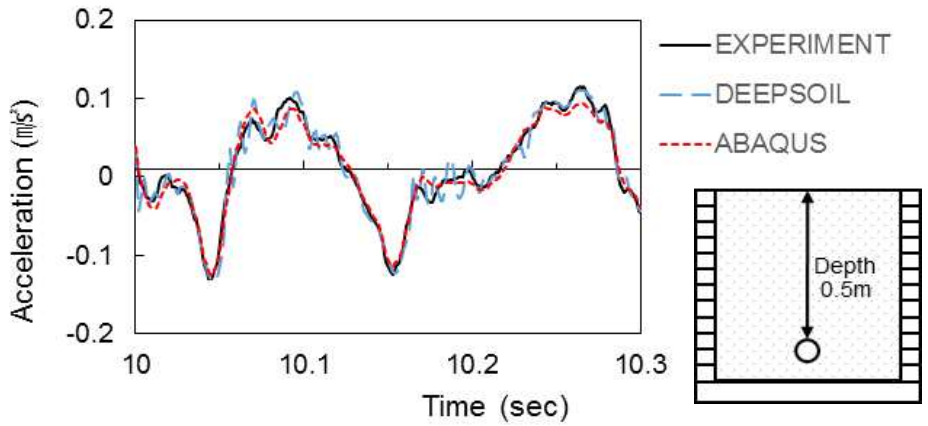

(i) Part of acceleration-time history graph of Artificial wave at depth 0.5m

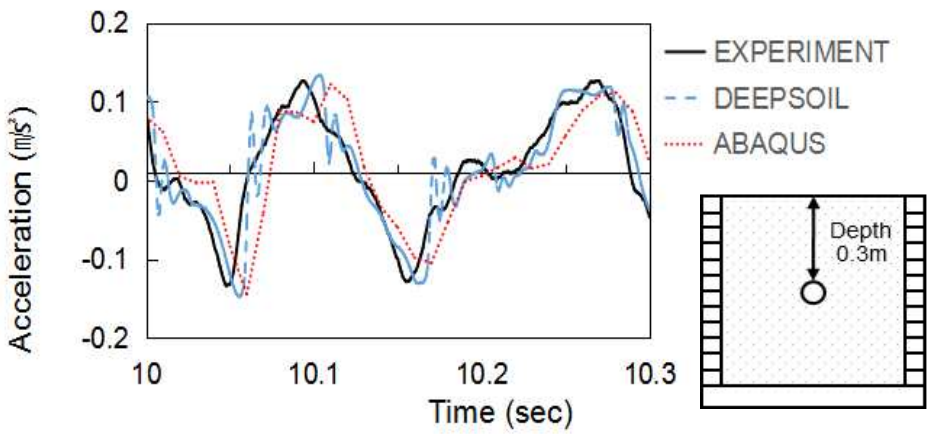

(j) Part of acceleration-time history graph of Artificial wave at depth 0.3m

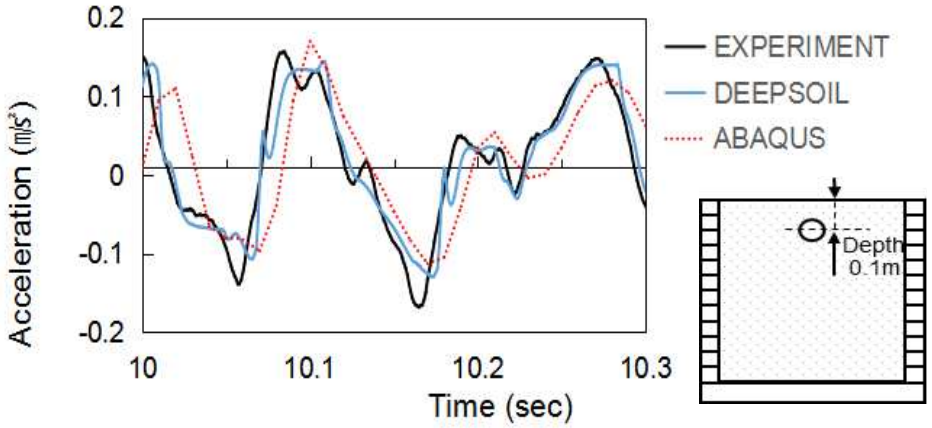

(k) Part of acceleration-time history graph of Artificial wave at depth 0.1m

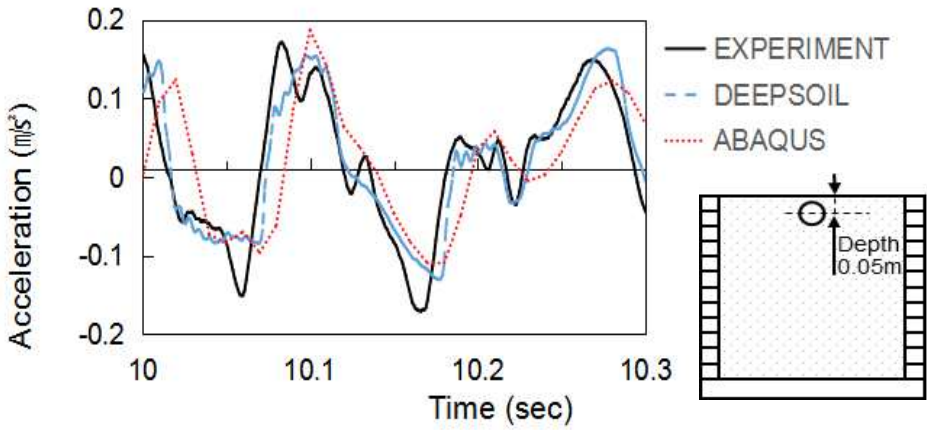

(l) Part of acceleration-time history graph of Artificial wave at depth 0.05m

Figure 5.4 Part of acceleration-time history graph for experiment and analysis.

Under the adjusted elastic modulus, the acceleration-time history of the test and analysis is closer. As shown in Figure 5.4, the experiment is very close to the result of DEEPSOIL. The acceleration-time history of ABAQUS moves slightly as the depth decreases, For the acceleration trend curve, analysis and experimental data are close.

5.2.2 Spectral acceleration

Figure 5.5 shows the Spectral acceleration measured by depth in the 1g shaking

table test and the Spectral acceleration obtained from DEEPSOIL and ABAQUS.

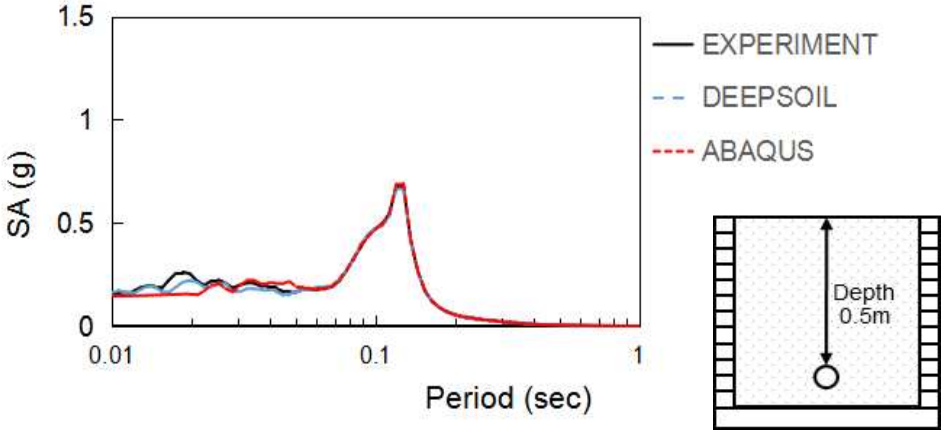

(a) Spectral acceleration by Sine 8Hz at depth 0.5m

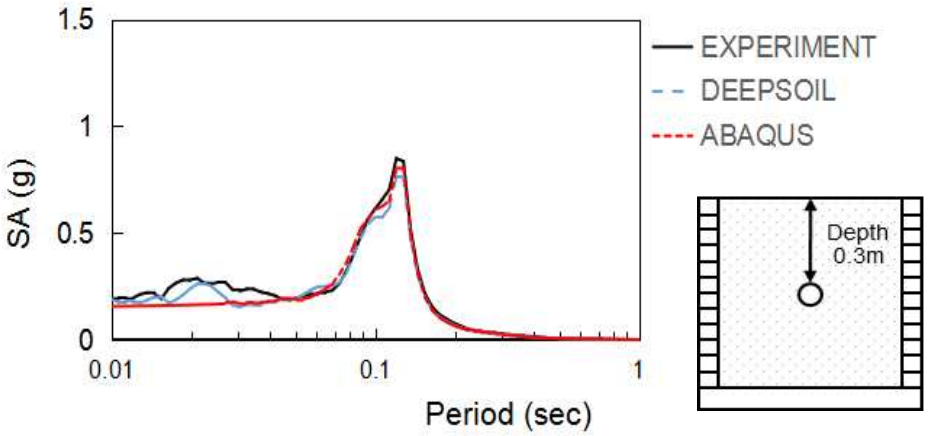

(b) Spectral acceleration by Sine 8Hz at depth 0.3m

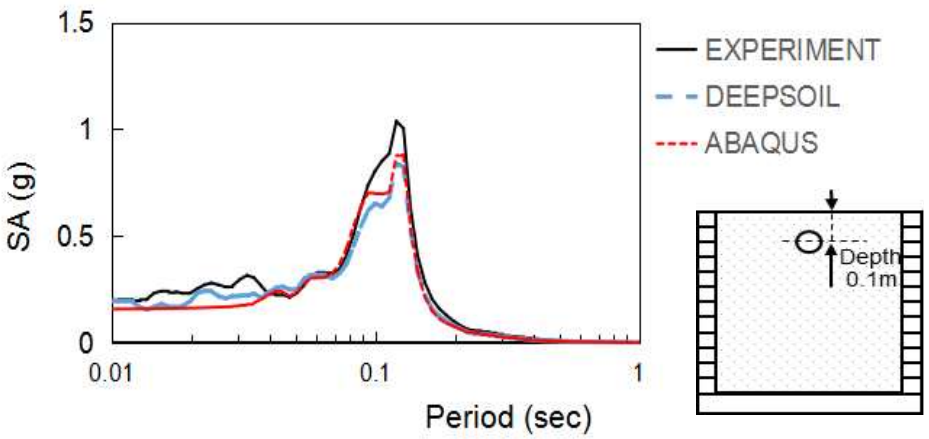

(c) Spectral acceleration by Sine 8Hz at depth 0.1m

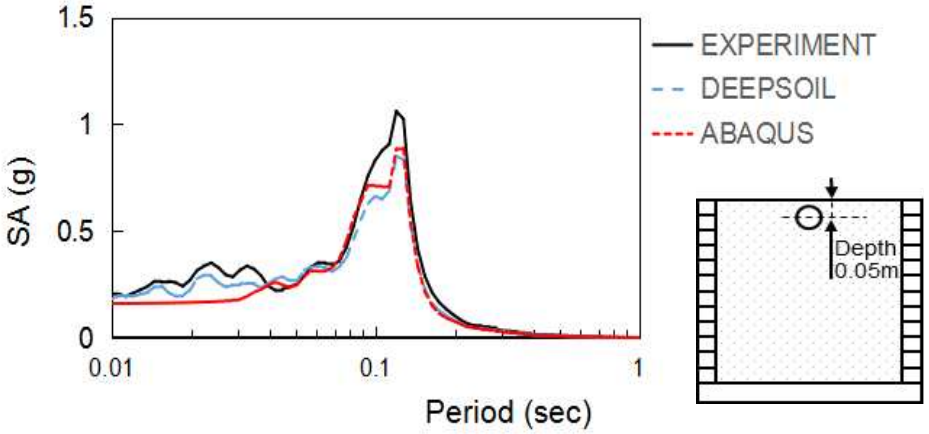

(d) Spectral acceleration of Sine 8Hz at depth 0.05m

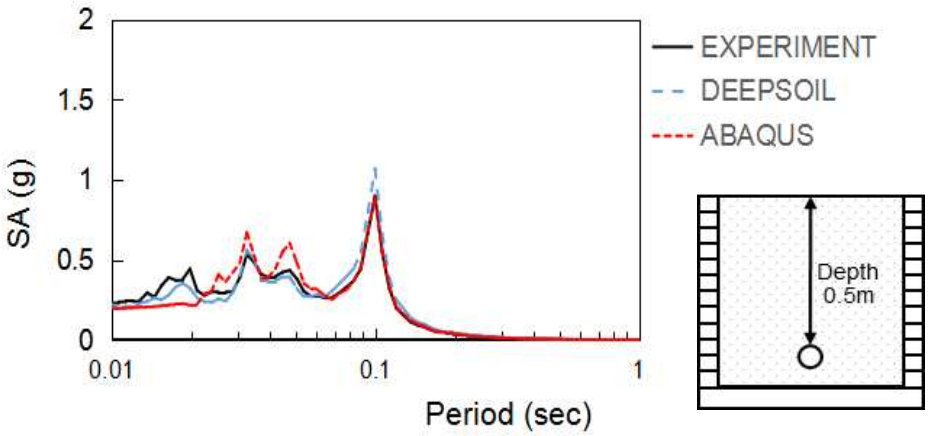

(e) Spectral acceleration by Sine 10Hz at depth 0.5m

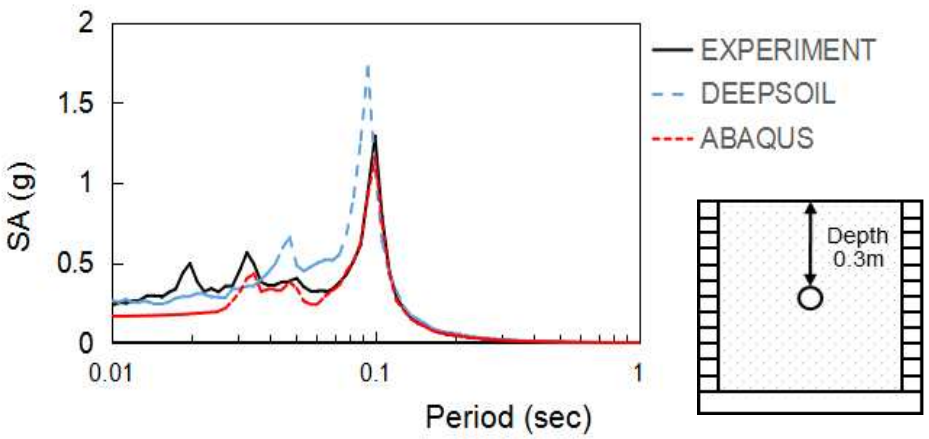

(f) Spectral acceleration by Sine 10Hz at depth 0.3m

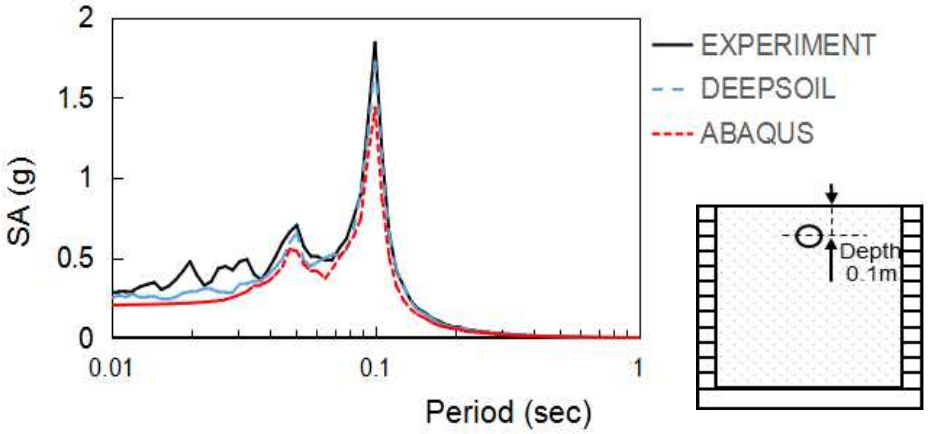

(g) Spectral acceleration by Sine 10Hz at depth 0.1m

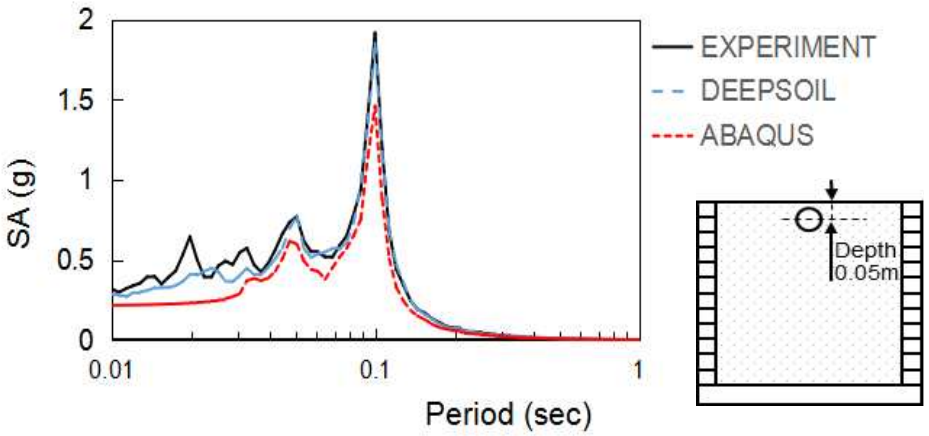

(h) Spectral acceleration by Sine 10Hz at depth 0.05m

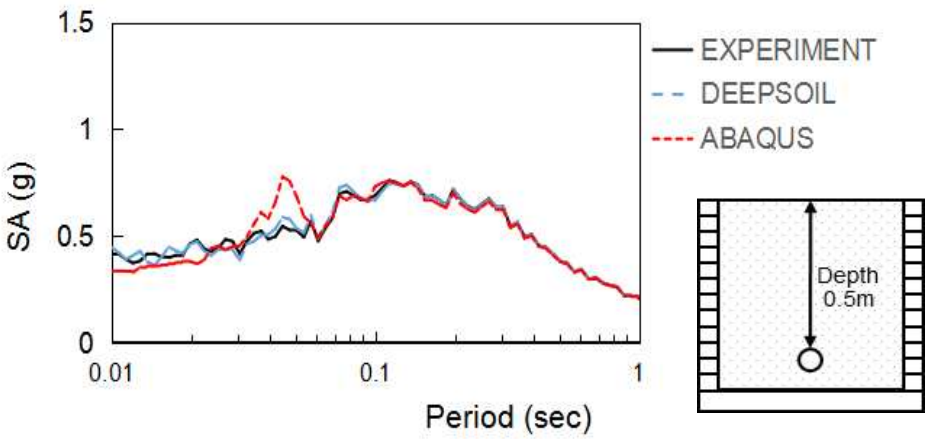

(i) Spectral acceleration by Artificial wave at depth 0.5m

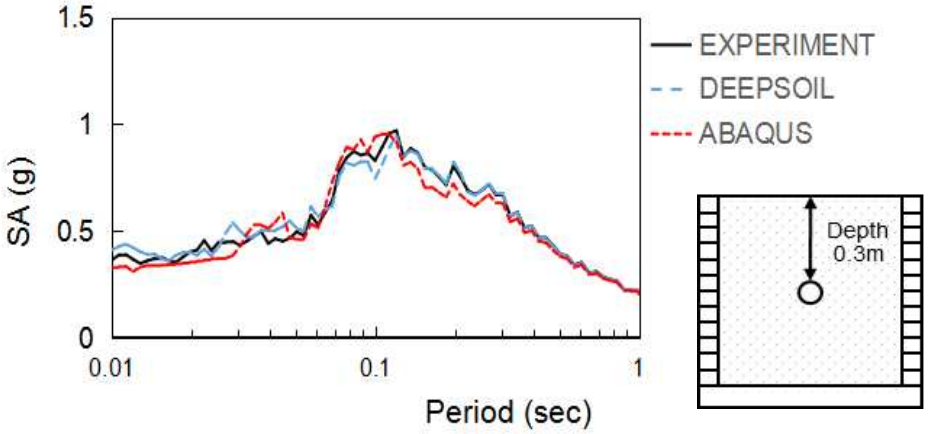

(j) Spectral acceleration by Artificial wave at depth 0.3m

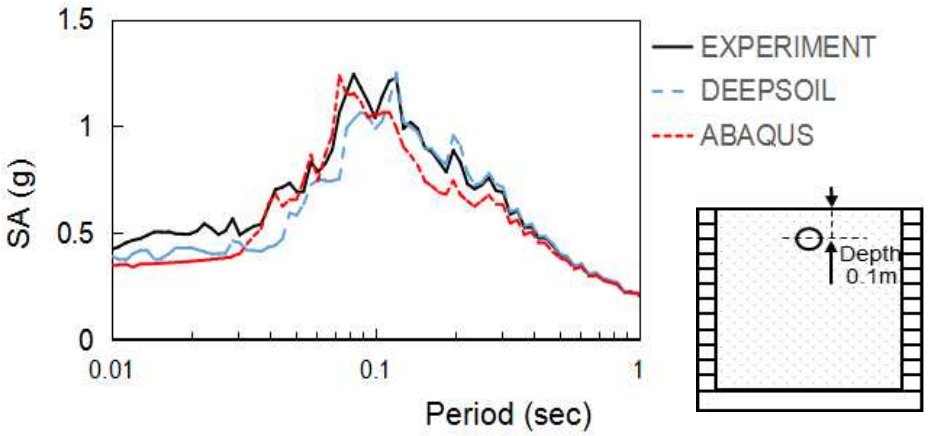

(k) Spectral acceleration by Artificial wave at depth 0.1m

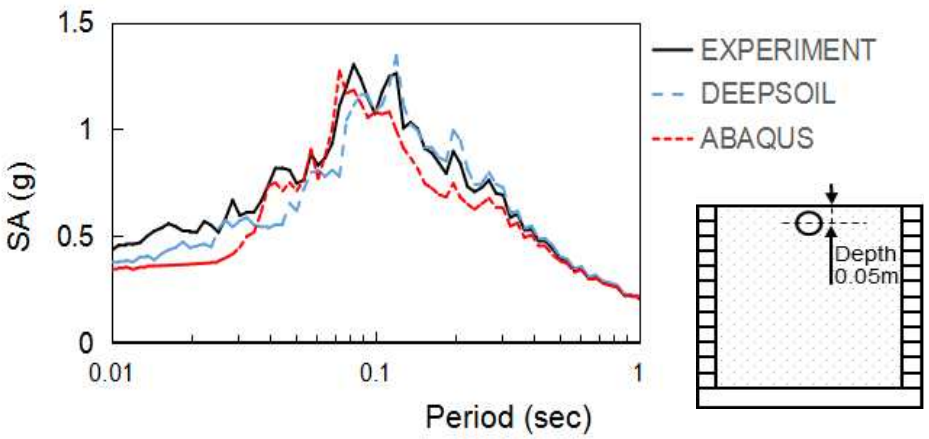

(l) Spectral acceleration by Artificial wave at depth 0.05m

Figure 5.5 Spectral acceleration for experiment and analysis.

Figure 5.5 (a) to (d) are the sine 8Hz spectral acceleration. As the depth decreases, the difference between experiment and analysis gradually increases. The analyzed spectral acceleration amplification is lower than the experimental spectral acceleration amplification. Figure 5.5 (e) to (h) are the sine 10Hz spectral acceleration. The spectral acceleration of ABAQUS is close to the experimental data at very deep depth, but decreases with the depth. The spectral acceleration of DEEPSOIL is closer to the experimental data. Figure 5.5 (i) to (l) are the spectral acceleration of artificial seismic waves. As the depth decreases, the experimental and analysis values are always close, but ABAQUS is closer to the experimental data.

Using the adjusted elastic modulus, acceleration time history and spectral acceleration all show accuracy under the action of each seismic wave. In this case, the analysis result of ABAQUS is closer to the experimental result than that of DEEPSOIL. This case verifies the feasibility of the adjusted elastic modulus and the accuracy of ABAQUS modeling.

5.3 Comparison of slope ground with adjusted elastic modulus

A slope model with a 45-degree inclination angle is used. Accelerometers are set to test the acceleration of the model center and the slope to verify the influence of the slope on the experiment.

Because DEEPSOIL is a 1D semi-infinite space program, the use of DEEPSOIL in this case is not representative, only experimental data and ABAQUS results are used for comparative analysis.

5.3.1 Acceleration-time history

Figure 5.6 shows the Acceleration-time history graph of the experiment and analysis by Sine 8Hz.

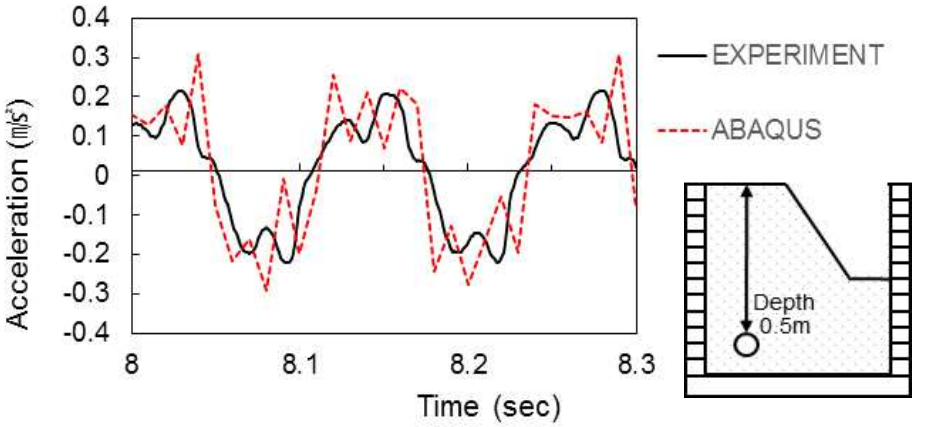

(a) Part of acceleration-time history graph of Sine 8Hz at depth 0.5m

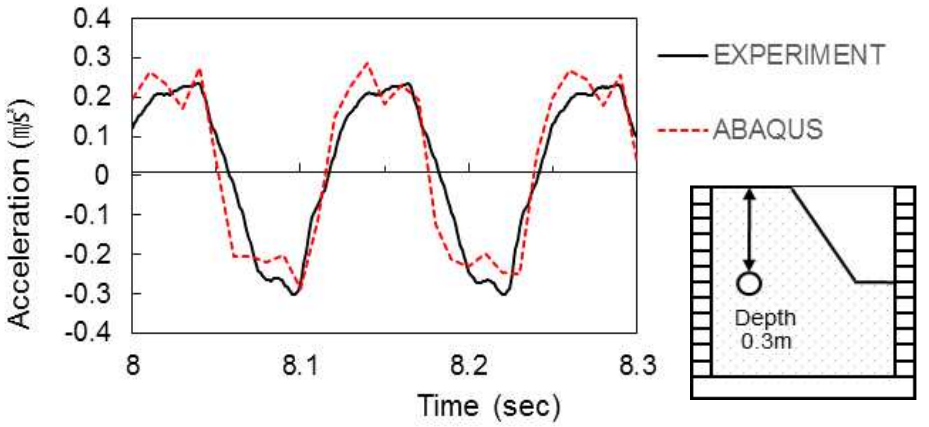

(b) Part of acceleration-time history graph of Sine 8Hz at depth 0.3m

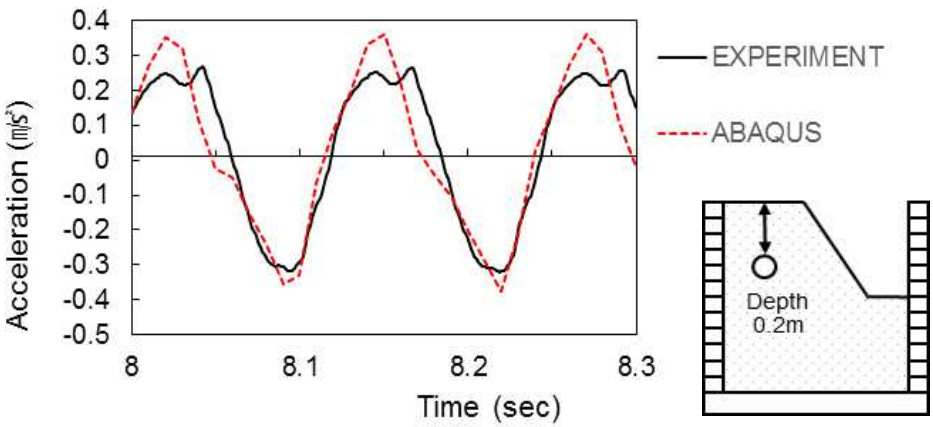

(c) Part of acceleration-time history graph of Sine 8Hz at depth 0.2m

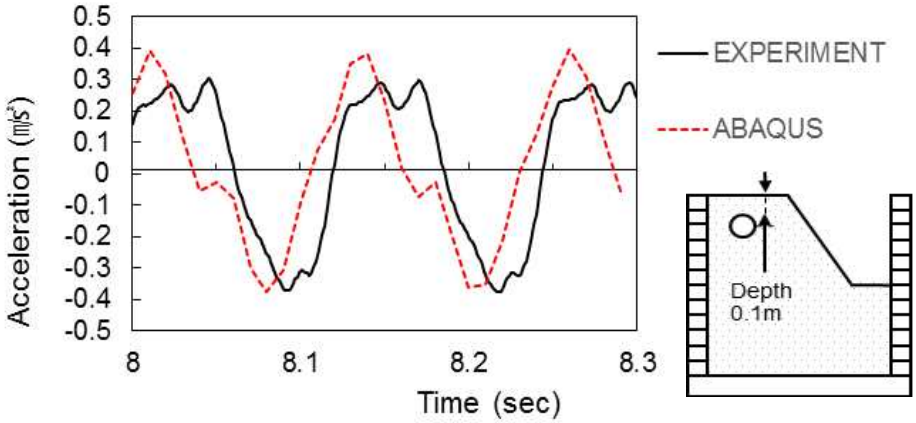

(d) Part of acceleration-time history graph of Sine 8Hz at depth 0.1m

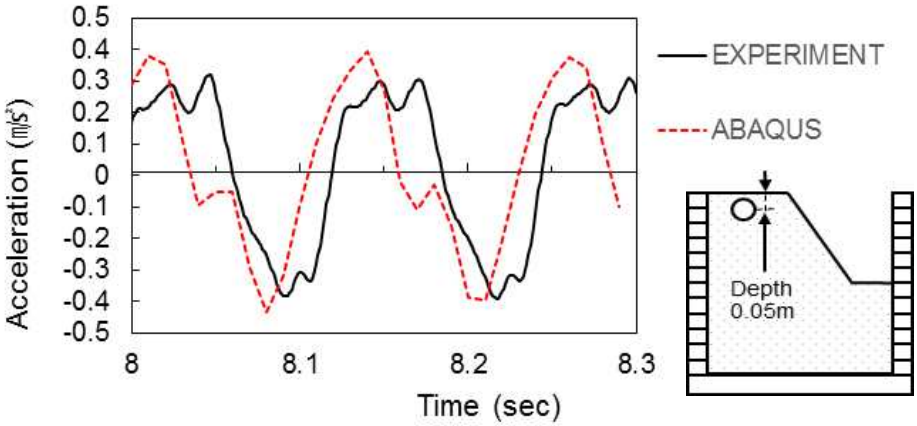

(e) Part of acceleration-time history graph of Sine 8Hz at depth 0.05m

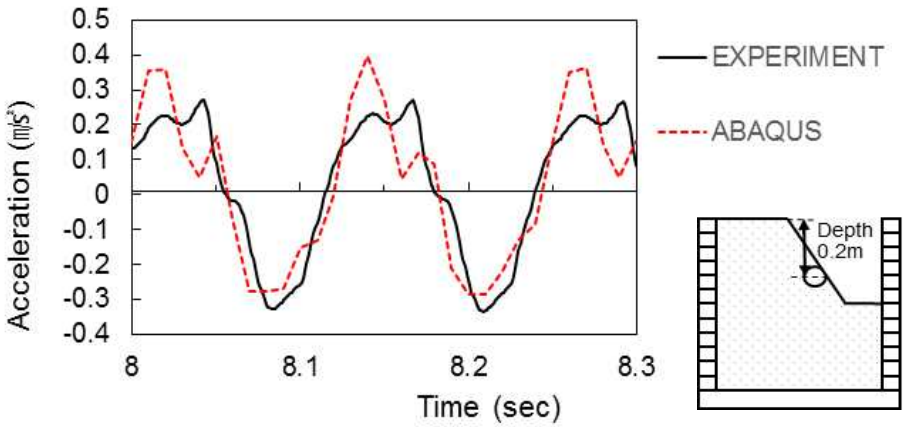

(f) Part of acceleration-time history graph of Sine 8Hz at depth 0.2m in slope

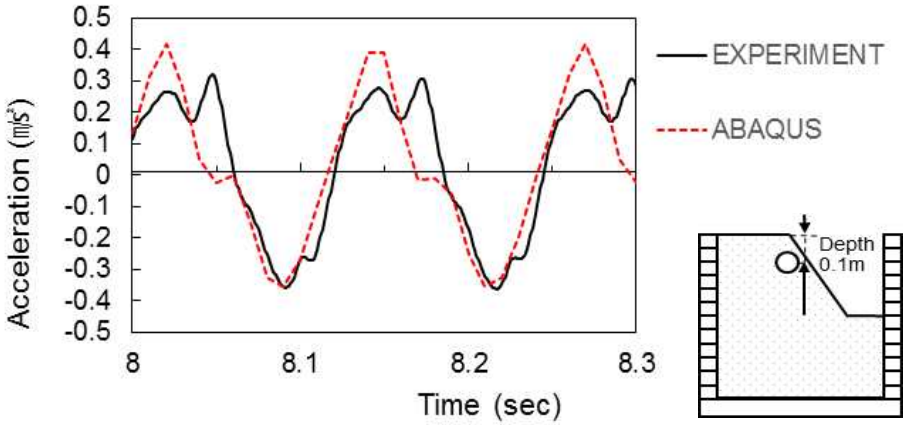

(g) Part of acceleration-time history graph of Sine 8Hz at depth 0.1m in slope

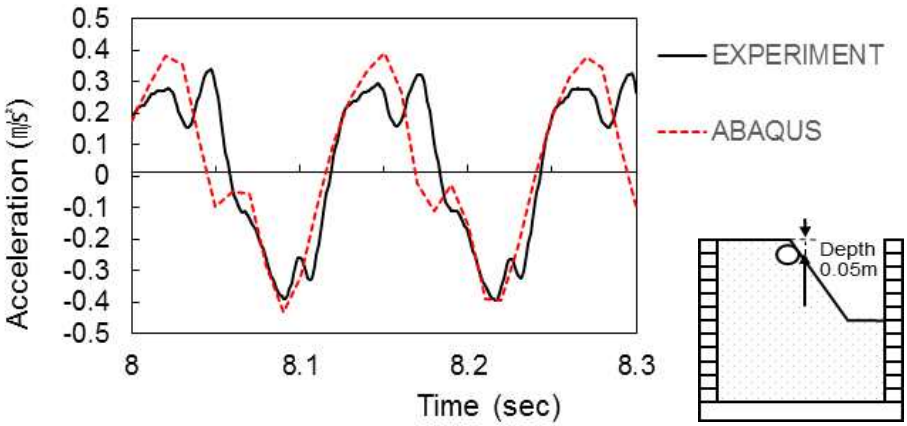

(h) Part of acceleration-time history graph of Sine 8Hz at depth 0.05m in slope

Figure 5.6 Part of acceleration-time history graph for experiment and analysis by Sine 8Hz.

Figure 5.6 (a) to (e) are the acceleration-time history at the center of the slope model under Sine 8HZ. As the depth decreases, the acceleration peaks between the experiment and ABAQUS gradually increase, and the difference gradually increases, but the trend is still very close. Figure 5.6 (f) to (h) are the slope acceleration time history of the slope model under sine 8Hz. As the depth decreases, the acceleration peaks of the test and ABAQUS gradually increase, and the acceleration time history is very close.

Figure 5.7 shows the Acceleration-time history graph of the experiment and analysis by Sine 10Hz.

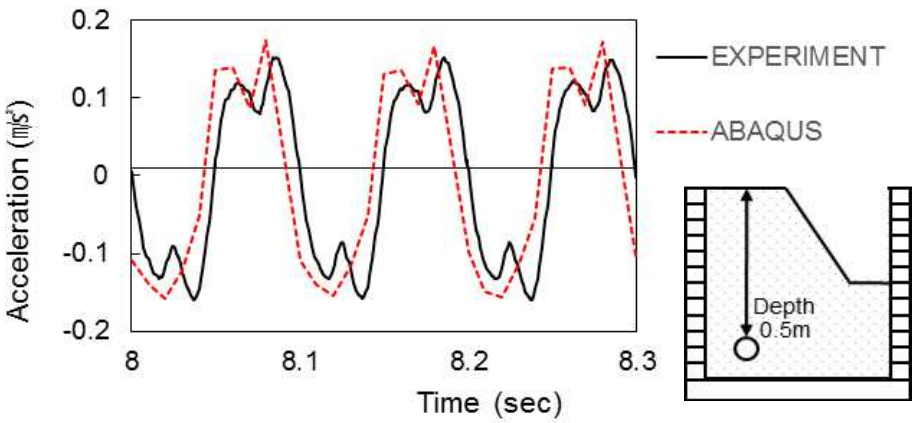

(a) Part of acceleration-time history graph of Sine 10Hz at depth 0.5m

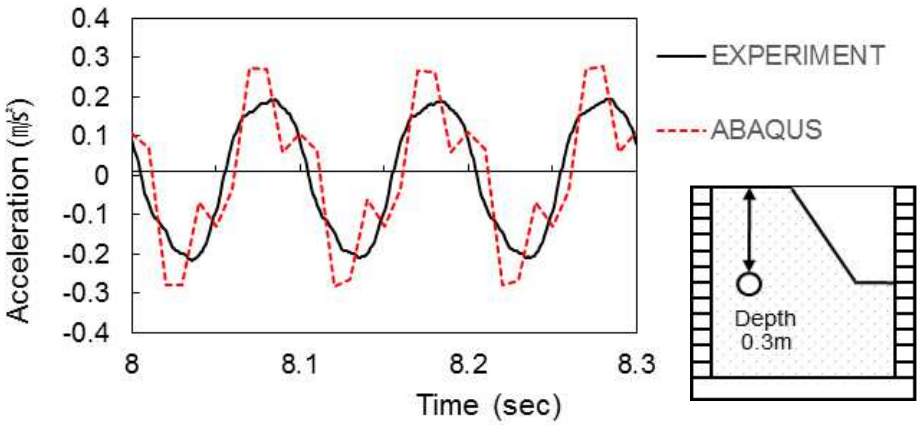

(b) Part of acceleration-time history graph of Sine 10Hz at depth 0.3m

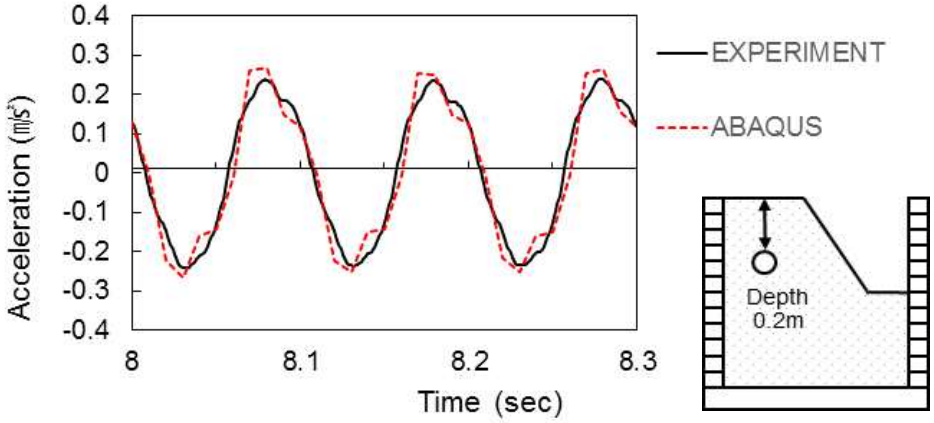

(c) Part of acceleration-time history graph of Sine 10Hz at depth 0.2m

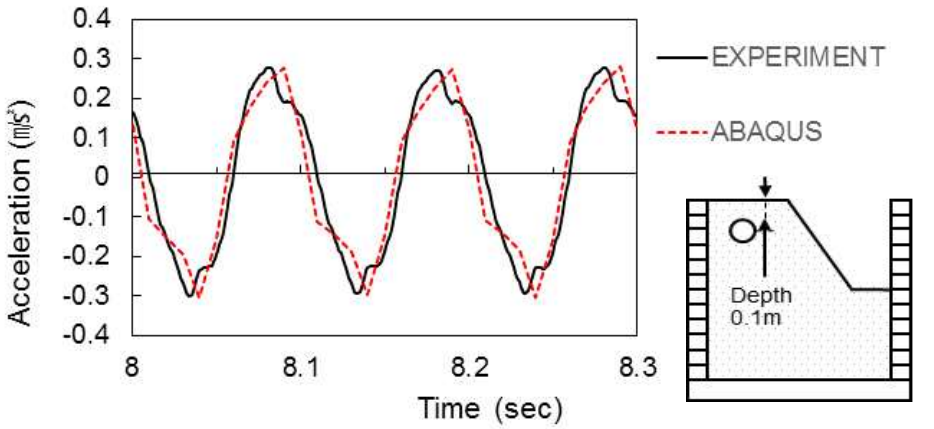

(d) Part of acceleration-time history graph of Sine 10Hz at depth 0.1m

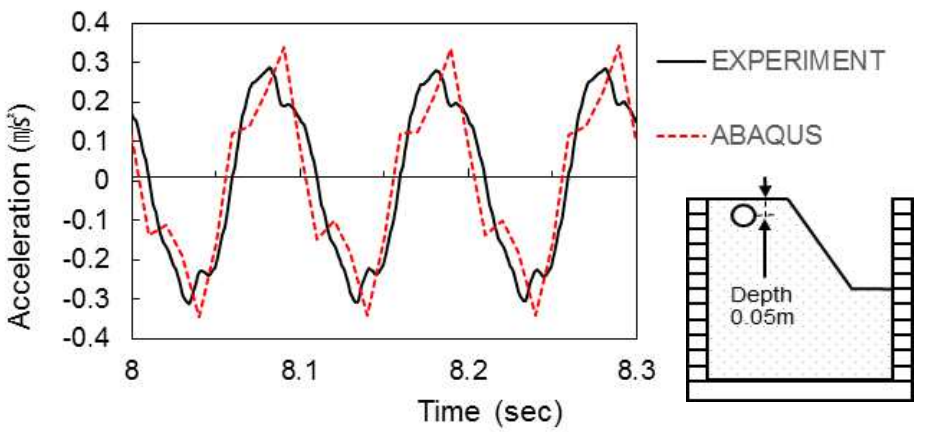

(e) Part of acceleration-time history graph of Sine 10Hz at depth 0.05m

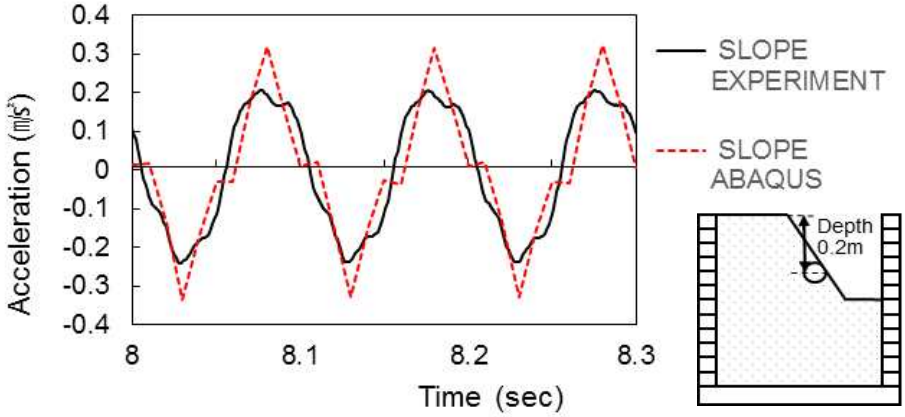

(f) Part of acceleration-time history graph of Sine 10Hz at depth 0.2m in slope

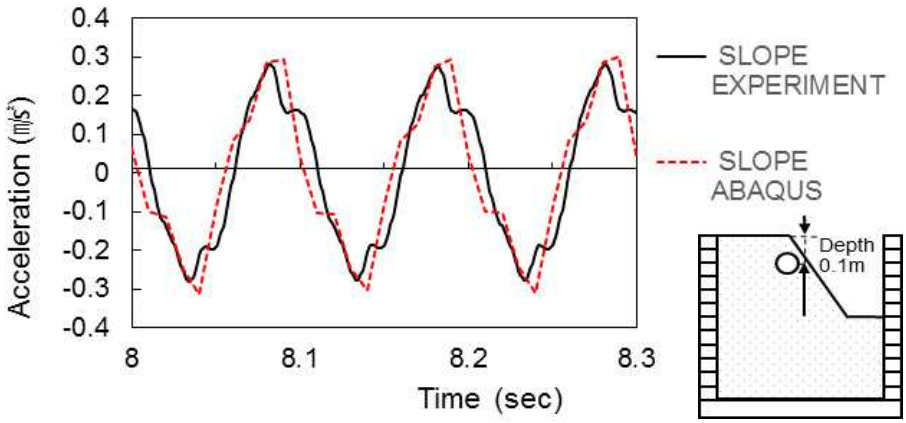

(g) Part of acceleration-time history graph of Sine 10Hz at depth 0.1m in slope

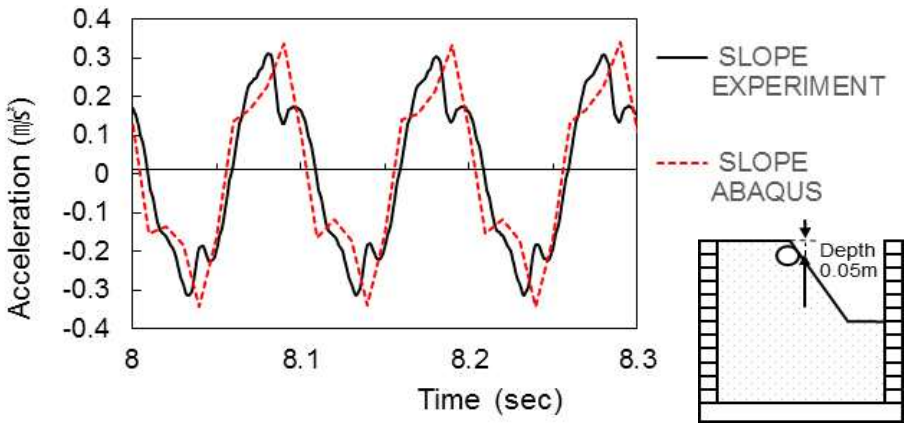

(h) Part of acceleration-time history graph of Sine 10Hz at depth 0.05m in slope

Figure 5.7 Part of acceleration-time history graph for experiment and analysis by Sine 10Hz.

Figure 5.7 (a) to (e) show the acceleration-time history at the center of the slope model under sine 10Hz. As the depth decreases, ABAQUS and the experimental acceleration continue to increase and are very close. Figure 5.7(f) to (h) are the acceleration-time history analysis of the slope model under sine 10Hz. As the depth increases, ABAQUS and the experimental acceleration continue to increase, and the results are getting closer and closer.

Figure 5.8 shows the Acceleration-time history graph of the experiment and analysis by Artificial seismic wave.

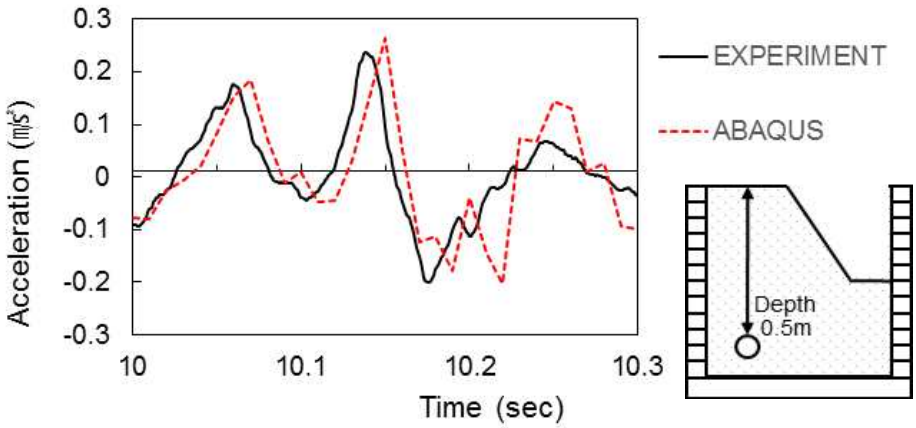

(a) Part of acceleration-time history graph of Artificial wave at depth 0.5m

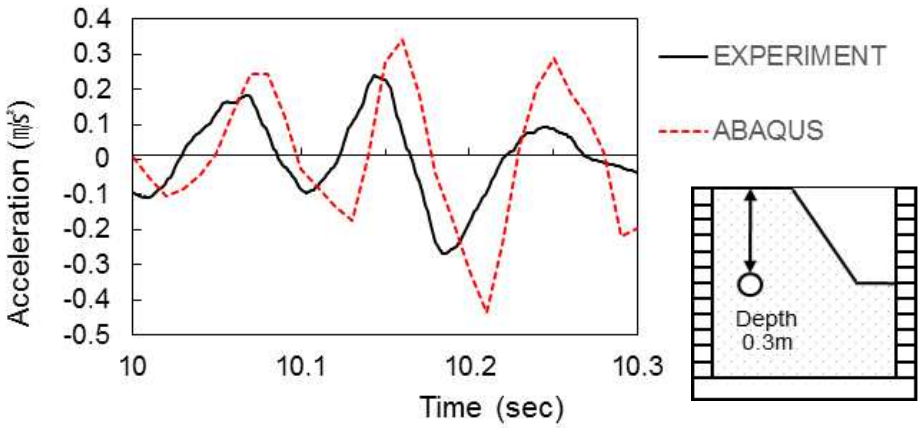

(b) Part of acceleration-time history graph of Artificial wave at depth 0.3m

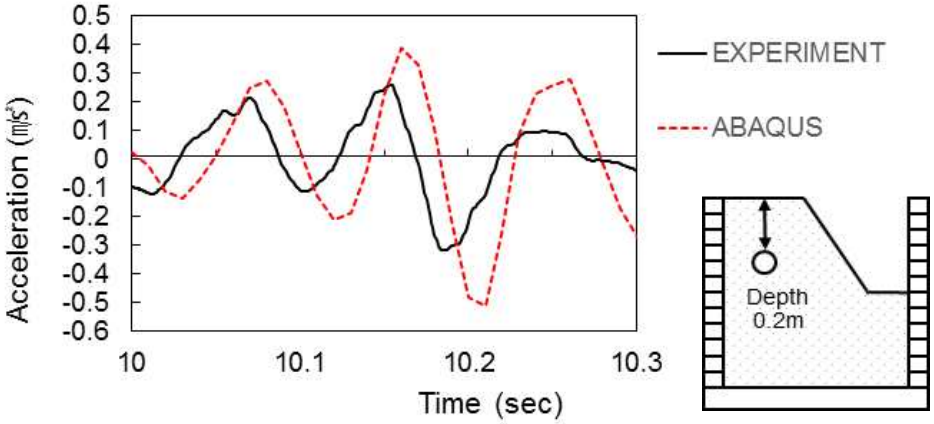

(c) Part of acceleration-time history graph of Artificial wave at depth 0.2m

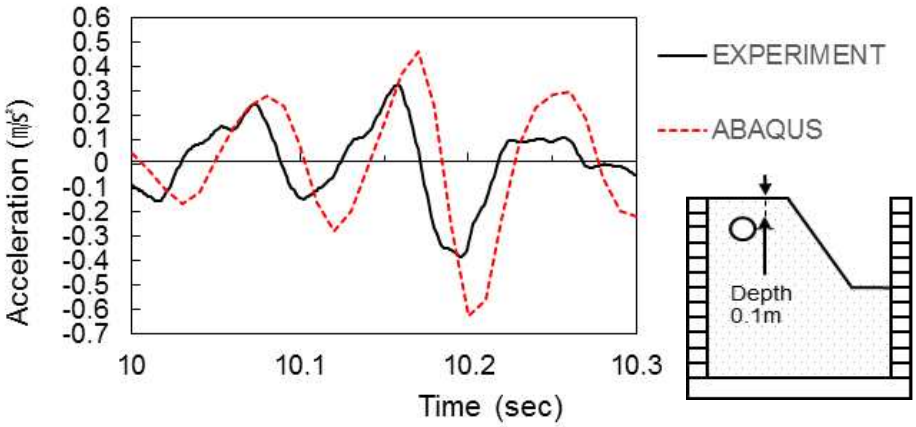

(d) Part of acceleration-time history graph of Artificial wave at depth 0.1m

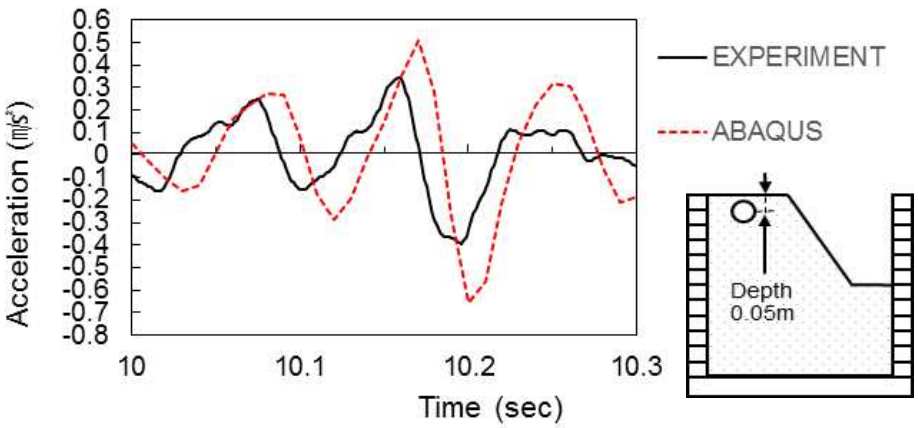

(e) Part of acceleration-time history graph of Artificial wave at depth 0.05m

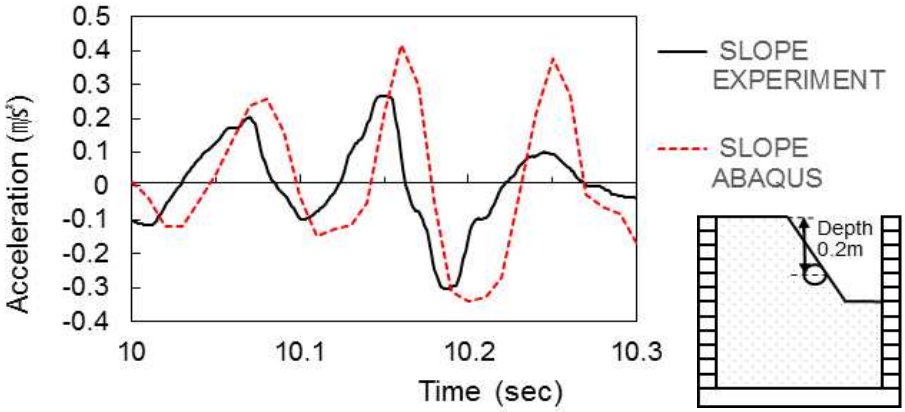

(f) Part of acceleration-time history graph of Artificial wave at depth 0.2m in slope

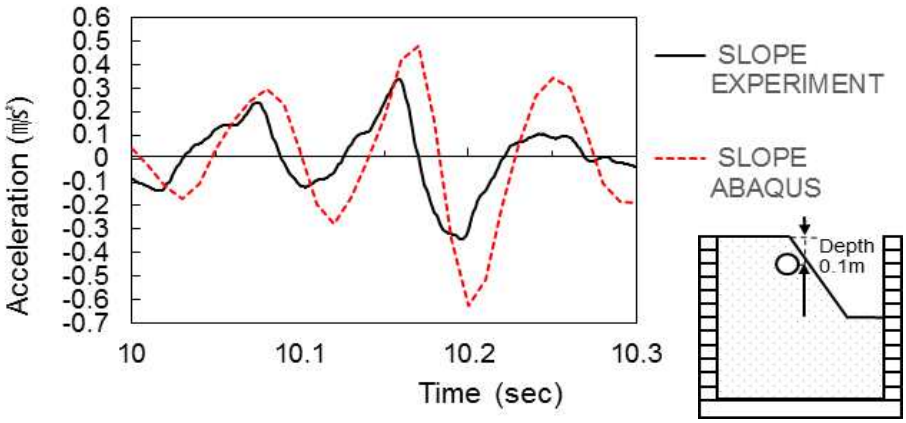

(g) Part of acceleration-time history graph of Artificial wave at depth 0.1m in slope

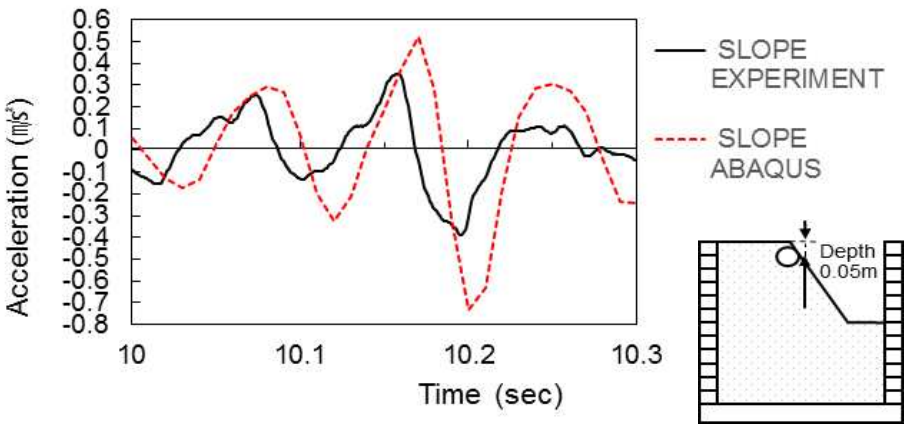

(h) Part of acceleration-time history graph of Artificial wave at depth 0.05m in slope

Figure 5.8 Part of acceleration-time history graph for experiment and analysis by Artificial wave.

Figure 5.8 (a) to (e) are the acceleration-time history of the slope model center under artificial seismic wave. In general, the experimental and ABAQUS analysis results are not quiet same, and the ABAQUS acceleration-time history curve is larger than the experimental curve. Figure 5.8 (f) to (h) are the acceleration history analysis of the slope model under artificial seismic wave. As the depth increases, the results of the test and analysis gradually increase, but the difference does not change much. This may be caused by parameter changes in the experiment or partial destruction of raw materials.

5.3.2 Spectral acceleration

Figure 5.9 shows the Spectral acceleration measured by depth in the 1g shaking table test and the Spectral acceleration obtained from ABAQUS.

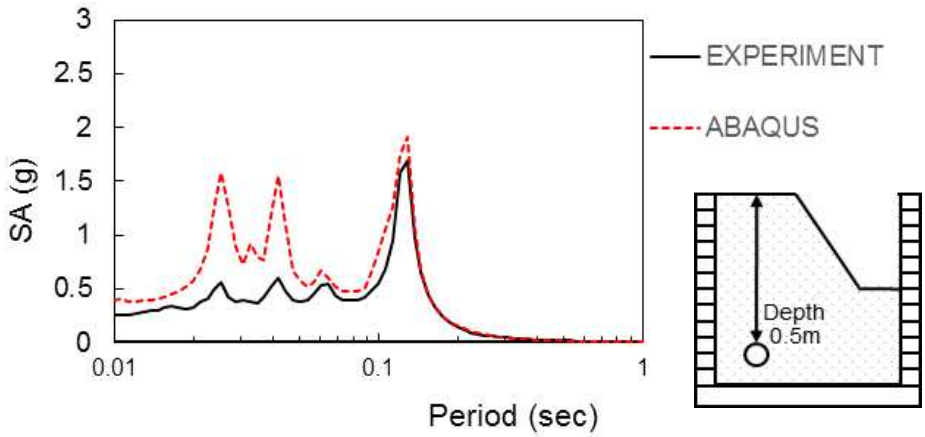

(a) Spectral acceleration by Sine 8Hz at depth 0.5m

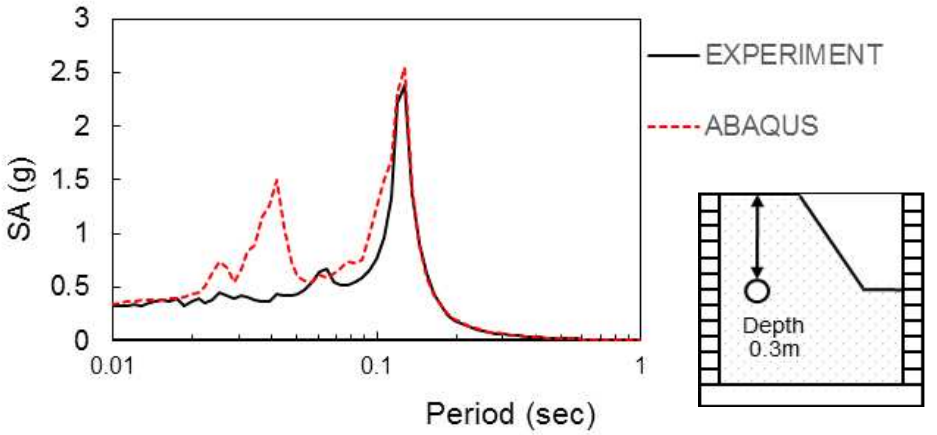

(b) Spectral acceleration by Sine 8Hz at depth 0.3m

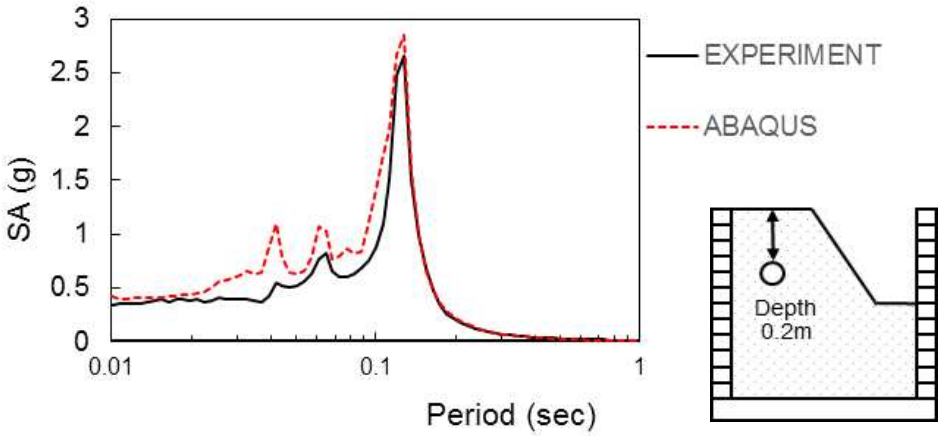

(c) Spectral acceleration by Sine 8Hz at depth 0.2m

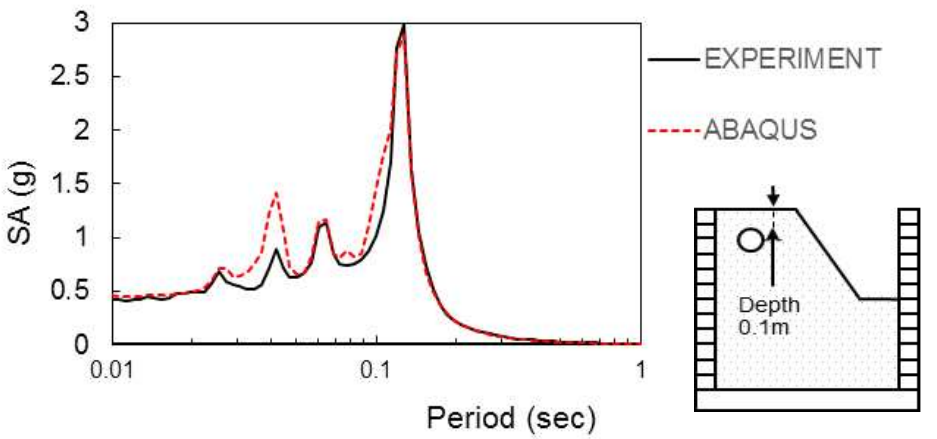

(d) Spectral acceleration by Sine 8Hz at depth 0.1m

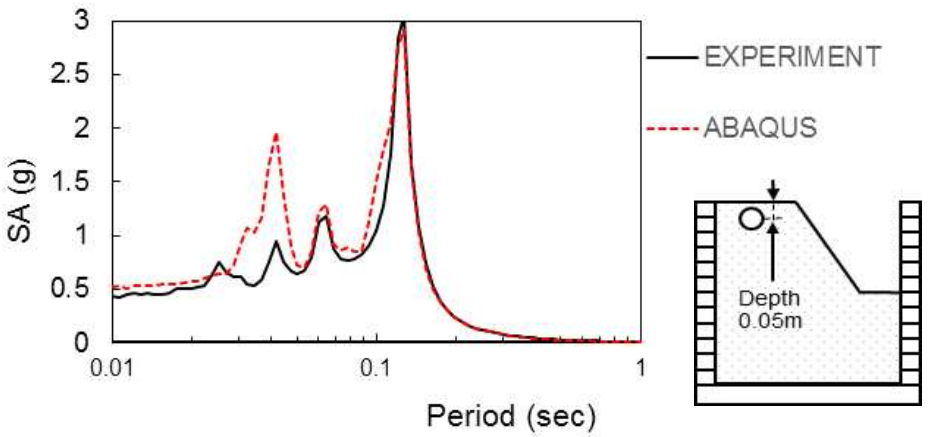

(e) Spectral acceleration of Sine 8Hz at depth 0.05m

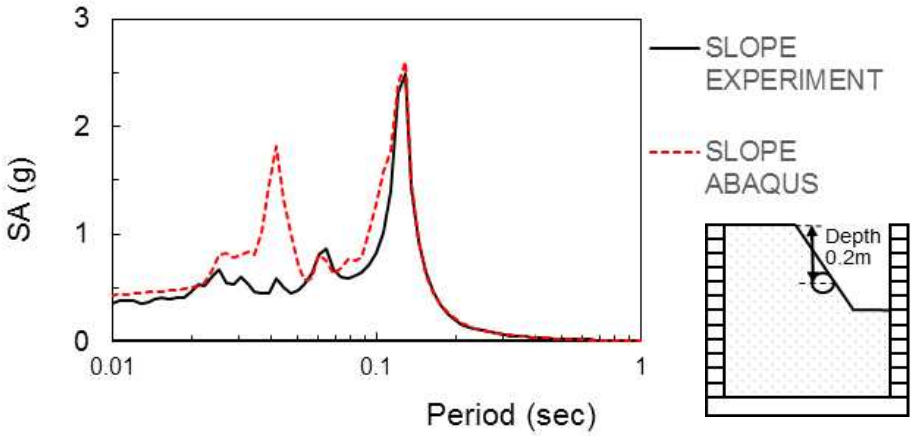

(f) Spectral acceleration by Sine 8Hz at depth 0.2m in slope

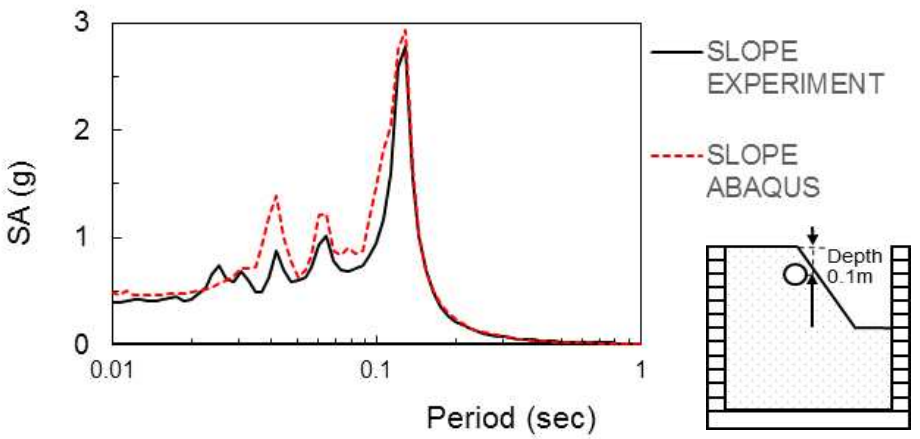

(g) Spectral acceleration by Sine 8Hz at depth 0.1m in slope

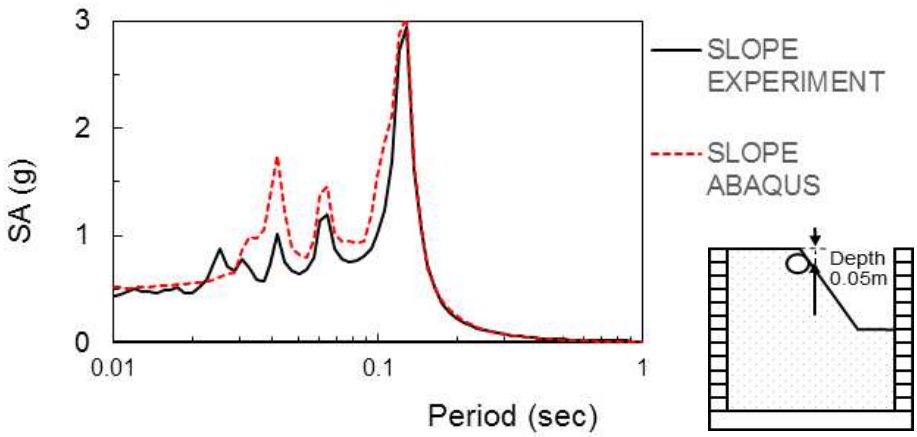

(h) Spectral acceleration by Sine 8Hz at depth 0.05m in slope

Figure 5.9 Spectral acceleration for experiment and analysis by Sine 8Hz.

Figure 5.9(a) to (e) are the spectral acceleration of the slope model under sine 8Hz. As the depth decreases, the trend and peak value of the spectrum acceleration between the experiment and ABAQUS are always close. For the left side of the peak, the numerical value of ABAQUS is greater than the experimental value. Figure 5.10 (f) to (h) are the slope model spectral acceleration under sine 8Hz, the general trend and peak value of the experiment and ABAQUS are very close. As the depth decreases, the spectral acceleration value on the left gradually becomes consistent.

Figure 5.10 shows the Spectral acceleration measured by depth in the 1g shaking table test and the Spectral acceleration obtained from ABAQUS.

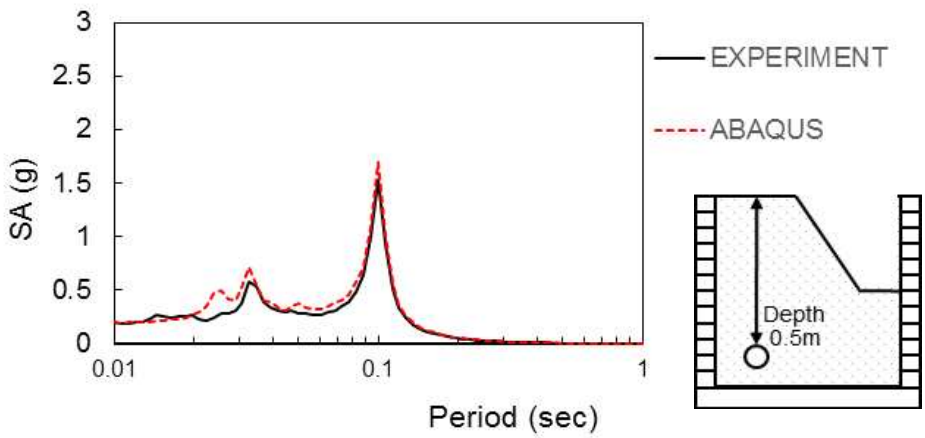

(a) Spectral acceleration by Sine 10Hz at depth 0.5m

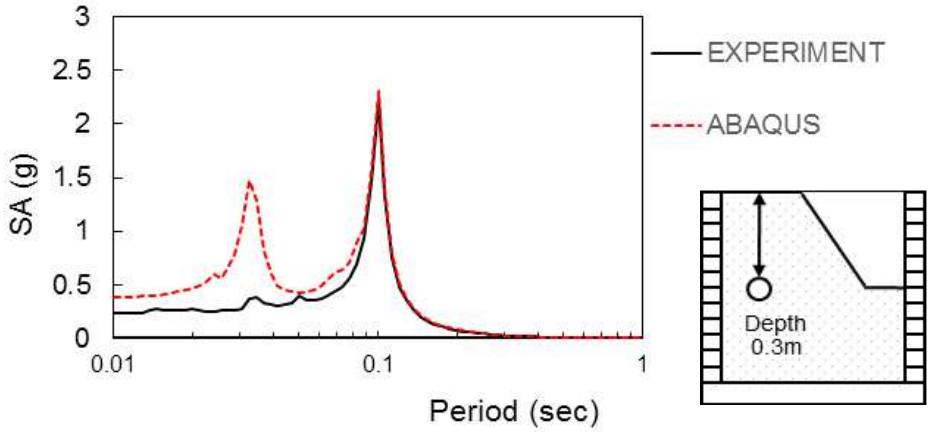

(b) Spectral acceleration by Sine 10Hz at depth 0.3m

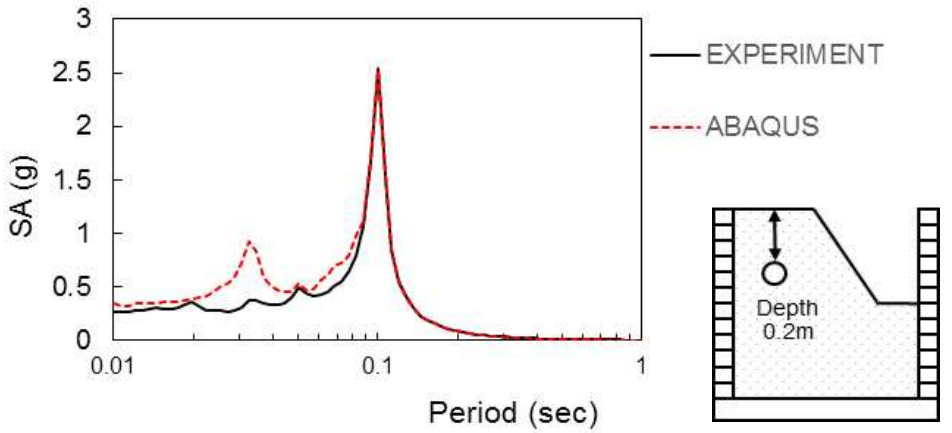

(c) Spectral acceleration by Sine 10Hz at depth 0.2m

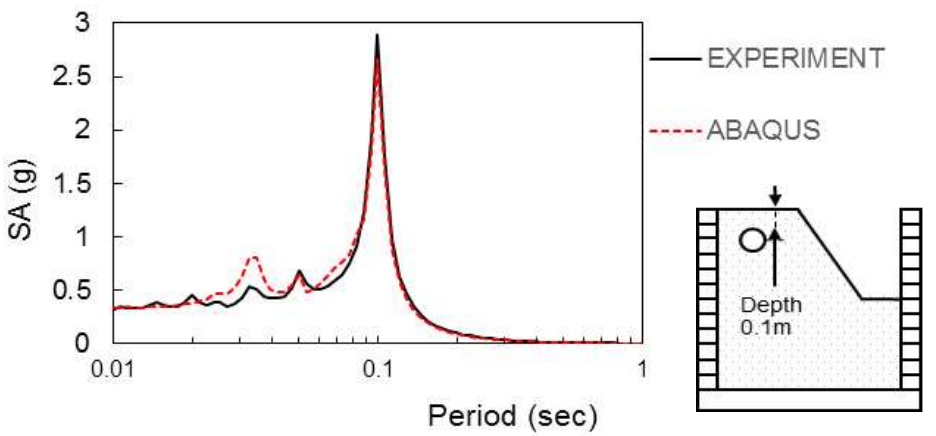

(d) Spectral acceleration by Sine 10Hz at depth 0.1m

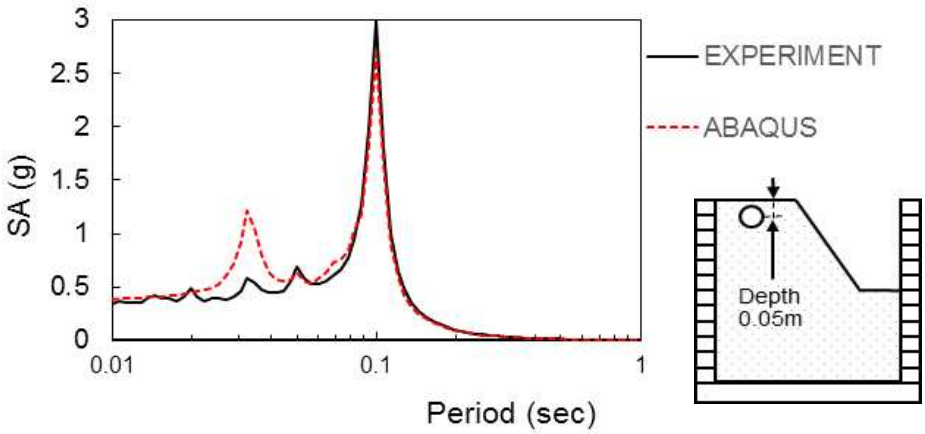

(e) Spectral acceleration of Sine 10Hz at depth 0.05m

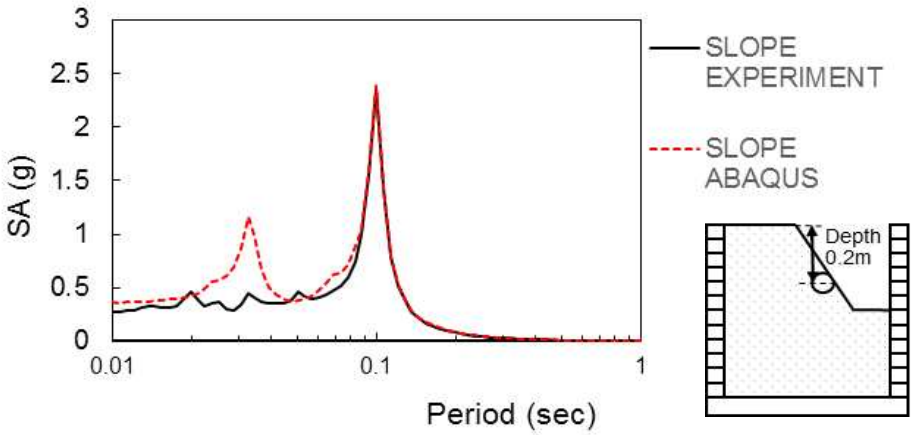

(f) Spectral acceleration by Sine 10Hz at depth 0.2m in slope

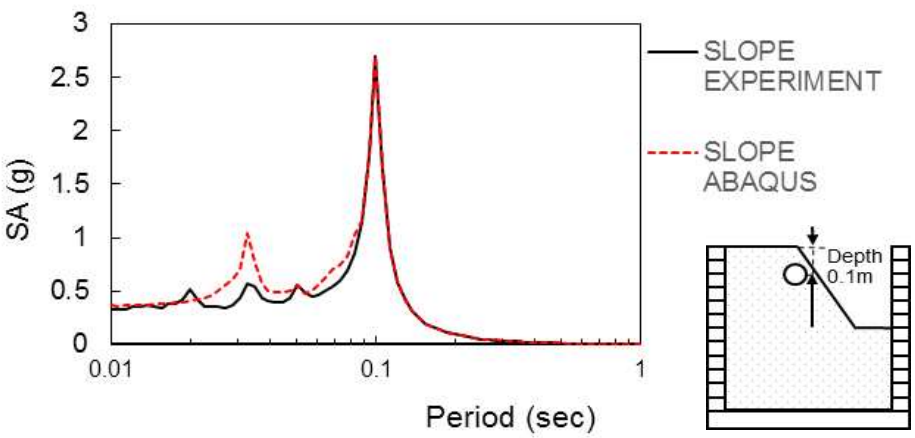

(g) Spectral acceleration by Sine 10Hz at depth 0.1m in slope

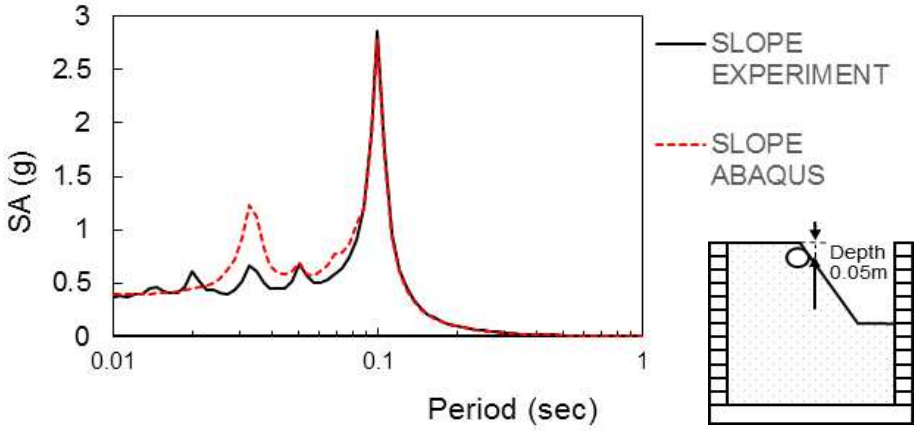

(h) Spectral acceleration by Sine 10Hz at depth 0.05m in slope

Figure 5.10 Spectral acceleration for experiment and analysis by Sine 10Hz.

Figure 5.10 (a) to (e) are the spectral acceleration of the slope model under sine 10Hz. As the depth decreases, the experimental and ABAQUS spectrum acceleration gradually increase. The peak value of the spectral acceleration is always close, and the two tend to coincide. Figure 5.10 (f) to (h) are the spectral acceleration of the slope model under sine 10Hz. The general trend and peak value of the test and ABAQUS are very close. As the depth decreases, the spectral acceleration values on the left gradually become consistent.

Figure 5.11 shows the Spectral acceleration measured by depth in the 1g shaking table test and the Spectral acceleration obtained from ABAQUS.

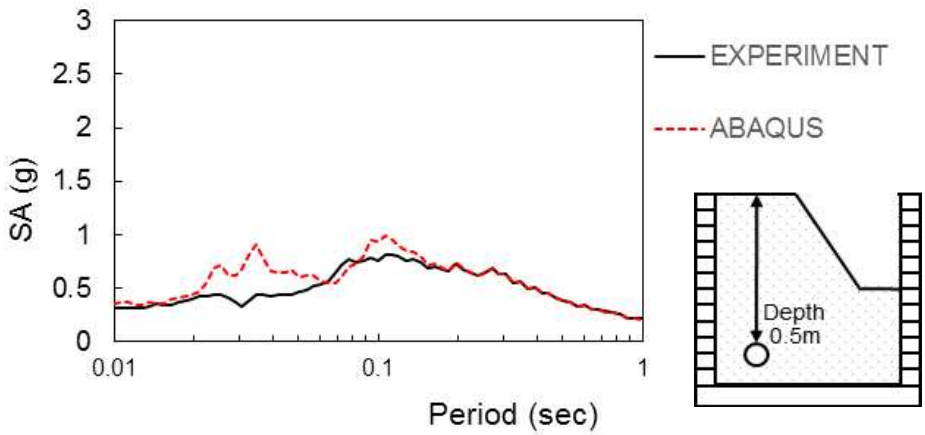

(a) Spectral acceleration by Artificial wave at depth 0.5m

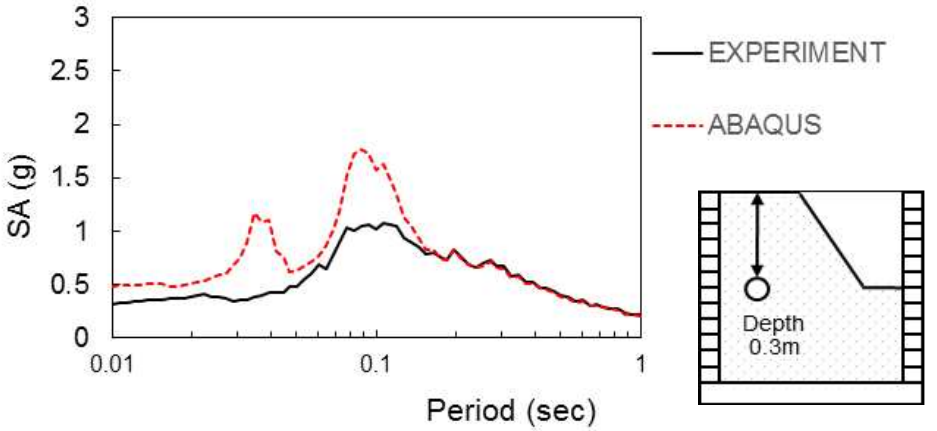

(b) Spectral acceleration by Artificial wave at depth 0.3m

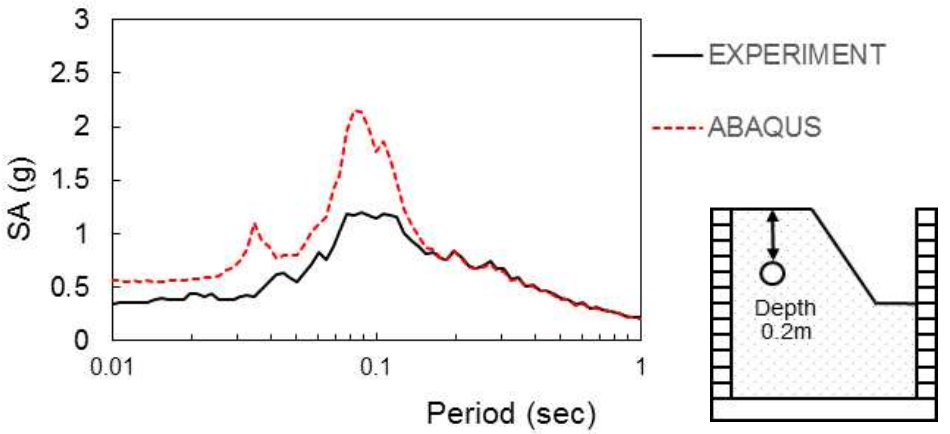

(c) Spectral acceleration by Artificial wave at depth 0.2m

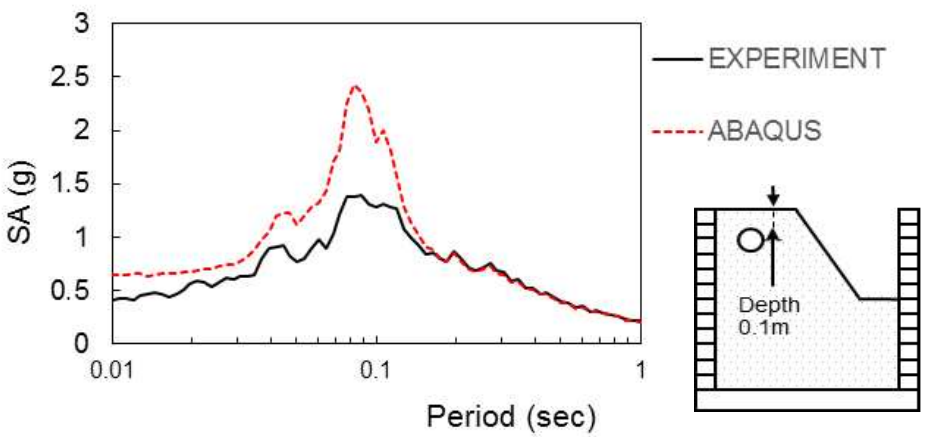

(d) Spectral acceleration by Artificial wave at depth 0.1m

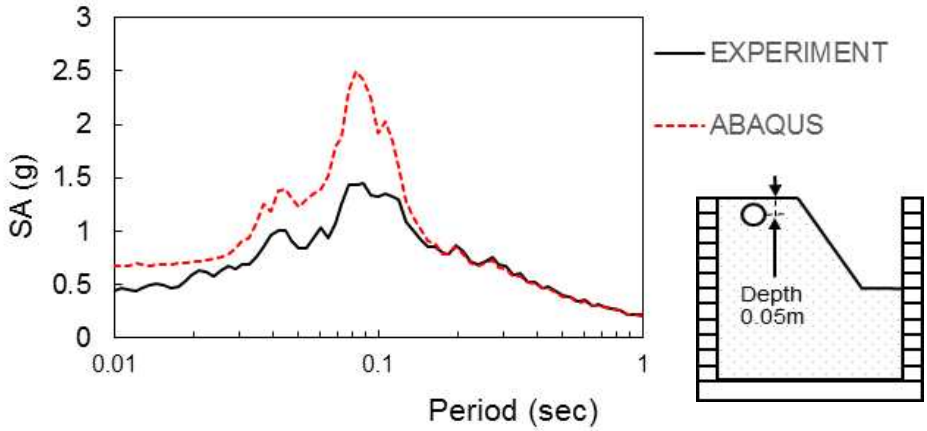

(e) Spectral acceleration by Artificial wave at depth 0.05m

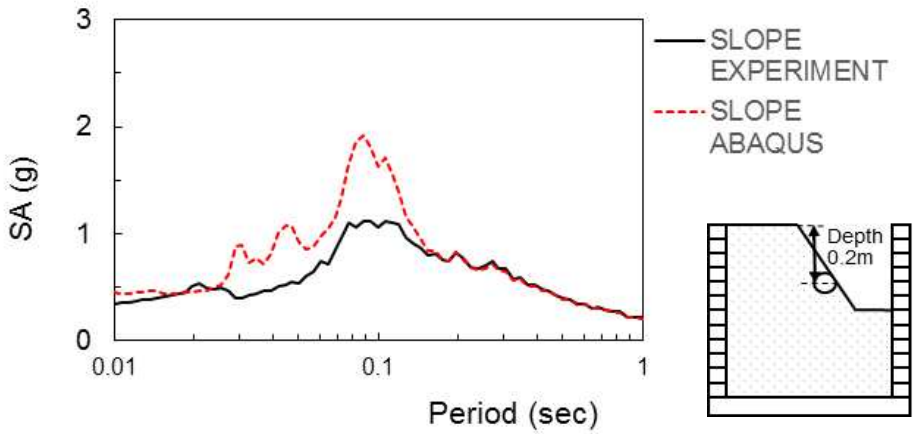

(f) Spectral acceleration by Artificial wave at depth 0.2m in slope

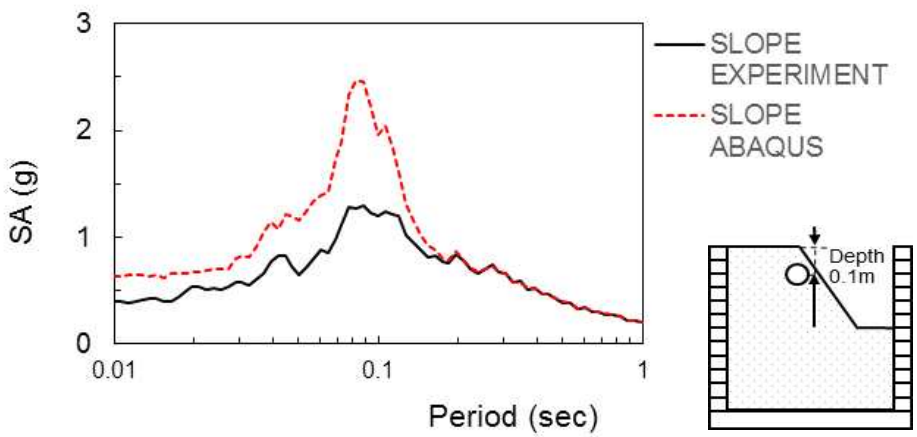

(g) Spectral acceleration by Artificial wave at depth 0.1m in slope

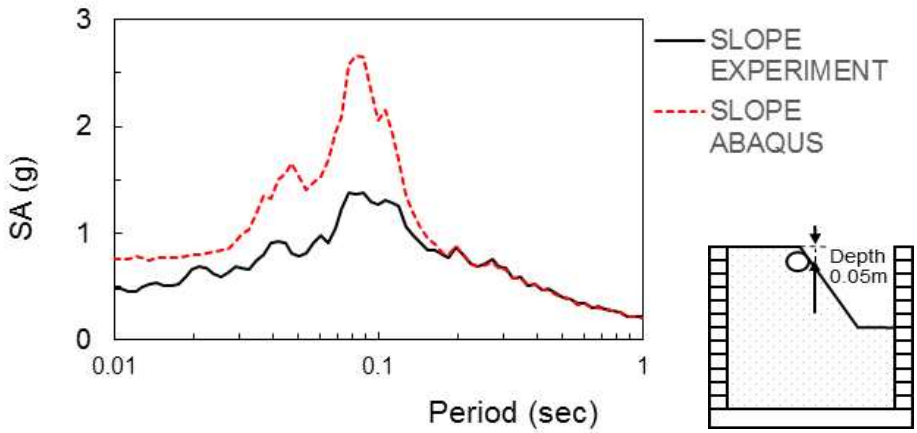

(h) Spectral acceleration by Artificial wave at depth 0.05m in slope

Figure 5.11 Spectral acceleration for experiment and analysis by Artificial wave.

Figure 5.11 (a) to (e) are the spectral acceleration of slope model under artificial seismic wave. As the depth increases, the spectrum acceleration of the test and ABAQUS gradually increases, and the difference of the spectrum acceleration gradually increases. Figure 5.11(f) to (h) are the spectral acceleration of slope model under artificial seismic wave. As the depth decreases, the test and ABAQUS spectral acceleration gradually increase. And the difference between the experimental value and ABAQUS gradually becomes larger, and the difference is the largest when it reaches the top.

For slope models with input waves of sine 8Hz and sine 10Hz, the acceleration -time history and spectral acceleration are very close to the experiment results. As shown in Figure 5.11, the slope model with the artificial wave had much larger difference in spectral accelerations between experimental and ABAQUS results at the top than that with the flat model. This difference may be due to different boundary conditions and geometry. Within the allowable range of the elastic modulus, it is possible to find adjustments to the elastic modulus to make the analysis more accurate. In this case, the acceleration magnification difference in the center of the model is not significant, but the magnification difference is obvious on the slope.

Chapter 6. Summary and Conclusions

In this study, the dynamic ground behavior performed through the 1g shaking table test was numerically analyzed using DEEPSOIL and ABAQUS. The conclusions of this study are summarized as follows:

1. In the ground acceleration profile, the experiment and analysis of DEEPSOIL and ABAQUS showed a consistent tendency to increase as the depth became shallower overall. In particular, the analysis of ABAQUS almost coincided with the ground acceleration of the experiment regardless of the input motion, it predicted the Peak ground acceleration of the experiment better than analysis of DEEPSOIL.

2. Input motion coinciding with the natural frequency of the ground or containing various frequency components, the spectral curves of the experiment and analysis of DEEPSOIL were almost identical and the maximum amplification was also the same. This indicates that using laminar shear box is a good tool to understand the dynamic behavior of soil.

3. As a result of analyzing and evaluating the dynamic load applied to the ground using 1g shaking table, using ABAQUS was more advantageous than DEEPSOIL when trying to predict the Peak ground acceleration. In order to check the amplification effect in the overall frequency period, using Spectral acceleration through 1D analysis using DEEPSOIL is considered to be more advantageous than ABAQUS Therefore, in order to verify the behavior characteristic of ground and dynamic experiment like shaking table test, it would be reasonable to use both analysis programs and to compare comprehensively.

4. The slope model with the artificial wave had much larger difference in spectral accelerations between experimental and ABAQUS results at the top than that with the flat model. This difference may be due to different boundary conditions and geometry used for the flat and slope model. The Mohr-Coulomb model often has singularities such as corners or spires in flat and slope models. Using the Darendeli model can get a smoother curve in flat models. Based on the analyses, both constitutive models have been verified to be accurate.

5. In this study, 1g shaking table experiments were performed to simulate flat grounds and slope grounds. The method of experiment and simulation ensures that the data obtained is fairly accurate. However, there is still work that needs to be done for the slope model, which will continue to be studied later.

References

1. Kwon, S. Y., and Yoo, M. (2020), “Study on the Dynamic Soil-Pile-Structure Interactive Behavior in Liquefiable Sand by 3D Numerical Simulation”, Applied Sciences, 10(8), 2723.

2. Shalev, E., Lyakhovsky, V., Ougier-Simonin, A., Hamiel, Y. and Zhu, W. (2014), “Inelastic compaction, dilation and hysteresis of sandstones under hydrostatic conditions. Geophysical Journal International”, 197(2), pp. 920-925.

3. Hardin, B. O. and Drnevich, V. P. (1972a), “Shear modulus and damping in soils: measurement and parameter effects”, Journal of Soil Mechanics and Foundations Engineering Division, ASCE, 98 (6), pp. 603-624.

4. Hardin, B. O. and Drnevich, V. P. (1972b), “Shear modulus and damping in soils: design equations and curves”, Journal of Soil Mechanics and Foundation Engineering Division, ASCE, 98 (7), pp. 667-692.

5. Martin, P. P. and Seed, H. B. (1982), “One-dimensional dynamic ground response analyses”, Journal of the geotechnical engineering division, 108(7), pp. 935-952.

6. Anderson D.(1974), “Dynamic Modulus of Cohesive Soils”, Ph.D.Thesis, University of Michigan, USA.

7. Darendeli, M. B. (2001), “Development of a new family of normalized modulus reduction and material damping curves”, Ph.D.Thesis. University of Texas, Austin, USA.

8. Idriss, I. M., Lysmer, J., Hwang, R. and Seed, H. B. (1973), “A computer program for evaluating the seismic response of soil structures by variable damping finite element procedures”, EERC Report 73-16, University of California, Berkeley, U.S.A.

9. Menq, F. Y. (2003), “Dynamic properties of sandy and gravelly soils”, Ph.D. Thesis. University of Texas, Austin, USA.

10. Seed, H. B. and Idriss, I. M. (1970), “Soil moduli and damping factors for dynamic analysis”, Report No. EERC 70-10. University of California, Berkley, USA.

11, Seed, H. B., Wong, R. T., Idriss, I. M. and Tokimatsu, K. (1986), “Moduli and damping factors for dynamic analyses of cohesionless soils”, Journal of Geotechnical Engineering, ASCE, 112(11), pp. 1016-1032.

12. Zhang, J., Andrus, R. D. and Juang, C. H. (2005), “Normalized shear modulus and material damping ratio relationships”, Journal of Geotechnical and Geoenvironmental Engineering, ASCE, 131(4), pp. 453-464.

13. Lee, C. J., Wei, Y. C. and Kuo, Y. C. (2012), “Boundary effects of a laminar container in centrifuge shaking table tests”, Soil Dynamics and Earthquake Engineering, 34(1), pp. 37-51.

14. Andersen, S. and Andersen, L. (2010), “Modeling of landslides with the material-point method”, Computational Geosciences, 14(1), pp. 137-147.

15. Faris, F. and Fawu, W. (2014), “Investigation of the initiation mechanism of an earthquake-induced landslide during rainfall: a case study of the Tandikat landslide, West Sumatra, Indonesia”, Geoenvironmental Disasters, 1(1), pp. 1-18.

16. Sun, Z., Kong, L., Guo, A. and Alam, M. (2020), “Centrifuge model test and numerical interpretation of seismic responses of a partially submerged deposit slope”, Journal of Rock Mechanics and Geotechnical Engineering, 12(2), pp. 381-394.

17. Na, S. J., Kim, D. H. and Kim, G, E. (2017), “The Behavior on Stress and Settlement of GCP Composite Ground with Different Shear Strength of Soil”, Jonal of the Korean Geosynthetics Society, 16(3), pp. 63-74.

18. Park, D. and Hashash, Y. M. (2004), “Soil damping formulation in nonlinear time domain site response analysis”, Journal of Earthquake Engineering, 8(02), pp. 249-274.

19. Jung, G. D., Youn, S. K. and Kim, B. K. (2000), “A three-dimensional nonlinear viscoelastic constitutive model of solid propellant”, International Journal of Solids and Structures, 37(34), pp. 4715-4732.

20. Abaqus Inc, 2014. Abaqus/CAE User’s Manual Version 6.14. Abaqus, Inc..,Pawtucket, Providence, RI.

21. Hashash, Y. M. and Park, D. (2001), “Non-linear one-dimensional seismic ground motion propagation in the Mississippi embayment”, Engineering Geology, 62(1-3), pp. 185-206.

22. Ramberg, W. and Osgood, W. R. (1943), “Description of stress-strain curves by three parameters”, National Advisory Committee for Aeronautics, Washington, DC, USA,

23. Kim, H., Kim, D., Lee, Y.and Kim, H. (2020), “Effect of Soil Box Boundary Conditions on Dynamic Behavior of Model Soil in 1 g Shaking Table Test”, Applied Sciences, 10(13), 4642.

24. Zhang, J., Andrus, R. D. and Juang, C. H. (2005), “Normalized shear modulus and material damping ratio relationships,” Journal of Geotechnical and Geoenvironmental Engineering, 131(4), pp. 453-464.

25. Roblee, C. and Chiou, B. (2004), “A proposed Geoindex model for design selection of non-linear properties for site response analysis”, In International workshop on uncertainties in nonlinear soil properties and their impact on modeling dynamic soil response. PEER Headquarters, pp. 18-19.

26. Huo, H. (2005), “Seismic design and analysis of rectangular underground structures”, Ph.D Thesis. Purdue University, Indiana, USA.

27. Douglas, J. (2003), “Earthquake ground motion estimation using strong-motion records: a review of equations for the estimation of peak ground acceleration and response spectral ordinates”, Earth-Science Reviews, 61(1-2), pp. 43-104.

28. Vucetic, M. and Dobry, R. (1991), “Effect of soil plasticity on cyclic response”, Journal of Geotechnical Engineering, 117(1), pp. 89-107.

29. Zhang, J. (2004), “Characterizing the dynamic properties of South Carolina soils for ground motion evaluation,” Ph.D Thesis. Clemson University, Clemson, USA.

30. Anderson, D. G. (2003), “Laboratory Testing of Nonlinear Soil Properties: I & II. prepared by CH2M HILL, Bellevue, Washington for the Lifeline Research Program”, Pacific Earthquake Engineering Research Center. University of California, Berkley, USA.

31. Phillips, C. and Hashash, Y. M. (2009), “Damping formulation for nonlinear 1D site response analyses”, Soil Dynamics and Earthquake Engineering, 29(7), pp. 1143-1158.

32. Choi, C., Song, M., Kim, D. and Yu, X. (2016). “A New Non-Destructive TDR System Combined with a Piezoelectric Stack for Measuring Properties of

Geomaterials," Materials, 9(6), 439.

33. Helwany, S. (2007), "Applied soil mechanics with ABAQUS applications," John Wiley & Sons.

34. Kim, H. Y., Jin, Y., Lee, Y. H., Kim, H. S. and Kim, D. H. (2020), "Dynamic response characteristics of embankment model for various slope angles", Journal of the Korean Geosynthetics Society, 19(2), pp. 35-46.

35. Yun, S. U. and Park, D. H. (2009), "Estimation of amplificationof slope via 1-D site response analysis", Journal of the Korean Geotechnical Society, pp. 620-625.

36. Kim, J. M., Ryu, J. H., Son, S. W., Na, H. Y.and Son, J. W. (2011), "A comparative study on dynamic behavior of soil containers that have different side boundary conditions," Journal of the Korean Geotechnical Society, 27(12), pp. 107-116.

37. Masing, G. (1926), "Eigenspannungen und Verfestigung beim Messing", Second International Congress of Applied Mechanics, pp. 332 -335.

38. Stokoe, K. H., Darendeli, M. B., Andrus, R. D. and Brown, L. T. (1999), "Dynamic soil properties: laboratory, field and correlation studies", In Earthquake geotechnical engineering, pp. 811-845.

39. Ishibashi, I. and Zhang, X. (1993), "Unified dynamic shear moduli and damping ratios of sand and clay," Soils and Foundations, 33(1), pp. 182-191.

40. Sun, J. I., Golesorkhi, R. and Seed, H. B. (1988), "Dynamic moduli and damping ratios for cohesive soils", Earthquake Engineering Research Center, University of California, Berkeley, USA.

41. U.S. Army Corps of Engineers (USACE). (1978), "Dynamic test report sheets on soil samples for Richard B. Russell Dam." Rep. No. EN-FS- 77-84, South Atlantic Division Laboratory, Marietta, USA.

42. Hashash, Y.M.A., Musgrove, M.I., Harmon, J.A., Groholski, D.R., Phillips, C.A., and Park, D.(2016), "DEEPSOIL 6.1, User Manual." University of Illinois, U.C.

43. Helwany, S. (2007), Applied Soil Mechanics with ABAQUS Applications. Wiley, New York.

44. Kezdi, A. (1974), Handbook of Soil Mechanics. Elsevier, Amsterdam.

45. Prat, M., Bisch, E., Millard, A., Mestat,P.,and Cabot, G. (1995), "La modelisation

des ouvrages." Hermes, Paris.

46. Faris, Fikri, and Fawu Wang. (2014), "Investigation of Tandikat Landslide, West Sumatra, Indonesia." Landslide Science for a Safer Geoenvironment, pp. 161-167.

47. Liu Jingbo, Gu Yin and Du Yixin. (2006), "Consistent viscous-spring artificial boundaries and viscous-spring boundary elements." Chinese Journal of Geotechnical Engineering, 28(9), pp 1070-1075.